Optical spectroscopy of reconstructed and moiré van-der-Waals bilayers

DISSERTATION ZUR ERLANGUNG DES DOKTORGRADES
DER NATURWISSENSCHAFTEN (DR. RER. NAT.)
DER FAKULTÄT FÜR PHYSIK
DER UNIVERSITÄT REGENSBURG

vorgelegt von

Philipp Parzefall

aus Niederwinkling

im Jahr 2025

Das Promotionsgesuch wurde eingereicht am: 05.11.2025

Die Arbeit wurde angeleitet von: Prof. Dr. Christian Schüller

Prüfungsausschuss:	Vorsitzender:	Prof. Dr. Gunnar Bali
	1. Gutachter:	Prof. Dr. Christian Schüller
	2. Gutachter:	PD Dr. Jonathan Eroms
	Weiterer Prüfer:	Prof. Dr. Dominique Bougeard

Contents

Chapter 1

From silicon to van-der-Waals bilayers: Towards tunable optoelectronics

---

Every human carries the profound need to live in a safe and secure environment. Additionally, a fundamental wish of each individual is to ease life's hardships, which has been accomplished throughout history by creativity and invention. The resulting development of tools and instruments has, in turn, shaped entire eras and their societies. However, each technological advancement carries inherent limitations, which spark the next wave of innovation.

The shaping tools in the current (post-)Information Age are digital devices. They enable rapid information exchange and are therefore the driving force behind economics and knowledge interchange. The building blocks of modern devices, silicon-based microprocessors, have been continuously miniaturized and are now approaching their quantum-mechanical limits. Here, leakage currents result in significant power losses, making heat dissipation a critical technological limitation [1–4].

It is up to the research community to overcome these fundamental limitations and provide concepts for the next generation of devices. Current strategies involve the design of specialized architectures. Two promising approaches are neuromorphic systems, which mimic neural networks [5–7], and parallel or near-data processing, which addresses the von Neumann bottleneck [8–10]. In completely novel approaches, quantum computers mimic problems that are inaccessible to classical circuits [11–13], or new carriers of information are investigated. At the forefront of this research, photons

promise reduced energy losses and faster communication speed [14–21], while electron spin enables non-volatile information storage and lower processing energy costs [22–24].

Alongside these conceptual advances, entirely new material systems are explored—one of which will be the focus of this thesis, and is a member of the family of van der Waals (vdW) semiconductors. These consist of two-dimensional (2D) atomically thin layers, which are bound by weak vdW forces into naturally occurring bulk crystals. When extracting a single layer, which can be achieved with sticky tape [25, 26], novel physical properties can emerge. The most prominent and first-discovered single-layer—monolayer (ML)—material is graphene, which alone exhibits numerous remarkable phenomena due to its massless Dirac fermions [27–38]. Since its discovery, a whole family of 2D materials spanning semiconductors, insulators, superconductors, and even 2D magnets has been discovered. Throughout this thesis, the materials of the 2D vdW class transition metal dichalcogenide (TMDC) will be central to all investigations. They are of particular interest, as they are direct semiconductors in the ML limit with large light-matter interactions and exciton physics dominate even at room temperature [39–45]. Additionally, spin-valley selective excitations [46–48] make them a prime candidate not only for optoelectronics but also for spintronics.

Going beyond the ML limit, an artificial stacking of bilayers (BLs) or heterostructures introduces tunability into the designed system. Here, the electronic band alignment is of particular interest. The material combination of TMDC MLs can be chosen so that hetero-BLs emerge with excitons situated across both layers, resulting in a permanent out-of-plane dipole [49–52] and, therefore, long lifetimes, which is of interest for excitonic devices.

Another prominent tuning knob in artificial BLs is introduced when layers are twisted relative to each other or when materials with a lattice mismatch are used, or both. The result is an emergent superlattice, which influences charge carriers, excitons, and phonons, revealing novel physical phenomena. These include the formation of localized excitons [53–61] and electron lattices [59, 62–72], resulting in the rise of integer- and fractional anomalous quantum Hall effect [73–77], kinetic magnetism [59], and unconventional superconductivity in twisted BL graphene [78–81]. These emerging physics, in turn, shape the optical response of the designed vdW structure, which offers a powerful, fast, and non-invasive probe that will primarily be used in this thesis.

Under this premise, fundamental excitonic and phononic phenomena in vdW BL systems are explored, with a special focus on heterostructures. The investigated struc-

tures are designed with specific materials—defining the band alignment and lattice constants—and controlled twist angles to tailor and control their properties. The two main findings in this work, phonon-assisted resonant energy transfer and quasiparticle–phonon coupling, emerge in two separate regimes, the moiré superlattice and a lattice under atomic reconstruction, respectively.

In the first regime, moiré superlattices confine excitons and influence vibrational modes. Resonant photoluminescence (PL) spectroscopy on encapsulated $MoSe_2$–WS_2 BLs reveals phonon-assisted resonant energy transfer between localized excitons, which can be controlled by electrostatic doping. Complementarily, superlattice physics gives rise to moiré phonons, detected in Raman spectroscopy, which can serve as a fast, non-invasive probe of the local twist angle.

In the second case of atomic reconstruction, the focus shifts to reconstructed BL lattices, their excitonic landscape, and the resulting interactions with free charge carriers. In $MoSe_2$–WSe_2 heteros-BLs, an emergent trion–phonon coupling, uncovered in resonant Raman spectroscopy, can be explained by the coupling of an interlayer phonon to hybridized trions. In electrostatically doped devices, this coupling can be tuned, enabling programmability. The experimental coupling signature is then used as a tool to investigate the electronic and excitonic landscape in real and reciprocal space of homo-BL and WSe_2 few-layer structures.

Together, these studies advance the microscopic understanding of exciton–phonon interactions in TMDC BLs across distinct lattice regimes, and point towards strategies for tailoring such couplings in future optoelectronic devices.

Before presenting the experimental results in Chapter 4, the thesis develops the necessary theoretical and methodological background. Chapter 2 introduces the material systems under investigation, emphasizes exciton complexes and the optical and vibrational properties of TMDCs, and outlines the spectroscopy techniques—PL, reflection, and Raman spectroscopy—used to probe exciton–phonon interactions. Chapter 3 describes the optical setups for resonant and nonresonant measurements, as well as the fabrication of high-quality heterostructures. In Chapter 5, a summary of the main findings, a discussion of their implications, and a brief perspective for future avenues of research are given, laying the foundation for 2D material-based applications.

Chapter 2

Fundamentals of optical spectroscopy in 2D semiconductors

As already emphasized during the introduction, semiconductors form the basis of today's technology, as transistors are the core building blocks of electronic devices. They enable precise signal control and drive advances in microprocessors, memory, and sensors. There are various transistor architectures, such as field-effect and bipolar junction transistors, which have driven the evolution of electronics and are therefore the foundation of modern technology [82, 83].

Ongoing research in various materials and in device fabrication has pushed silicon technologies to their quantum limits. 2D vdW semiconductors have emerged as candidates for next-generation electronics, in part due to their unique excitonic properties. The dielectric screening in these materials is reduced due to their 2D character, resulting in large exciton binding energies that enable exciton formation even at room temperature. Additionally, their strong light-matter interactions make them a prime candidate for future optoelectronic applications.

2.1 Transition metal dichalcogenides

TMDCs are a prominent class of vdW semiconductors that have been studied for over a century in bulk form, resulting in well-explored and characterized crystal structure and

bulk properties [84–86]. Molybdenite, a naturally occurring TMDC, was first examined optically by X-ray diffraction spectroscopy in 1923 [87].

As highlighted earlier, a breakthrough came when Novoselov, Geim, and colleagues demonstrated mechanical exfoliation of atomically thin, air-stable MLs from bulk graphite and TMDC crystals [25, 88]. This discovery sparked intense research into the 2D family and their possible heterostructures in the last decades, which will also be explored extensively in this thesis. Before exploring these systems in detail, the fundamental crystal, electronic, and optical properties of ML TMDCs, along with the theoretical foundations of the optical measurement techniques, are introduced.

2.1.1 Crystal structure

The primitive unit cell of TMDCs contains a transition-metal atom "M" and two chalcogen atoms "X", corresponding to the stoichiometry MX_2. A single covalently bonded ML consists of three atomic layers, where the transition-metal atoms are sandwiched in between the chalcogens, forming a trigonal prismatic unit cell (see Fig. 2.1.1**a**). The resulting ML lacks spatial inversion symmetry.

Bulk TMDC crystals are composed of multiple MLs stacked vertically and held together by weak vdW forces. Due to their rotational symmetry of 180°, two prominent stacking configurations emerge, one without relative twist between the adjacent layers, the R-type, and one with a rotation of $\theta = 60°$, the H-type stacking. In naturally occurring crystals, a repeating two-layer sequence of H-type stacking can be predominantly found, which is depicted in Fig. 2.1.1**b**. In contrast, the R-type configuration corresponds to a repeating three-layer sequence, as shown in Fig. 2.1.1**c**. A more detailed discussion of

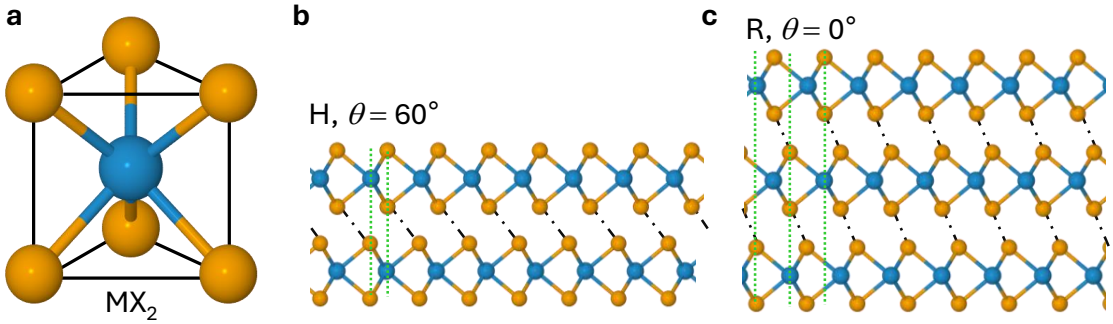

Figure 2.1.1 | **a** Trigonal prismatic unit cell of a TMDC ML. The transition-metal atom "M" is shown in blue, and the chalcogen atoms "X" are shown in orange. Side views of **b** H-type and **c** R-type stacked TMDC layers.

stacking configurations and the nomenclature used to describe artificially stacked BLs is provided in Section 4.2.

The crystal structure is hexagonal, as shown in the orthographic top view in Fig. 2.1.2**a**. In momentum space, this corresponds to a hexagonal first Brillouin zone (BZ) [86], which is illustrated in Fig. 2.1.2**b**. There, the relevant high-symmetry points are shown: the Γ point at the center, the K points at the edges, the M points between them, and the Q points along the Γ–K axis. In odd-layer systems, the absence of inversion symmetry renders the K and Q valleys inequivalent, giving rise to the corresponding K′ and Q′ points connected by time-reversal symmetry. The implications of this inequivalence will be discussed following the introduction of the general electronic structure.

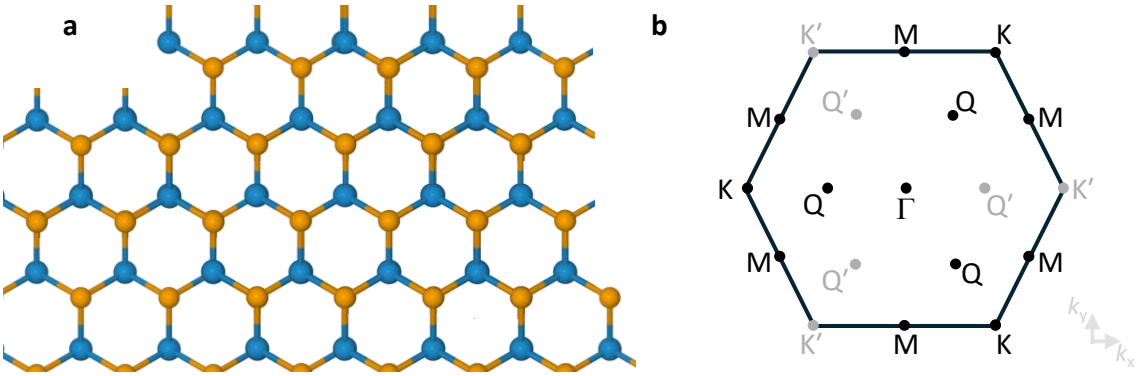

Figure 2.1.2 | a Orthographic top view and **b** hexagonal first BZ of a TMDC ML.

2.1.2 Electronic structure

TMDC semiconductors in the bulk limit are indirect bandgap materials [84, 86, 89, 90], with a transition to a more direct bandgap as the layer number decreases [91, 92]. The transition to a direct bandgap semiconductor in momentum space in the ML limit was first experimentally observed by Splendiani *et al.* [39] and Mak *et al.* [40]. This indirect-to-direct bandgap evolution is illustrated in representative band structure calculations for bulk, BL, and ML MoS_2 shown in Fig. 2.1.3**a**. As the number of layers decreases, the valence band (VB) maximum shifts from the Γ to the K point, while the conduction band (CB) minimum moves from the Q to the K valley [39, 93, 94].

The aforementioned spatial inversion symmetry breaking in structures with an odd number of layers, combined with strong spin-orbit coupling arising from the heavy metal atoms, results in a spin splitting at the VB maxima and at the CB minima [95–99]. The VBs are, hereby, separated by several hundred meV, while the splitting of the

CBs is minor and even changes sign depending on the metal. The splitting magnitudes of relevant TMDCs, calculated by Ref. [99], are given in Tab. 2.1 and were directly experimentally observed using angle-resolved photoemission spectroscopy (ARPES). Here, the momentum and energy of photoemitted electrons from the material's VB are resolved. Such a spectrum along the Γ-K direction for a ML $MoSe_2$ is shown in Fig. 2.1.3**b**, where the binding energy is given with respect to the Fermi energy E_F [100]. The second energy derivative is shown in order to highlight the band splitting.

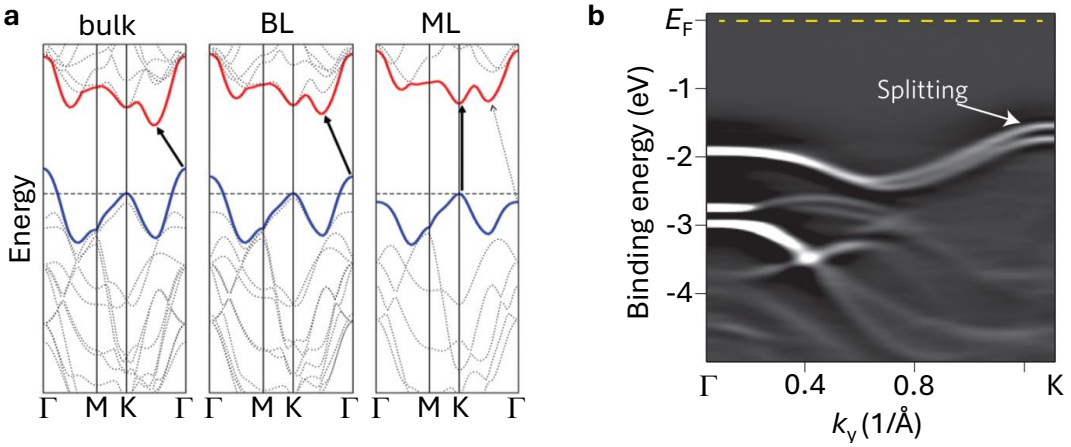

Figure 2.1.3 | a Calculated band structure of bulk, BL and ML MoS_2, shown from left to right. The lowest CB and the highest VB are highlighted in red and blue, respectively. The energetically lowest transitions are marked by solid arrows (adapted from Ref. [39]). **b** Second derivative of the ARPES spectrum of ML $MoSe_2$ measured along the Γ-K direction (adapted from Ref. [100]).

Since the K and K′ valleys are related by time-reversal symmetry, the spin splitting acquires opposite signs in the two valleys. This opposing spin orientation directly ties the spin degree of freedom to the valley, providing the basis for spin–valley locking, which enables selective excitation of the K and K′ valleys using circularly polarized light with σ^+ and σ^- helicities, respectively [46–48, 96, 101–103] (see Fig. 2.1.4).

	Δ_{VB} [meV]	Δ_{CB} [meV]
$MoSe_2$	186	-22
MoS_2	148	-3
WSe_2	466	32
WS_2	429	37

Table 2.1 | Calculated CB and VB spin splitting at the K points (from Ref. [99]).

Furthermore, spin-valley locking persists in each ML of an H-type TMDC multilayer. Here, the K and K′ points alternate between adjacent layers, resulting in spin-layer locking [96, 104–108]. Generally, the energetically lowest transition from the VB to the

CB at the K points is spin-allowed in MoX_2 but spin-forbidden in WX_2 [99, 109–111]. Notably, the spin orientation of the bands at the WX_2 Q valley is opposite to that at the K point [99, 111].

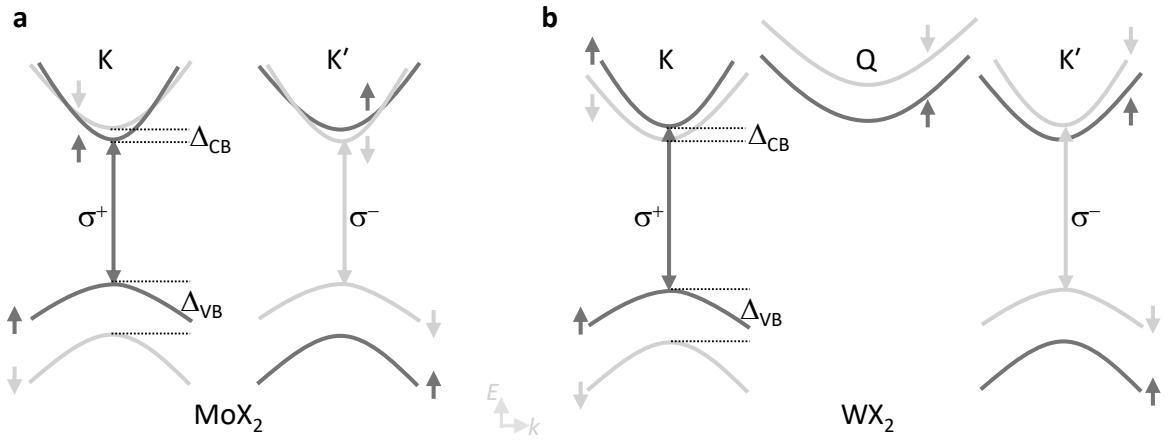

Figure 2.1.4 | Schematic electronic band structure of **a** MoX_2 and **b** WX_2 ML, including spin-orbit coupling and the consequent spin splitting $\Delta_{CB/VB}$. The different spin orientations are indicated by arrows and color shading. Due to spin-valley locking, the K and K′ valleys can be selectively addressed by σ^+ and σ^- circularly polarized light, respectively. In WX_2, the spin orientation at the Q valley is opposite to that at the K point (adapted from Refs. [99, 111]).

2.2 Excitons in 2D materials

The previously mentioned exciton is a Coulomb-bound electron-hole pair. It may form when an electron is excited from the VB to the CB. The resulting void can be considered a positively charged hole with opposite spin and momentum. Their binding, of the hole and the electron, results in a quasi-particle, conceptually analogous to a hydrogen atom. Additionally, their binding reduces the single-particle bandgap.

Excitons are classified into the following two categories. The Frenkel excitons, which are highly localized with binding energies on the order of several electron volts, and Wannier-Mott excitons, which exhibit lower binding energies and are characterized by a delocalized wavefunction.

Comparing these classifications to ML TMDCs results in a mixed picture. The excitons exhibit large, Frenkel-like, binding energies of $\approx 500\,\mathrm{meV}$, resulting in tightly bound excitons [41–45, 112]. Despite this, their Bohr radius is about $1,\mathrm{nm}$ [43, 113, 114], and

the observation of well-resolved Rydberg series—analogous to those in the hydrogen atom—further supports a description within the Wannier–Mott framework [44, 115].

The exciton corresponding to a transition from the VB maximum to the CB minimum is referred to as the A exciton (X^0) (see Figs. 2.1.4**a, b**). The exciton associated with the transition from the energetically lower spin-split VB to the corresponding spin-split CB is termed the B exciton.

For an estimation of the exciton energy E_X, the 2D hydrogen model with a reduced excitonic mass has to be used in order to calculate the binding energy more accurately. This leads to the equation, following Refs. [44, 116, 117]

$$E_X = E_{gap} - E_{bind} + E_{kin} = E_{gap} - \frac{1}{2}\frac{\mu e^4}{(4\pi\epsilon_0\epsilon_{ext})^2\,\hbar\left(n-\frac{1}{2}\right)^2} + \frac{\hbar^2 K_X^2}{2M_X}, \tag{2.2.1}$$

where E_{gap} represents the free-particle bandgap, E_{kin} is the exciton's center-of-mass kinetic energy and E_{bind} is the exciton binding energy. Here, μ is the exciton's reduced mass, M_X is the exciton's total mass, K_X is the exciton's center-of-mass momentum, and ϵ_{ext} is the external relative permittivity. The quantum number n is analogous to that of the hydrogen atom. With increasing n, E_{bind} decreases quadratically and the Bohr radius increases linearly.

For MLs, an additional prominent factor influencing the excitonic binding energy is the change in dielectric environment. Especially, the tightly bound excitons $n = 1, 2$ are influenced by the contrast of strong screening within the layer and weak screening in the surrounding medium [44], which is schematically compared to bulk excitons in Figs. 2.2.1**a, b** with relative permittivities ϵ_{2D} and ϵ_{3D}. The inherently weak dielectric screening outside the TMDC ML results in high excitonic binding energies, giving rise to pronounced excitonic effects that persist even at room temperature [44, 118].

Inhomogeneities in samples must be considered, as the spatial extent of the X^0 wavefunction makes it highly sensitive to its surroundings. This is conceptually illustrated in Fig. 2.2.1**b**, where a substrate alongside contaminations are shown. Those variations are on the scale of the laser spot size and result in a significant inhomogeneous broadening of the excitonic resonances. Using insulating hexagonal boron nitride (hBN) in order to encapsulate the ML, a drastic reduction of such a broadening is achieved, as it is atomically flat [119–123]. Furthermore, the encapsulation provides additional protection against degradation, effectively preserving the ML [124].

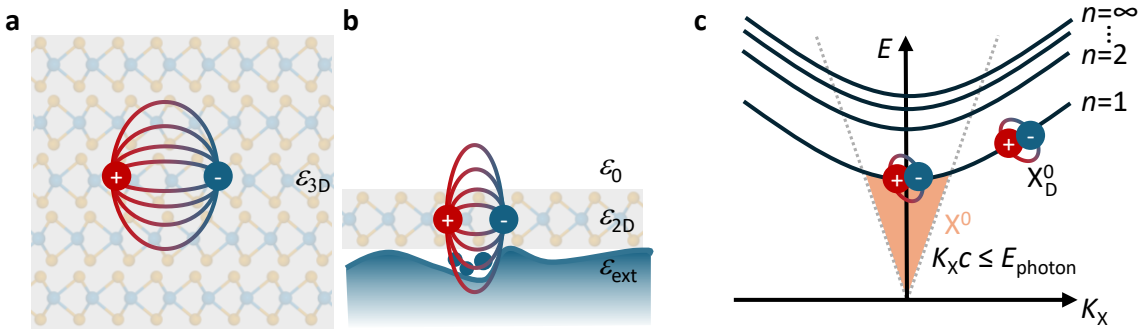

Figure 2.2.1 | Real-space representation of excitons for **a** bulk and **b** ML TMDC. The dielectric environment is indicated by gray-shading and the different relative permittivities ϵ_{3D}, ϵ_{2D}, ϵ_0 and a fluctuating external dielectric environment ϵ_{ext} (adapted from Ref. [44, 119]). **c** Schematic illustration of the exciton dispersion with the exciton center-of-mass momentum K_X in the two-particle representation. Higher excited states are labeled until the continuum is reached. The momentum conservation restricts transitions to $K_X c \leq E_{photon}$ and is indicated by the orange light cone. Excitons outside the light cone are called momentum dark X^0_D.

The exciton dispersion within the two-particle picture is schematically illustrated in Fig. 2.2.1**c**. The lowest-energy exciton (the A exciton) with its energy E_{X^0}, defines the optical band gap [111]. It is from now on denoted as X^0. For radiative recombination of the exciton to occur, momentum conservation must be satisfied. This requirement constrains optically active excitons to those whose center-of-mass momentum K_X matches the in-plane momentum of the emitted photon, forming what is known as the exciton light cone.

Excitons with momenta outside this light cone are termed momentum-dark excitons (X^0_D), as they can only couple to light in a second-order process involving an additional phonon. Furthermore, excitons can also be spin-dark if the electron and hole comprising the exciton possess parallel spins, thereby making the radiative recombination spin-forbidden.

Further considerations on the exciton can be made by looking at the VB and CB curvatures of calculated band structures, as they reflect the effective mass of the exciton. For instance, the WSe_2 K-Q exciton—formed by an electron in the Q valley and a hole in the K valley—exhibits a higher binding energy due to the larger effective mass, which results in a lower total exciton energy E_X compared to the K–K exciton, despite the single-particle band structure suggesting the opposite (see Fig. 2.1.4**b**). As a result, the lowest-energy exciton in ML WSe_2 is momentum-dark. Nonetheless, such

dark states can be probed optically through phonon-assisted scattering processes, spin-mixing mechanisms, or back focal plane imaging [125–130].

Charged excitons, termed trions, result when the exciton further binds to additional charge carriers. The increased binding energy is approximately 30 meV [131–133]. In general, a more comprehensive description is required, as the exciton interacts with a whole Fermi sea at large charge densities [133–135]. In this regime, many-body interactions must be considered. Applying perturbation theory to the Fermi sea fluctuations reveals that the system is more appropriately described in terms of attractive and repulsive Fermi polarons, as illustrated in Fig. 2.2.2**a**, analogous to the interaction of an electron with phonons in a crystal [136, 137].

In this picture, the exciton is dressed by an electron screening cloud, which modifies its binding energy. This framework enables a consistent interpretation of the Rydberg-like $(1s, 2s, 3s, ...)$ excitonic series even at high carrier densities [133, 138, 139]. Optical signatures of such a series at various charge doping levels are shown in Fig. 2.2.2**b**, where the absorbance is presented and the doping level is modified by an applied external gate voltage U_G. The second energy derivative of the reflection contrast (RC) is used to enhance the contrast. An introduction to this technique will be provided in the following section. Additionally, the formation of biexcitons [123] or even higher-order excitonic complexes [140–142] is possible, where two or more excitons bind to each other.

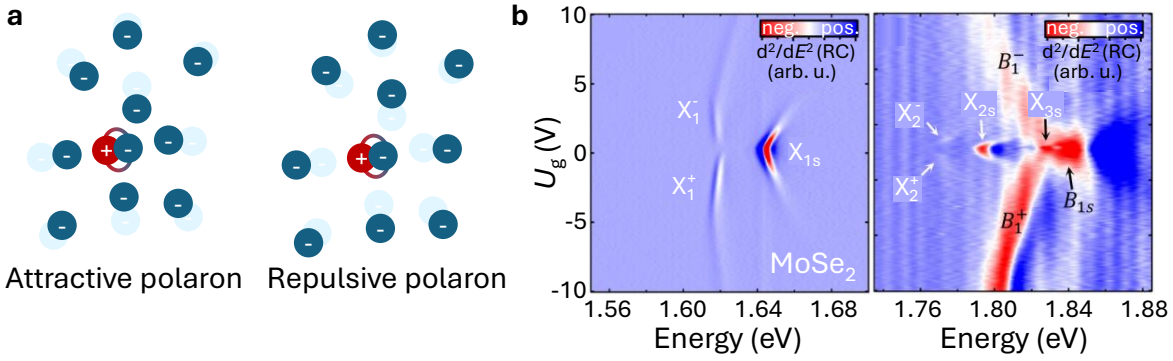

Figure 2.2.2 | a Schematic picture of an attractive- and a repulsive polaron. The bound exciton attracts or repulses the surrounding Fermi sea, respectively. **b** Gate-dependent maps of the second derivative of the ML $MoSe_2$ RC at $T = 15\,K$. The Rydberg-series of X^0 and the B exciton in charge neutrality and at varying doping levels are marked (adapted from Ref. [133]).

In order to correctly interpret measurements on excitonic resonances, it is essential first to introduce the underlying spectroscopic techniques. This will provide deeper insights into the spectral response of TMDCs.

2.3 Optical spectroscopy in transition metal dichalcogenides

This thesis needs to link experimental signatures to microscopic phenomena. Here, the fundamental consideration is the Lorentz oscillator model, which simplifies the solid's interaction with electromagnetic radiation. This simplification describes the electron clouds bound to the nuclei as springs. Their resulting motion—and thus their interaction—can be described as a driven, damped oscillator. From this classical picture, the refractive index and absorption coefficients can be calculated, which, in turn, determine the reflectivity using the Fresnel formulas. An ensemble of Lorentzian oscillators with discrete eigenenergies, coupling strengths, and damping constants can, thus, describe TMDCs in linear optics [116, 117, 143].

2.3.1 Absorption measurements

One common approach for measuring absorption is to measure the sample's RC. This method provides a measure of the absorption by illuminating a sample with a broadband white-light source. The reflected signal from the sample (R) is hereby compared to both a reference reflection spectrum (R_{ref}) and a background spectrum (R_{BG}). The R_{ref} is taken at a location, which features the exact same structure except for the investigated sample. The reflection contrast is then defined as

$$RC = \frac{R - R_{ref}}{R_{ref} - R_{BG}}. \tag{2.3.1}$$

The resulting relative intensity is directly linked to the oscillator strength and thus reflects the strength of the optical transitions. For a more detailed analysis of the spectrum, it is necessary to account for the dielectric environment and the thickness of each layer in the sample to correct for multilayer interference effects. In the simplest case of a ML, only the Si/SiO_2 substrate must be considered. However, as sample complexity increases—e.g., by adding hBN layers—the analysis becomes progressively more chal-

lenging. One practical approach to isolating changes in the material's absorption is to tune its properties externally.

An example for RC measurements on $MoSe_2$, measured by Ref. [133], is provided in Fig. 2.2.2**b**. Here, the second derivative of the ML $MoSe_2$ RC spectra is shown doping-dependent in a heatmap. In these spectra, one can clearly resolve the neutral and charged A exciton Rydberg series, as well as the B exciton.

An alternative method for probing quasi-particle resonances—and one employed in this thesis—is the measurement of the resonance fluorescence (RF) signal. In this technique, the laser energy is tuned into extreme resonance with the targeted optical transition. The resulting excitation leads to the radiative, coherent recombination of the quasi-particle and provides a measure of the oscillator strength, the density of states, and the oscillator resonance energy.

2.3.2 Photoluminescence spectropscopy of excitonic states

PL spectroscopy is the experimental method where the optical response of a system is investigated after optical excitation. It is used to probe excitonic physics, usually by coherent irradiation, as follows. The formed quasi-particles, after an electron is excited from the CB to the VB by laser energies $\geq E_X$, thermalize via phonon interactions into lower-energy states, where they can radiatively recombine. Afterwards, this optical response is analyzed spectrally. The energies thus indicate excitonic resonances, and their intensities provide further insights, e.g., into selection rules. Indirect semiconductors exhibit weak PL peaks contrary to direct ones, which is exemplarily shown for the direct ML and the indirect BL MoS_2 PL in Fig. 2.3.1**a** (adapted from Ref. [40]).

A prime candidate for discussing a PL spectrum is ML WSe_2 at cryogenic temperatures. It exhibits a rich optical response with multiple peaks, which is shown in Fig. 2.3.1**b**. An understanding of this optical response can be gained by using the earlier introduced excitonic complexes and the WX_2 band structure (c.f. Fig. 2.1.4**b**). In this representative spectrum, the A exciton signal is fitted with a Lorentzian function. The resulting narrow full-width at half maximum (FWHM) of 3.9 meV, achieved through encapsulation in hBN, is dominated by the exciton lifetime and serves as an indicator of high sample quality.

Various previously discussed complexes are now directly observed in experiment and identified following Ref. [144]. Charged excitons exist in both singlet (X_S^-) and triplet

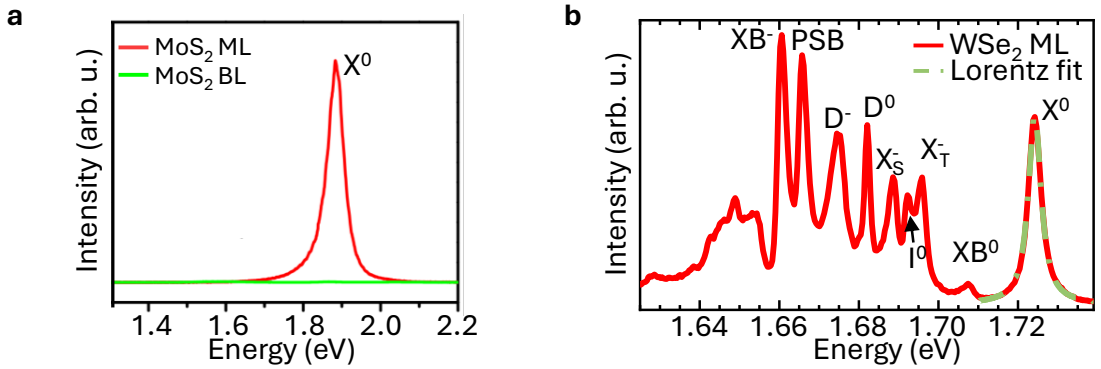

Figure 2.3.1 | **a** PL spectra of ML and BL MoS_2 samples at room temperature (adapted from Ref. [40]). **b** PL spectrum of an hBN encapsulated ML WSe_2 at cryogenic temperature. The X^0 is fitted with a Lorentzian function with a FWHM= 3.9 meV. The ML peaks are identified according to Ref. [144].

(X_T^-) configurations, depending on whether the additionally bound electron occupies the lowest CB in the same or the opposite valley, respectively. These complexes are shown for the K valley in Fig. 2.3.2**a**. The energy splitting is due to the short-range exchange interaction, which is sensitive to both spin and valley [145]. The biexciton (XB^0), shown in Fig. 2.3.2**b**, appears alongside its charged configuration (XB^-).

Furthermore, the momentum-indirect, exciton (I^0), stemming from a K-valley hole and a Q-valley electron, as well as the spin-forbidden lowest-energy K-valley exciton (D^0), can be identified in the PL spectrum in Fig. 2.3.1**b**. These states are schematically shown in Fig. 2.3.2**c**. Complementarily, the dark trion (D^-) is observed in the WSe_2 spectrum. Further momentum-dark excitons must be considered, as they can be brightened by phonon-assisted processes [128–130]. This leads to phonon sidebands (PSBs) in the PL spectrum. The low-energy PL signatures around 1.65 eV are attributed to localized excitons bound to defects. This in-depth understanding of a PL spectrum illustrates the experimental access to the excitonic landscape of TMDCs via PL spectroscopy.

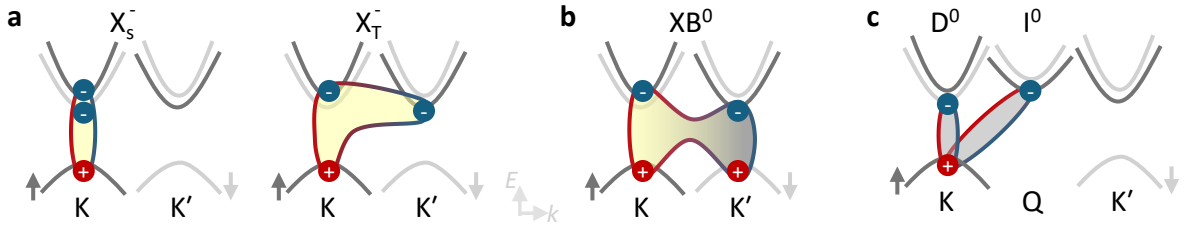

Figure 2.3.2 | Schematic representation of selected excitonic complexes in WSe_2 ML. **a** The bright trions (X_S^-, X_T^-), **b** the neutral biexciton (XB^0) and **c** the momentum-indirect (I^0) together with the spin-forbidden (D^0) exciton.

2.3.3 Raman spectroscopy

Raman spectroscopy is one of the key experimental techniques used in this thesis. The term Raman scattering, hereby, refers to the inelastic scattering of incident electromagnetic waves, in this case, with solids. During this scattering event, a phonon is either created, in so-called Stokes scattering, or annihilated, which is denoted as anti-Stokes scattering [146–151]. Both inelastic scattering events are schematically illustrated in Fig. 2.3.3**a**.

During both, the momentum and energy are conserved, which can be expressed by

$$\begin{aligned} \boldsymbol{k}_{\mathrm{S}} &= \boldsymbol{k}_{\mathrm{I}} \pm \boldsymbol{q} \\ \hbar\omega_{\mathrm{S}} &= \hbar\omega_{\mathrm{I}} \pm \Omega, \end{aligned} \tag{2.3.2}$$

where $\boldsymbol{k}_{\mathrm{S}}$, $\boldsymbol{k}_{\mathrm{I}}$, ω_{S}, ω_{I} are the scattered and incident wave vectors and frequencies. The phonon wave vector and frequency are labeled $\boldsymbol{q}$ and Ω, respectively. The minus sign corresponds to the creation of a phonon (highlighted in red in Fig. 2.3.3). In contrast, the positive sign indicates a phonon annihilation (shown in blue).

As a direct consequence, the phonons located at the Γ point of the phonon dispersion, in the case of solids,—carrying no momentum—are Raman active.

A simplified exemplary Raman spectrum is shown in Fig. 2.3.3**b**. Here, the inelastically scattered light is detected symmetrically around the incident laser energy, i.e., the Rayleigh scattered light. The peaks are presented in relative wavenumbers with respect to the incident laser energy, allowing easy identification of the phonon energies. Furthermore, the Stokes spectrum is displayed with positive energy values, as is standard practice. The Raman intensity is a measure of the scattering probability as it depends on the phonon population, which follows the Bose-Einstein distribution. As a result, the anti-Stokes peak is typically weaker and vanishes at low temperatures.

Vibrational modes are Raman active if their polarizability is influenced by lattice motion, i.e., the polarizability changes. The Raman intensity I_{R}, hereby, can be expressed by the relation

$$I_{\mathrm{R}} = |\boldsymbol{e}_{\mathrm{s}} R \boldsymbol{e}_{\mathrm{i}}|^2. \tag{2.3.3}$$

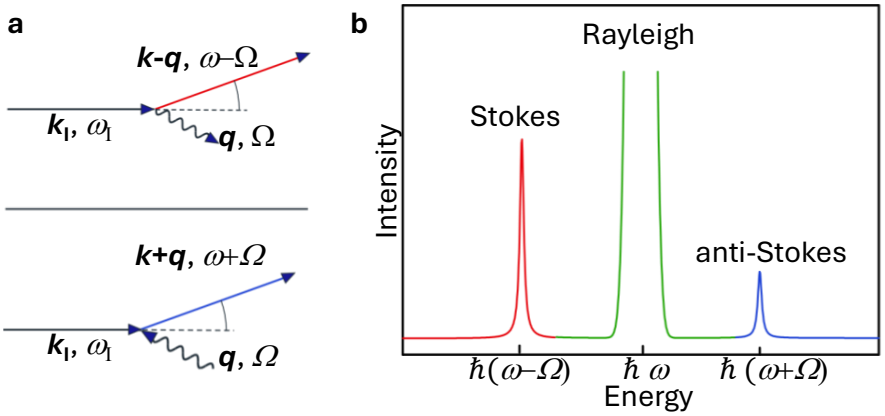

Figure 2.3.3 | a Scattering diagram and **b** Raman spectrum of scattered light. The elastically scattered light does not experience a change in energy. The Stokes (red) and anti-Stokes (blue) Raman scattering processes are of lower and higher energy, respectively.

Here, $\boldsymbol{e}_\mathrm{i}$ and $\boldsymbol{e}_\mathrm{s}$ are unit vectors of the electric field for the incident and scattered light, respectively. R denotes the Raman tensor, which is a second-rank tensor. From this equation on Raman intensities, it becomes apparent that polarization-dependent detection provides a tool for identifying Raman modes [152]. In TMDC MLs, the most prominent Raman-active modes are the optical phonons $\mathrm{A_{1g}}$ and $\mathrm{E^1_{2g}}$. They correspond to out-of-plane and in-plane oscillations of the chalcogen atoms. During both oscillations, the chalcogen atoms are out-of-phase relative to the metal atom [153]. The motions are depicted in Fig. 2.3.4**a**. Furthermore, combining the momenta of multiple phonons can satisfy momentum conservation. Such sum- or difference-processes are thus Raman-active. An overview of phonons and their resulting Raman signatures in TMDCs is provided in several publications [154–161] and review articles [152, 153, 162–165].

Another important parameter influencing the Raman intensity is the excitation energy. In the general case, the excitation promotes the system to a virtual state before it relaxes back to the ground state. However, if the excitation energy is resonant with an electronic or excitonic transition, the Raman scattering process is strongly enhanced. Formally, this can be expressed with third-order time-dependent perturbation theory, compared to the second-order nonresonant case [150, 152]. In this picture, one or more of the previously virtual states coincide with real intermediate states, giving rise to resonant or double-resonant Raman scattering. These processes can be further distinguished as incoming or outgoing resonances, depending on whether the excitation

or emission step is resonant. A schematic illustration of these three resonant Stokes processes is shown in Fig. 2.3.4**b**.

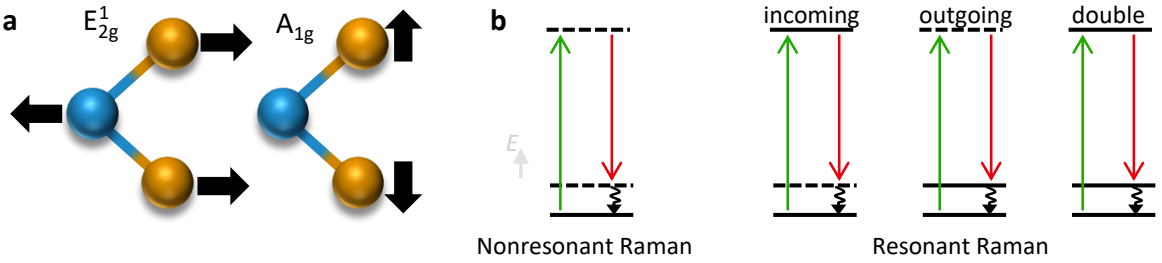

Figure 2.3.4 | a E^1_{2g} and A_{1g} intralayer Raman modes. **b** Energy levels of Raman scattering events involving virtual states or excitonic resonances. Dashed lines indicate virtual states, while solid lines represent excitonic resonances.

Resonance alone is insufficient to enhance Raman scattering, as the effective coupling between the electronic and phononic systems is also essential. Two primary mechanisms govern this electron-phonon interaction [166].

First, the deformation potential interaction arises from the motion of atoms in a lattice. Since they move more slowly than electrons, the electron cloud experiences a time-dependent potential. This changes the electrons' energies and, therefore, their spatial distribution, leading to electron-phonon coupling [167, 168].

Second, in polar materials, lattice vibrations generate oscillating electric fields by displacing positive and negative ions. These fields, in turn, couple to the electron cloud in the so-called Fröhlich interaction. As TMDCs are polar materials, influences on phonon scattering, exciton lifetimes, and resonance effects must be considered (c.f. Fermi-polaron picture in Section 2.2) [116, 151, 169–178].

This introduction to applied optical methods provides a basis for understanding the experimental results presented in this thesis. Prior to this, the experimental setups and sample fabrication techniques employed throughout this work are presented.

Chapter 3

Experimental techniques and fabrication for 2D bilayer spectroscopy

Before presenting the experimental results of this thesis, this chapter introduces the spectroscopy setups and sample fabrication techniques employed. The experiments are conducted in two separate laboratories. One is designed for nonresonant sample characterization, and the other is optimized for resonant Raman spectroscopy. Both setups will be described in the following, with particular emphasis on the equipment, configurations, and parameters used during the optical experiments. Following this, the sample fabrication processes will be outlined.

3.1 Optical spectroscopy setups

The similarities between the two experimental setups are introduced first, as the key differences lie in the lasers and spectrometers used. All samples are mounted on a Steinmeyer x–y stage with a positioning accuracy of approximately 100 nm, and all experiments are performed in backscattering geometry. For low-temperature measurements, a continuous-flow cold-finger cryostat (Konti Micro, CryoVac GmbH) is used, enabling sample temperatures down to ≈ 4 K. Optionally, the sample can be contacted inside the cryostat to two external voltage sources (SMU-Standardseries 2400, Keithley). The excitation power is controlled using a variable optical density filter wheel, and the laser beam is focused onto the sample using a 100× objective (Plan SLWD,

Nikon) with a numerical aperture of 0.7. The backscattered signal is coupled into the detection path with a 90 : 10 cube beam splitter (CBS). A white LED, a camera, and a foldable 50 : 50 CBS are integrated into the optical path for sample illumination and positioning, with minor variations between the two setups. From this point, the two experimental configurations diverge and will be described separately. The nonresonant laser spectroscopy setup, shown in Fig. 3.1.1**a**, is discussed first.

Nonresonant characterization laboratory

A continuous-wave (cw), solid-state, single-mode laser (Excelsior, Spectra-Physics) with an excitation energy of 2.3305 eV is used as a narrow-bandwidth source of excitation. Higher modes are filtered using a bandpass (BP) afterwards. For absorption measurements, a tungsten–halogen lamp (SLS301, Thorlabs) serves as a broadband white-light (WL) source. High resolution is achieved using a 75 μm pinhole as a point-like source. Therefore, the WL is focused on this pinhole before collimating the light. The spot size, at the sample, is approximately 3 μm for the WL and 1 μm for the green laser.

In the detection path, the backscattered signal can be analyzed using two separate setups. First, it can be spectrally filtered using three Bragg notch filters (BNF-532-OD3-11M, OptiGrate), enabling access to low-frequency (LF) Raman modes. Alternatively, a spatial filter consisting of two 5 cm-focal-length lenses and a 30 μm pinhole, in combination with a long-pass filter, can be used to reduce the collection spot size. The filtered signal is then focused into a spectrometer (Acton SP 2750, Teledyne Princeton Instruments) equipped with gratings of 150, 600, or 1800 grooves/mm. The detection is performed using a back-illuminated, Peltier-cooled CCD camera (Pixis 100BR eXcelon, Teledyne Princeton Instruments).

Both the excitation and detection paths can be manipulated using linear polarizers (LPs) in combination with $\lambda/2$ or $\lambda/4$ wave plates, enabling full polarization control. Unless otherwise stated, all experiments are performed in an unpolarized detection configuration.

The relevant experimental configurations for this thesis, gained in the nonresonant laboratory, are introduced in the following and differ between nonresonant LF Raman, μPL, and absorption spectroscopy.

Nonresonant LF Raman measurements are performed under ambient conditions using Bragg filters to reduce the Rayleigh scattered light intensity. This allows for the detection of low-energy Raman modes. The used excitation power is 2.5 mW. The spectrometer grating of 1800 grooves/mm is used for all measurements. The Stokes and anti-Stokes modes are then centered around the Rayleigh peak. Two polarization configurations are employed: co-polarized and cross-polarized. In the co-polarized configuration, the Raman signal is detected with linear polarization parallel to the excitation. In the cross-polarized configuration, the detection polarization is orthogonal to the excitation.

μPL measurements are performed at a temperature of ≈ 4 K with an excitation power of 25-50 μW. To enhance signal quality, Rayleigh-scattered light is suppressed using a BP filter. A spectrometer grating with 150 or 600 grooves/mm is used for all measurements.

Absorption measurements are performed using the WL source, with appropriate integration times and, in some cases, the spatial filter to improve spatial resolution. The subtle changes are monitored using differential reflectance (DR), where the reference reflection spectrum R_{ref} in Eq. 2.3.1 is obtained by modifying the sample's absorption through external influences rather than by changing the sample location [179, 180]. In this work, R_{ref} is recorded in backgate controllable doping devices at high free-carrier densities, where Pauli blocking and Coulomb screening suppress the exciton oscillator strength. While the exact carrier density is unknown, the used spectra resemble that of free-carrier plasma, providing a suitable baseline for DR analysis [116, 133, 138, 181–184]. DR should not be confused with differential reflectivity, where the time-resolved transient absorption is investigated in pump-probe experiments.

Resonant Raman laboratory

The second laboratory, illustrated in Fig. 3.1.1**b**, employs a cw Ti:Sapphire laser (3900S, Spectra-Physics), pumped by a Millenia Pro laser. The laser is tunable over the spectral range of 675–1100 nm. Higher-order modes are suppressed using a tunable volume Bragg grating filter (Photon etc.) in the spectral range of 715–790 nm. The laser beam is broadened and dispersed by this filter, which is compensated for by an inverse beam

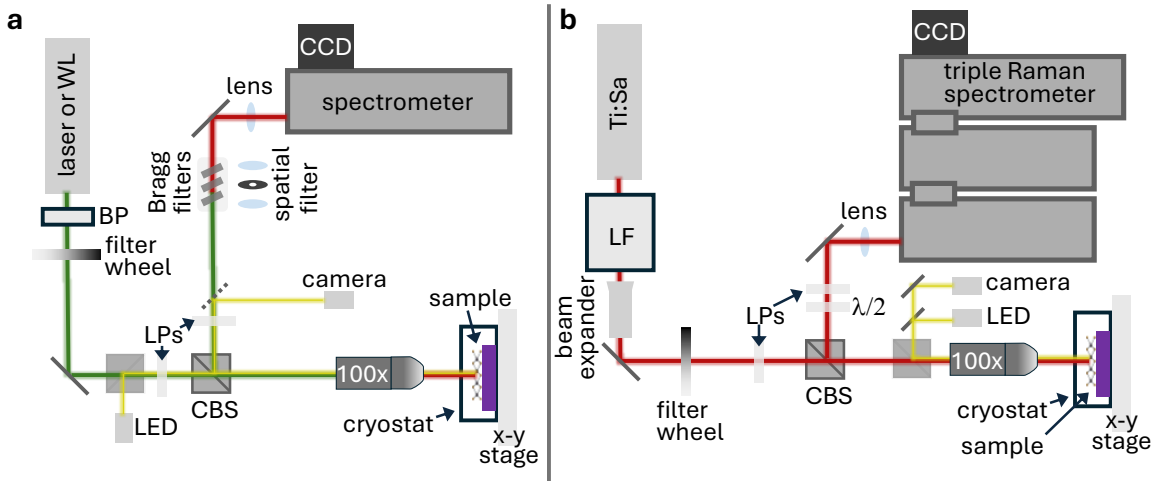

Figure 3.1.1 | Schematic illustration of the **a** nonresonant and **b** resonant spectroscopy setups.

expander. After focusing on the sample, the resulting laser spot size is approximately 1.5 μm.

A 2.3305 eV laser (GL532LN, Shanghai Laser & Optics Century Co., Ltd.) can be coupled into the excitation path as an alternative excitation source.

The collected signal is directed into a triple Raman spectrometer (TriVista, Princeton Instruments) operated in subtractive mode. The first two monochromators, which block the Rayleigh scattered light, have gratings of 900 grooves/mm. the third monochromator uses a grating with 600 grooves/mm. The spectra are recorded using a liquid-nitrogen-cooled CCD camera.

Due to the polarization sensitivity of the spectrometer grating—particularly to horizontally polarized light in the near-infrared region—the setup operates by default in a cross-polarized detection configuration.

Resonant LF Raman measurements are performed at approximately 5 K using an excitation power of $\approx 800\,\mu$W. Due to the subtractive mode of the triple Raman spectrometer, only the Stokes spectrum is recorded. As the Raman shift cannot be corrected by comparing the Stokes to the anti-Stokes energies, the A_{1g}, E^1_{2g} intralayer phonon modes of $MoSe_2$ or WSe_2 are compared with corresponding nonresonant low-temperature measurements [185–187].

For comparability across the heatmaps presented in the following chapter, all spectral intensities are normalized by the respective integration time. The RF signal is quantified by evaluating the intensity at an arbitrary Raman shift of 12 cm^{-1}, unless

stated otherwise. The resonance profile of the oscillator is obtained by performing an excitation-energy scan, and the LF Raman mode intensities are extracted by subtracting the RF background. The low-energy region—excluding the Raman mode's energy—is fitted with an exponential decay function in order to describe said background.

Magneto-PL measurements are performed using the same Ti:Sapphire laser in combination with a 5 T magneto-cryostat (MicrostatMO, Oxford Instruments). Precise sample positioning within the cryostat is enabled by two retrofitted horizontal linear stepper stages (ANPx51/RES Nanopositioners, attocube systems GmbH) mounted inside the sample chamber. The resulting change in the sample's vertical (z) position reduces the effective magnetic field at the sample to approximately 4.5 T.

To enable circularly co-polarized measurements, additional $\lambda/4$ wave plates are incorporated into both the excitation and detection paths, in combination with LPs.

3.2 Sample fabrication process

The success of experimental investigations critically depends on both sample quality and reproducibility. Therefore, the sample fabrication plays a crucial role. In this work, all utilized materials are vdW materials, sourced through various techniques. MLs and few-layer flakes are obtained either by mechanical exfoliation from artificially grown bulk crystals [25, 88] or by chemical vapor deposition (CVD) growth. Subsequently, precise stacking techniques are employed to fabricate artificial hetero-BLs and devices.

All bulk TMDC crystals were purchased from HQ Graphene, while the hBN crystals were provided by Dr. T. Taniguchi and Dr. K. Watanabe (National Institute for Materials Science, Tsukuba, Japan). All investigated samples were fabricated using different procedures. The detailed fabrication steps for all techniques applied in this study are presented in the following sections.

3.2.1 Exfoliation

Exfoliation begins with the mechanical cleavage of a high-quality bulk vdW crystal using adhesive tape (Scotch Magic tape). For hBN and graphite, this is followed by

a second careful cleavage using the same tape. In contrast, for TMDCs, a blue tape with lower adhesive strength (polyvinyl chloride backgrinding tape SPV-224PR, Nitto Denko Corp.) is employed to minimize material loss and preserve thinner layers.

The yield depends on several factors, such as crystal size, thickness, and peeling speed. For hBN, a standard method involves placing a single crystal on one piece of tape and repeatedly cleaving it with another tape—ensuring no overlap during the process—to achieve thinner flakes.

The resulting few-layer flakes on the tape can then be used in two downstream approaches, as described in the following sections.

First, a viscoelastic polymer stamp can be employed for flake transfer. The polydimethylsiloxane (PDMS) (WF-20-X4/PF-30-X4, Teltex GmbH) is a viscoelastic material, i.e., it acts like a liquid under low stress and like a solid under high stress. The PDMS stamp is fixed onto a glass slide, and the adhesive tape containing exfoliated crystals is slowly brought into contact with the PDMS surface. Adhesion strength and tape removal speed are critical parameters that determine the transfer yield of crystals onto the stamp. Upon successful exfoliation, MLs or other target flakes can be identified via optical contrast using an optical microscope.

Second, the exfoliated flakes can be directly deposited onto a heated silicon wafer with a 90 nm amorphous SiO_2 capping layer. The substrate must be thoroughly cleaned beforehand. This involves successive ultrasonic baths in acetone, isopropyl alcohol, and high-purity water, followed by baking in a plasma oven to remove residual organic contaminants. As with PDMS-assisted exfoliation, the optical contrast of the flakes is thickness-dependent, and experienced users can visually identify MLs under an optical microscope. The flake thickness can also be estimated by comparing it to established optical contrast data from the literature [188, 189] or by direct measurement using atomic force microscopy (AFM).

In general, the yield and lateral size of MLs obtained via direct exfoliation onto Si/SiO_2 are lower compared to those gained with the PDMS-assisted method. The main advantage of the former lies in the higher quality of the resulting flakes, as PDMS contamination can be effectively avoided. For ML stacks, avoiding such contamination is essential to ensure sample homogeneity. Due to the inherently low ML yield from exfoliation, CVD grown ML TMDCs are partially used in this thesis. These are syn-

thesized at Prof. Högele's laboratory in Munich and at Prof. Turchanin's group in Jena. The resulting flakes are later used in one of the following two stacking techniques.

3.2.2 All-dry viscoelastic stamping

One possible fabrication method is the "all-dry viscoelastic stamping" technique established in Ref. [190]. For this stacking approach, all flakes must be exfoliated onto PDMS. The employed microscope and stamping setup are depicted in Fig. 3.2.1**a**. The glass slide containing the TMDC flake is inverted and mounted on an x-y-z stamping stage. A p^{++}-doped Si/SiO_2 substrate (with a 285 nm oxide layer) is placed on a copper heating block. A gold coordinate system is pre-patterend to aid navigation. A low-pressure pump secures the substrate during processing.

Using a 10× objective, or optionally a glass-corrected 20× objective, and an x-y-z translation stage, the desired flake on the PDMS can be located and precisely positioned. Contact between the flake and the substrate is established gradually, as is indicated by a distinct change in optical contrast. A controlled retraction of the contact area—achieved via the z-axis micrometer screw—results in the transfer of the flake. Alternatively, heating and cooling the copper block induce thermal expansion and contraction of the PDMS, enabling a uniform, high-quality transfer.

This process can be repeated to fabricate artificially stacked multilayers. The twist angle between flakes can be roughly estimated by aligning their edges, as TMDCs tend to cleave along their main crystallographic axes [191]. A rotation stage beneath the heating block facilitates this alignment. For homobilayers (homo-BLs), the "tear-and-stack" method can be employed, where a single flake is partially transferred, torn, optionally rotated, and transferred again to achieve precise twist-angle control [192].

After stacking, an annealing step in a cryostat at 400-420 K helps agglomerate PDMS residues and airborne adsorbates into isolated bubbles. This relieves interfacial strain near the bubbles and enhances layer contact [193]. When multiple stacking steps are required, thermal stamping is recommended after each transfer to progressively encourage lattice relaxation, rather than relying solely on a final annealing step. An exemplary microscope image of an edge-aligned and annealed $MoSe_2$–WSe_2 heterostructure is shown in Fig. 3.2.1**b**.

By acquiring frequency-modulated (FM) AFM images, structural features such as bubbles, wrinkles, residues, and even adsorbates can be resolved. These measurements were

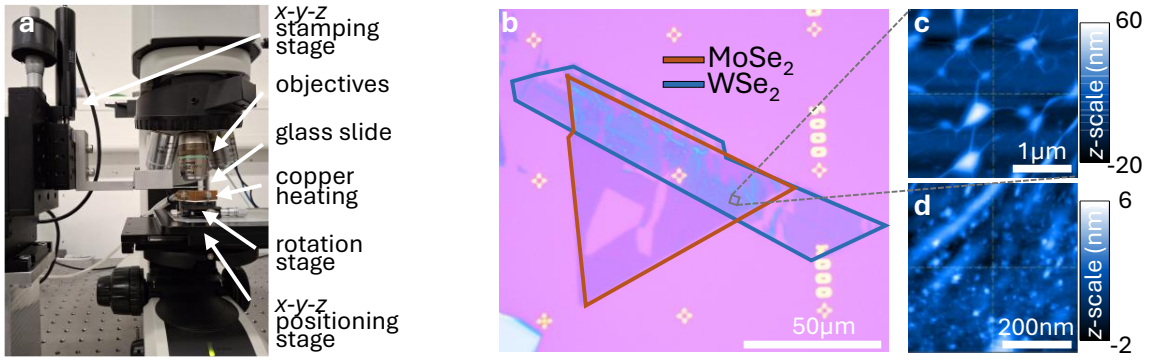

Figure 3.2.1 | a Optical microscope setup used for exfoliation and sample fabrication. **b** Microscope image of an exemplary $MoSe_2$–WSe_2 hetero-BL on a Si/SiO_2 substrate after annealing. The relative twist angle between the layers can be estimated to be either 0° or 60° based on the alignment of their edges. **c**–**d** FM-AFM images of the region shown in **b**, taken at different magnifications. In **c**, PDMS residue bubbles are visualized on a length scale comparable to the laser spot size used in optical experiments. In **d**, additional inhomogeneities, such as wrinkles and surface residues, are resolved in greater detail.

performed by Dr. K. Pürckhauer and are shown in Figs. 3.2.1**c**–**d**. The bubbles appear on a length scale comparable to the laser spot size used in optical experiments, making their influence non-negligible.

When additional stamping steps are introduced—for example, to integrate graphite stripes for controlling charge carriers or applying an external electric field—the resulting structures often become too inhomogeneous. To overcome these limitations, the alternative, polymer-free fabrication technique known as “hot pickup” is employed.

3.2.3 Hot-pickup method

Before starting the stamping process, a PDMS substrate is prepared by mixing PDMS and a curing agent (Dowsil 184) in a 10:1 weight ratio, followed by an ultrasonic bath to ensure homogeneity. A small droplet of this mixture is then applied to a heated microscope slide using a pipette or a toothpick, resulting in a hemispherical PDMS dome.

Next, a thin polycarbonate (PC) film is prepared. Here, a solution consisting of 5% PC and 95% chloroform by weight is drop-cast onto a glass slide. The solution is then spread evenly by pressing a second glass slide on top and sliding them apart. All slides are heated to 80°C afterward to evaporate the chloroform, leaving behind a thin PC

film. This film is then transferred onto the PDMS dome using a tape-based template, thereby forming a stamp.

The sample is assembled by sequentially stacking the individual layers using the PDMS-PC stamp, following a slightly modified version of the procedures described in Refs. [194, 195]. The stamp is inverted and mounted onto the x-y-z stamping stage. Before the stamping process can start, a thorough plan for the sample, including the position and rotation of each component, is needed. The transfer itself begins by approaching the substrate adjacent to the first hBN flake at a temperature of 125°C. Due to thermal expansion, the stamp makes contact with the hBN crystal. Upon cooling, the stamp contracts, thereby picking up the flake onto the PC layer. In subsequent pickup steps, vdW forces between the 2D materials exceed those of the substrate, enabling an iterative assembly of the planned heterostructure.

Subsequently, the completed stack is placed onto the final substrate, and the PC is melted off at 175°C. The sample is then cleaned via sequential chloroform and isopropyl alcohol baths, leaving only the assembled heterostructure. If electrical contacting is required, the final substrate is chosen to include pre-patterned gold or platinum electrodes. It is mounted onto a ceramic chip carrier using conductive silver lacquer. Finally, aluminum (or optionally gold) wires are bonded to the contact pads, allowing the application of external voltages during experiments.

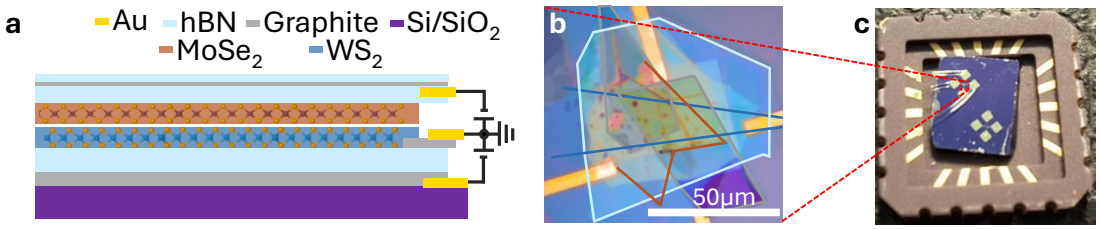

Figure 3.2.2 | a Schematic illustration of the dual-gated $MoSe_2$–WS_2 R-type heterostructure device (sample R8, fabricated by N. Paulik). **b** Optical microscope image of the same device, showing the individual layers. **c** Macroscopic image of the bonded and mounted sample fixed onto the ceramic chip carrier using conductive silver lacquer.

A schematic of the exemplary $MoSe_2$–WS_2 device R8, fabricated by N. Paulik, an optical microscope image, and a macroscopic image of the assembled device are shown in Figs. 3.2.1**a**–**c**. This specific device can be understood as follows: the $MoSe_2$ and WS_2 MLs are stacked at 0°, rendering an R-type heterostructure. The WS_2 flake is contacted by a graphite stripe, which functions as the ground contact. The hetero-BL is encapsulated between two hBN flakes with a thickness of 10 to 20 nm, which is

determined via optical contrast. A top- and a bottom graphite flake function as top- and bottom gates, allowing for an electrostatic doping by an external voltage source (SMU-Standardseries 2400, Keithley). The whole stack is hBN capped. All three graphite flakes are in direct contact with separate gold electrodes, which are bonded to the contact pads via aluminum wires. Devices with only a single gate miss a graphite and an hBN stripe.

Even a brief look at the fabrication process reveals that sample fabrication is a broad, continuously evolving field of research. Consequently, all samples used in this thesis are fabricated with slight variations. The experimental results presented during this thesis are, in part, made possible by the high-quality samples provided by my colleagues Dr. J. Holler, Dr. P. Nagler, M. Scheuck, F. Buchner, N. Maier, N. Paulik, J. Lichtenberger, and L. Sichert, whose contributions are gratefully acknowledged.

Chapter 4

Optical signatures of moiré and reconstructed van-der-Waals bilayers

Having established the theoretical foundations of TMDCs in the ML limit, this thesis now shifts focus to a more complex system: vdW BL structures. Recent advances in angle-aligned bi- and multilayers have unveiled a variety of intriguing physical phenomena, including spin-layer locking between adjacent layers [96, 104–108, 196], the emergence of hybridized and every-other-layer excitons [107, 142, 197–203], and interlayer phonons [152, 204–213].

Additionally, introducing the key tuning parameter in vdW BLs—the twist angle between adjacent layers—enables the formation of moiré superlattices. This degree of freedom results in exciting discoveries, including unconventional superconductivity near the so-called magic angle in twisted BL graphene [78, 79], the fractional quantum anomalous Hall effect in twisted $MoTe_2$ BLs [73–77], and ferroelectric and multiferroic behavior in twisted TMDC BLs [59, 214–225].

The groundwork and key experimental findings during this thesis on this promising field will be presented in the following chapter, which focuses on vdW BLs and heterostructures. It first introduces the key concepts in Section 4.1, before discussing moiré superlattices and their resulting potential landscapes in Section 4.2, alongside the key experimental findings of this thesis concerning moiré physics. Finally, the focus is shifted to the phenomenon of atomic reconstruction and to its influence on vibrational and excitonic properties in Section 4.3.

4.1 Heterostructures

In 2013, Geim and Grigorieva [226] introduced their visionary perspective on heterostructures by stacking different vdW materials. By reviewing state-of-the-art fabrication techniques and the resulting groundbreaking phenomena, they spurred the scientific community to move in a collective direction toward perfect tunability and control in industrial-scale applications.

Compared with conventional transistors and electronic devices, essential electronic functionalities can be replicated in vdW heterostructures, which offer unprecedented control through layer stacking, twisting, and heterojunction engineering [227–230].

Extensive research on BLs and multilayer heterostructures composed of vdW materials has since kept Geim's and Grigorieva's perspective relevant to this day. During these studies, it was demonstrated that vdW heterostructures not only reproduce many effects known from traditional semiconductors but also enable entirely new physics. Many phenomena are hereby driven by the interplay of strong Coulomb interactions, spin-orbit coupling, moiré superlattices, and hybridization. For instance, the periodic potential created by moiré patterns has been shown to trap electrons into correlated states such as generalized Wigner crystals [67–72].

Building on these advances, engineered vdW systems hold great promise for future optoelectronic [231–233] and quantum electronic applications [234, 235], where precise tailoring of electronic, optical, and mechanical properties is possible.

This section introduces the essential concepts of vdW heterostructures. Here, the focus will be on band alignment between adjacent layers and on the formation of interlayer excitons. For a comprehensive overview of the rapidly evolving field of vdW heterostructures, the reader is referred to several recent review articles [236–245].

4.1.1 Band alignment

Before delving into this immense field of research—with its enormous possibilities for tuning properties—the fundamental principles of vdW semiconductor heterojunctions must be discussed. A helpful starting point is Anderson's rule, which states that the vacuum levels of the constituent semiconductors are aligned. Applying this rule to two materials A and B with their respective electron affinities (χ) allows for an estimate

of their band alignment and, therefore, their charge carriers' location in the respective materials. Here, χ is defined as the energy required to remove an electron from the CB minimum to the vacuum level [246].

There are three possible types of band alignment, which are determined by the relative bandgaps of the two semiconductors, as illustrated in Fig. 4.1.1**a**. Type-I (straddling gap) alignment occurs when both the conduction and valence bands of one material lie within the bandgap of the other, resulting in both electrons and holes being confined in the same material. Type-II (staggered gap) alignment features spatial separation of electrons and holes across the interface, while type-III (broken gap) alignment results in an overlap of the CB of one material with the VB of the other. In Ref. [247], Anderson's rule is extended to 2D semiconductor heterostructures, where corrections must be made to account for interlayer hybridization and dipole-induced electric fields [248].

All three band alignments are realized in vdW heterostructures. The existence of type-I heterostructures has been confirmed by various experimental groups, notably in $MoSe_2$–WS_2 BLs [58, 60, 249] and in $MoTe_2$–WSe_2 BLs [250]. Type-II heterostructures are theoretically predicted in Refs. [251–255] and subsequently confirmed experimentally [49, 50, 256]; see also [257] for an overview. Type-III band alignments have also been realized in various vdW heterostructures to exploit their charge-transfer characteristics [258–260]. However, the focus of this thesis will remain on type-I and type-II band alignments, which are shown in the band-alignment schematic at the K points in Figs. 4.1.1**b-c**, where the individual materials are color-coded. The spin-configurations are indicated by arrows in Figs. 4.1.1**b**.

The band alignment is not as straightforward as theoretical calculations may suggest, as demonstrated by the extended debate surrounding $MoSe_2$–WS_2 hetero-BLs. Here, the CBs of WS_2 and $MoSe_2$ lie in close energetic proximity, making the spin-subband ordering crucial (see Fig. 4.1.1**b**) and requiring experimental verification. Ultimately, experimental studies confirmed that $MoSe_2$–WS_2 heterostructures exhibit type-I band alignment in the R-type stacking [58, 60, 249]. In contrast, a type-II alignment is observed only for the H-type stacking under an applied out-of-plane magnetic field [60, 249]. This conclusion is supported by magneto-optical experiments [58, 60, 249].

As a direct consequence, there is a possibility of new quasi-particles forming, where the exciton's individual charges are separated across adjacent layers—the interlayer excitons.

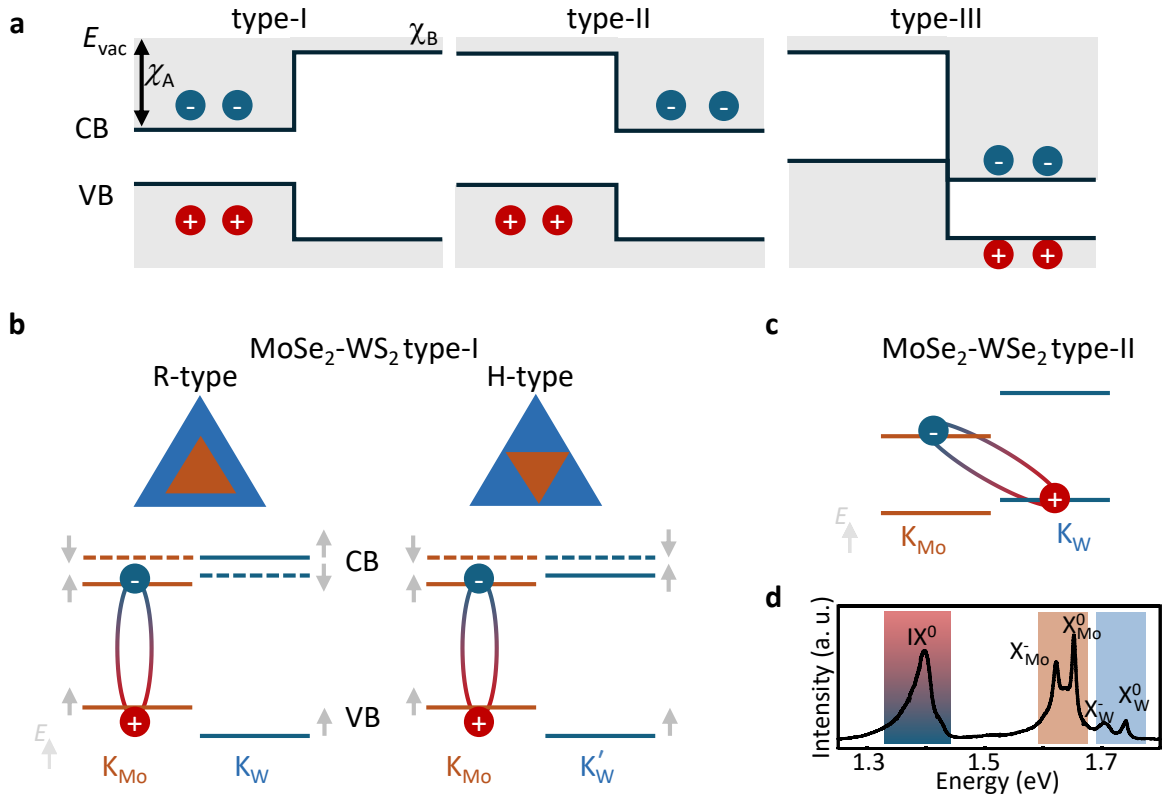

Figure 4.1.1 | a Schematic of type-I, type-II, and type-III band alignment with electrons and holes situated in VB maxima and CB minima in respective configurations. **b** Schematic of R- and H-type $MoSe_2$-WS_2 type-I band alignment at K points. The lowest energy Coulomb-bound electron-hole pairs are marked. $MoSe_2$ (WS_2) material and bands are orange (blue). The spin up (down) configuration is indicated by upward (downward) facing arrows and drawn-through (dashed) lines. **c** Schematic of $MoSe_2$-WSe_2 type-II band alignment at K points. **d** H-type $MoSe_2$-WSe_2 PL spectrum with marked intra- and interlayer exciton peaks (adapted from Ref. [50]).

4.1.2 Bright interlayer excitons

Interlayer excitons can emerge in both natural and artificially-stacked vdW material systems [49, 141, 198, 239, 247, 261–263], with this thesis focusing on type-II vdW hetero-BLs. In those strongly coupled heterostructures, it is energetically favorable for the carriers to relax to their lowest energy state, which involves charge transfer between the layers [49, 50, 252, 253]. Thereby, the electron relaxes to the CB and the hole to the VB, which are situated in the two opposite layers as is illustrated in Fig. 4.1.1**c**.

These charge transfer processes occur on ultrafast timescales [264–267] and result in the formation of spatially indirect, permanent dipoles [49, 247], as electrons and holes reside in separate layers while remaining Coulomb-bound. These interlayer excitons (IX^0)

possess large binding energies [268] and exhibit a low oscillator strength due to their indirect character [269, 270]. They are long-lived as a consequence [50–52]. They can be probed using magneto-PL techniques [51, 271–276] (see Section 4.3), while their interlayer character is revealed through the Stark shift observed in electric-field-dependent studies [198, 239]. In $MoSe_2$–WSe_2 hetero-BLs, this interlayer charge transfer leads to a decrease in the intralayer exciton population and, therefore, to the intralayer PL quenching. The distinct IX^0 PL emerges. An exemplary PL spectrum displaying both inter- and intralayer PL peaks, adapted from Ref. [50], is shown in Fig. 4.1.1**d**.

The type-II band alignment is not the only factor influencing the electronic structure. Density functional theory calculations reveal hybridization of the electronic bands across both layers at the Q valley of the CB and the Γ point of the VB (see Fig. 4.1.2**a**) [187, 269, 277, 278]. Since the global energy minimum for free electrons lies at the Q valley, the resulting electron wavefunction is delocalized over both layers. Analogous to the behavior observed in MLs, interactions between these free charges and intra- and interlayer excitons lead to the formation of charged excitonic complexes.

In the intralayer exciton case, they interact with the hybridized electron sea, leading to the formation of hybridized Fermi polarons or, at low charge densities, hybridized intralayer trions (HX^-). The resulting excitonic complexes in $MoSe_2$-WSe_2 hetero-BLs are schematically illustrated in the single-particle representation in Fig. 4.1.2**b**. A notable consequence is the emergence of a trion-phonon coupling [187] in a specific lattice configuration, which will be discussed in detail in Section 4.3.

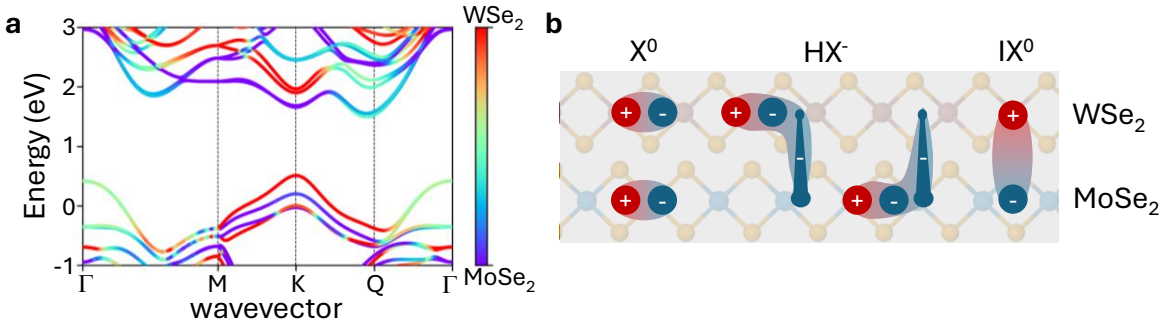

Figure 4.1.2 | a Layer-projected band structure of H-type $MoSe_2$-WSe_2 hetero-BLs. The band layer contribution is color-coded. The bands in the K valley exhibit negligible hybridization and a type-II band alignment. Additionally bound electrons are situated at the Q points, and are strongly hybridized over both layers (adapted from Ref. [187]). **b** Schematic real-space illustration of excitonic complexes in $MoSe_2$-WSe_2 hetero-BLs shown in side-view. The $MoSe_2$ and WSe_2 X^0 exist next to their hybridized negatively charged counterpart HX^- alongside the IX^0.

The properties of IXs and their charged states will now be explored to better understand the $MoSe_2$-WSe_2 interlayer PL spectra, introduced in the same Section 4.3.

In H-type $MoSe_2$–WSe_2 hetero-BLs, the energy minima at K valley band structure become relevant. The 60° rotational twist between the constituent MLs results in the K (K′) valley of the WSe_2 VB being aligned with the K′ (K) valley of the $MoSe_2$ CB. The spin-splitting in the $MoSe_2$ CB results in two energetically distinct states when an IX^0 is formed. Here, the lower-energy state is a spin-forbidden triplet state IX^0_T. It involves parallel spins of electrons and holes. The higher-energy state is a spin-allowed singlet state IX^0_S [273, 279–283]. These transitions are schematically depicted in Figs. 4.1.3**a** and **b**, for the hole located in the WSe_2 VB at the K point. Here, the color is indicative of the exciton being optically dark or bright.

These excitonic complexes can lower their energy by binding an additional hybridized electron located at the Q and Q′ valleys, forming charged IXs denoted as IX^-_T and IX^-_S. The experimentally observed energy shifts between these complexes and their relative PL intensities, extracted from low-temperature, nonresonant μPL measurements, are shown in Fig. 4.1.3**c** (following Ref. [279]).

One additional peak, labeled $IX^-_{T^*}$, may hereby originate from an IX_T bound to an electron at the $MoSe_2$ K′ spin-up valley, as hypothesized in Ref. [279]. Alternatively,

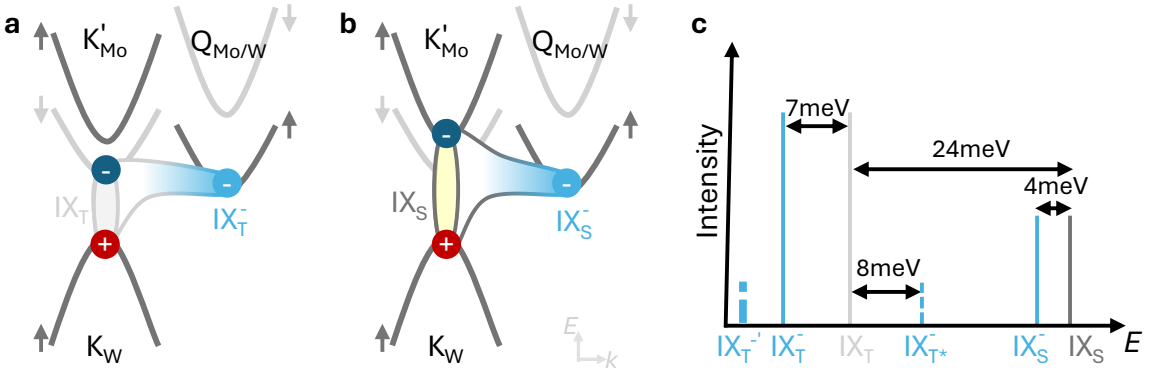

Figure 4.1.3 | Schematic representation of charge configurations for IXs and their charged counterparts in H-type $MoSe_2$-WSe_2 hetero-BLs: **a** IX_T and IX^-_T, and **b** IX_S and IX^-_S, illustrating optical transitions involving a hole in the WSe_2 VB and an electron in the $MoSe_2$ CB at the K point. The spins of the involved bands are color-coded and indicated by arrows. The additionally bound electron is hybridized over both layers at the Q valley and is color-coded in light blue. **c** Schematic of exciton energies and the expected intensities in low-temperature μPL experiments for the excitonic complexes shown in **a** and **b**, following Ref. [279].

this peak may result from differing binding energies associated with electrons located at the Q- versus Q′ valleys, a scenario discussed for WSe_2 homo-BLs in Ref. [203].

A lower-energy resonance, labeled $IX_T^{-'}$, is attributed to either a Mahan-like exciton [284] or an exciton-plasmon-like excitation, as discussed in theoretical ML studies [179, 285].

When investigating charge-tunable devices in the hole-doping regime, the formation of positively charged interlayer excitons, IX_T^+ and IX_S^+, is expected. These arise from the binding of an additional hole at the WSe_2 K′ valley [273].

Taken together, these assignments establish a consistent picture of the interlayer excitonic landscape in H-type $MoSe_2$–WSe_2 hetero-BLs and provide the foundation for the analysis presented in Subsection 4.3.2.

4.2 Moiré superlattice

For this section, the vdW BL lattice is of central interest. If two lattices with a lattice mismatch are combined, or by introducing a finite twist between the layers, an interference pattern emerges, which can be described as a novel superlattice. This is called a moiré lattice and the accompanying effects, moiré effects.

Such a moiré supercell of an angle-aligned hetero-BL is shaded in gray in Fig. 4.2.1**a**. The moiré lattice constant a_m as a function of the twist angle θ is given by

$$a_m = \frac{(1+\delta)a_0}{\sqrt{2(1+\delta)(1-\cos\theta)+\delta^2}}, \tag{4.2.1}$$

where δ is the lattice mismatch, defined as $\delta = \frac{|a_1-a_2|}{a_2}$, with a_1 and a_2 denoting the lattice constants of the two MLs with $a_1 < a_2$ [238].

This new periodicity in real space gives rise to a corresponding periodicity in reciprocal space. The reciprocal moiré lattice vector is defined as $\boldsymbol{g} = \boldsymbol{b}_2 - \boldsymbol{b}_1$, where $\boldsymbol{b}_1$ and $\boldsymbol{b}_2$ are the reciprocal lattice vectors of the individual layers. The typical moiré lattice constant a_m is on the order of a few to several tens of nanometers. As a result, the first moiré BZ is considerably smaller than the first BZ of the individual MLs. This is illustrated for a hetero-BL, consisting of angle-aligned TMDC MLs with a lattice constant mismatch,

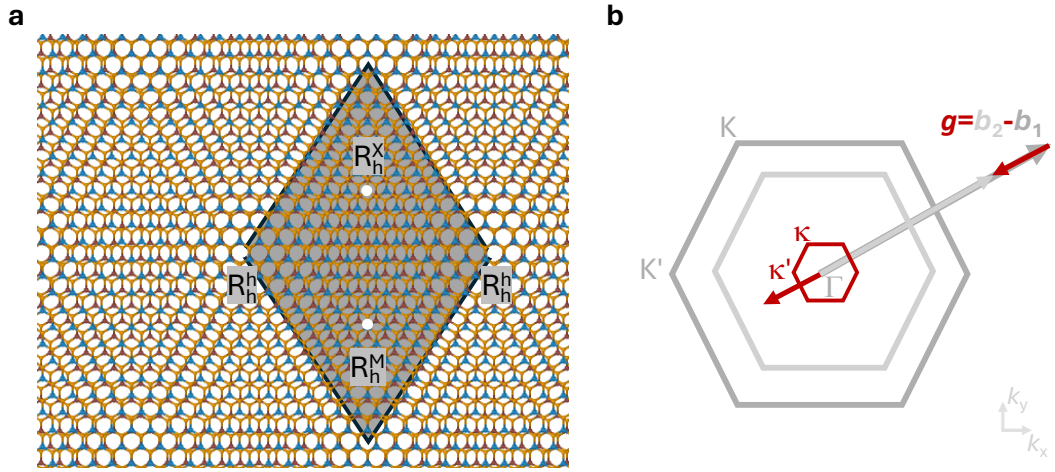

Figure 4.2.1 | Illustrations of an R-type moiré hetero-BL superlattice formed by two angle-aligned TMDC MLs with lattice constant mismatch. **a** Real-space representation, with the moiré unit cell shaded gray and the high-symmetry points, introduced in Fig. 4.2.2**a**, marked. **b** Reciprocal-space representation, with the first moiré BZ colored red. The ML contributions are gray-shaded.

in Fig. 4.2.1**b**, where the first moiré BZ is shown in red. The high-symmetry moiré points are labeled in lowercase Greek letters.

It is essential to introduce a precise nomenclature for high-symmetry stacking in the emergent supercell. This will enable a precise description of the moiré physics in the following. For this thesis, the notation of Ref. [54] is used. Here, the R- and H-type stackings are denoted as $\mathrm{R}_\mathrm{m}^\mathrm{n}$ and $\mathrm{H}_\mathrm{m}^\mathrm{n}$. The sub- and superscript letters indicate atomic sites in the bottom and top layers, respectively. Similarly to Section 2.1.1, "X" is used for a chalcogen atom site, "M" for a transition-metal one, and "h" for a hollow center.

The resulting high-symmetry stacking configurations are $\mathrm{R}_\mathrm{h}^\mathrm{X}$, $\mathrm{R}_\mathrm{h}^\mathrm{h}$ and $\mathrm{R}_\mathrm{h}^\mathrm{M}$ for R-type and $\mathrm{H}_\mathrm{h}^\mathrm{M}$, $\mathrm{H}_\mathrm{h}^\mathrm{h}$ and $\mathrm{H}_\mathrm{h}^\mathrm{X}$ for H-type stacking. These are highlighted in the moiré cell in Fig. 4.2.1**a** and are illustrated in Figs. 4.2.2**a** and **b**, respectively, where the upper (lower) layer is colored blue (red).

Each moiré superlattice contains all the characteristic high-symmetry points of either R-type or H-type stacking. Between these high-symmetry configurations, the local atomic registry varies smoothly. This smooth spatial transition is exemplified for an R-type hetero-BL in Fig. 4.2.1**a**.

In BL graphene, the discovery of so-called magic twist angles—at which superconductivity and correlated insulating states appear—has generated intense interest in the

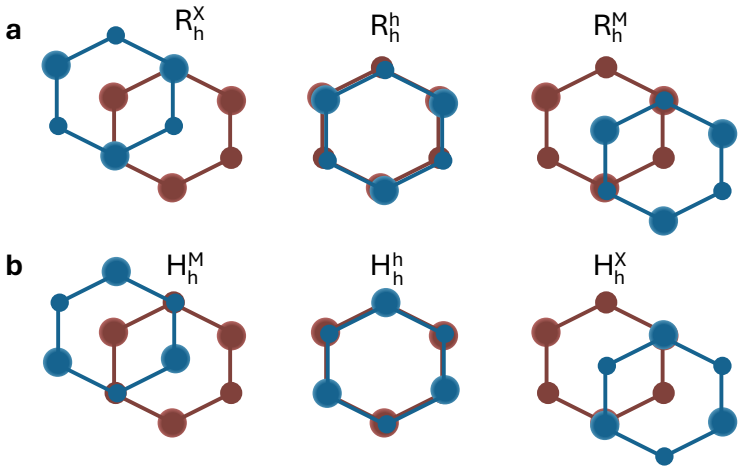

Figure 4.2.2 | Schematic illustration of high-symmetry stacking configurations in **a** R-type and **b** H-type BLs. The chalcogen atoms are represented by small circles, and the metal atoms by larger ones. The top layer is colored blue, and the bottom layer red.

emerging field of twistronics [78–81]. This research frontier has since expanded into TMDC BLs, which will be the focus of the following experimental sections.

4.2.1 Excitonic moiré potential

The basis for exciton physics, the electronic band structure of 2D materials, introduced in Chapter 2.1.2, is significantly modified by the presence of a moiré superlattice. The smooth variation between high-symmetry stacking points creates a periodic potential and dielectric landscape, leading to backfolding of the CB and VB into the first moiré Brillouin zone and the formation of moiré minibands [58, 60, 239, 286–289], when including hybridization.

For large moiré periods, the electronic potential can be approximated by the effective band masses of the constituent layers modulated by a periodic potential, producing flat minibands at the edges of the mini-BZ [241]. Free charge carriers tend to localize in the minima of the resulting moiré potential, which can be imaged using scanning tunneling microscopy [290]. Moreover, strong Coulomb interactions can lead to the formation of long-range ordered, correlated electron lattices at integer or fractional fillings ν.

As the electrons become pinned, an energy gap emerges because introducing additional electrons into the system is not energetically favorable. This gives rise to insulating

states such as the Mott insulator ($\nu = 1$), the moiré band insulator ($\nu = 2$), and generalized Wigner crystals at fractional fillings (e.g., $\nu = 1/3, 2/3$) [68].

These states have been experimentally investigated in various moiré-BL systems such as homo-BLs and WSe_2-WS_2, $MoSe_2$-WS_2, and $MoSe_2$-hBN-$MoSe_2$ heterostructures [59, 63, 65–67, 69, 70, 77, 291–298]. Evidence of the Coulomb crystal can also be provided in all-optical experiments, as it causes the backfolding process like a conventional lattice [71, 299].

The widely used term Mott insulator at $\nu = 1$ should be used with caution in moiré systems, as studies suggest that the dominant mechanism is charge-transfer insulating [300, 301]. Therefore, the general term generalized Wigner crystal will be used throughout this thesis [62, 64, 68]. Additionally, the integer- and fractional quantum anomalous Hall effects have been reported in ferromagnetic, topologically nontrivial $MoTe_2$ homo-BLs [73–77], further highlighting the rich correlated physics accessible in tailored moiré systems.

The charge filling factor ν can, hereby, be estimated using a simple parallel-plate capacitor model, which is widely applied in moiré-heterostructure studies. The equation for the charge density n is given by

$$n = \frac{\epsilon_0 \epsilon_{BN}}{e} \left(\frac{V_t}{d_t} + \frac{V_b}{d_b} \right), \tag{4.2.2}$$

where V_t and V_b are the applied voltages to the top and bottom gate, respectively. The top and bottom insulating hBN layer thicknesses are d_t and d_b, respectively. Here, ϵ_0 is the vacuum permittivity, and $\epsilon_{BN} = 3.8$ is the out-of-plane relative permittivity of hBN [302]. With knowledge of the intrinsic doping level, the thicknesses of the hBN dielectric layers—determined either via AFM or optical contrast [189]—and the moiré lattice constant, the gate voltage required to reach a specific charge filling factor can be estimated.

In the following experimental work, an intrinsic (undoped) R- or H-type $MoSe_2$-WS_2 hetero-BL with a moiré period of $a_m \approx 7.5\,\mathrm{nm}$ combined with an hBN thickness between 10 and 20 nm is used. This corresponds to a gate voltage range of $0.5 - 1.0\,\mathrm{V}$ applied simultaneously to both gates to achieve a moiré site filling factor of $\nu = 1$, which corresponds to a carrier density of $n = 2.05 \times 10^{12}\,\mathrm{cm}^{-2}$.

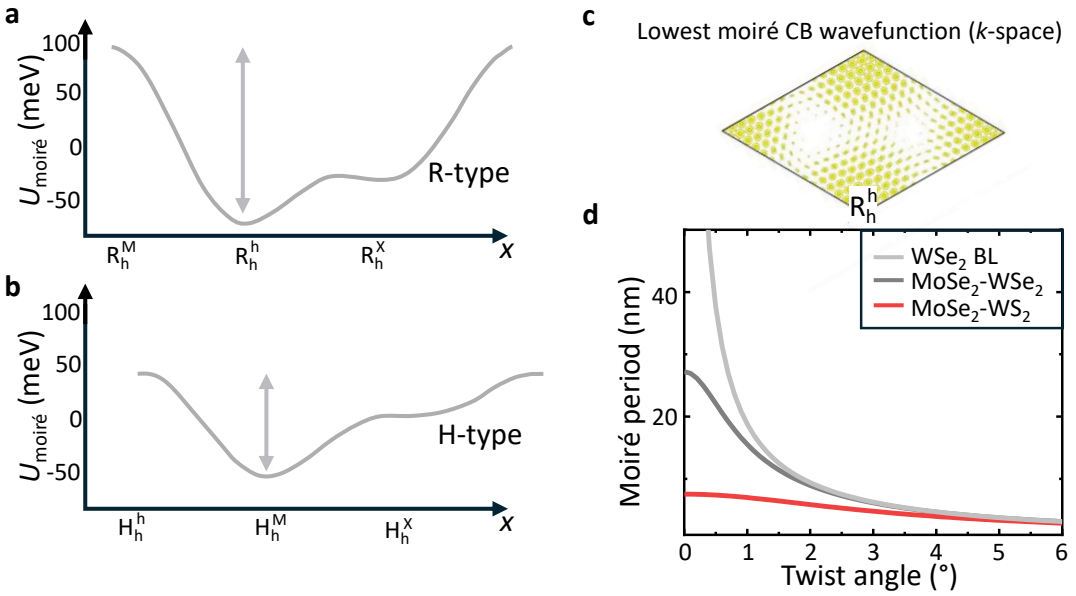

Figure 4.2.3 | Calculated moiré potential along high-symmetry stacking configurations for **a** R-type **b** and H-type $MoSe_2$-WS_2 hetero-BL (adapted from Ref. [61]). **c** Momentum wavefunction plot for lowest moiré CB of R-type $MoSe_2$-WS_2 hetero-BL (adapted from Ref. [59]). The highest probability density of the moiré exciton is found at the R_h^h stacking. **d** Calculated moiré period as a function of the twist angle from Eq. 4.2.1 for WSe_2 homo-BLs, $MoSe_2$-WSe_2 and $MoSe_2$-WS_2 hetero-BLs.

Similarly to the electronic bands, excitons in a moiré superlattice form mini-bands, which follows from either the single-particle or from the two-particle picture [60, 61, 287, 303]. The modulation of the potential landscape is, hereby, dependent on the moiré period and on the material system. The H-type moiré potential is generally shallower than that of an R-type configuration due to the spin-subband ordering in the CB of WS_2 [55, 61, 304].

Previous theoretical studies on various TMDC hetero-BL systems ($MoSe_2$-WS_2, WSe_2-WS_2, $MoSe_2$-MoS_2, MoS_2-WSe_2, and WS_2-MoS_2) show a moiré potential depth of a few meVs up to a hundred meV [53–56, 61]. The moiré excitons (M_1) in the type-I heterostructure $MoSe_2$-WS_2 can be considered as trapped quasi-particles due to the large moiré potential. The calculated potentials for R- and H-type hetero-BLs along the high-symmetry stacking configurations are shown in Figs. 4.2.3**a** and **b**, respectively [60].

Calculations on the momentum wavefunction of the lowest R-type moiré CB highlights its strong localization at the R_h^h high-symmetry point in the $MoSe_2$ layer [59–61], as depicted in Fig. 4.2.5**c**. Additionally, when calculating the moiré period of $MoSe_2$–WS_2

as a function of the twist angle, it shows little dependence on the angle in contrast to other BLs, as seen in the slopes in Fig. 4.2.3**d**. This minimum twist-angle disorder yields a highly reproducible moiré period, ideal for experimental investigations.

Together, these properties make the $MoSe_2$-WS_2 moiré heterostructure not only a promising platform for exploring correlated physics [59, 305], but also an appealing candidate for scalable device applications. In the following, the focus is specifically on $MoSe_2$–WS_2 hetero-BLs as the material platform of this thesis.

Multiple distinct moiré excitons have been observed in PL and RC measurements [59–61, 249, 287], serving as the foundation for sample characterization in this thesis. Alternatively, the moiré miniband structure can be probed via collective inter-moiré-band excitations (IMBE), observable in resonant inelastic light scattering (RILS) experiments [289]. These investigations are analogous to earlier works in GaAs-based systems [306–311]. In this three-step scattering process, an electron is first excited from a lower VB to a virtual state. It then scatters via Coulomb interaction with a charge carrier residing in a moiré miniband, promoting that charge to a higher miniband. The scattered electron-hole pair subsequently recombines under the emission of the scattered photon. As the charge carrier is scattered into a higher moiré band, it is called IMBE. This can be detected in RILS spectra, thereby granting experimental access to the underlying moiré band structure and its emergent properties.

When considering the backfolding of the exciton band structure, excited states emerge, denoted as M_2 and M_3. The energies of these moiré excitonic peaks are well-documented in the literature [59–61, 72, 249, 287, 312]. Their oscillator strength f differs distinctly between R- and H-type stacking configurations, which is shown in Figs. 4.2.4**a, b**. The calculated and experimentally measured moiré excitonic oscillators are labeled accordingly (cf. Refs. [61, 313]). The large and distinct energy gap between M_2 and M_3 in the R-type stacking, compared to the H-type stacking, enables an unambiguous identification of the stacking configuration of the $MoSe_2$–WS_2 hetero-BL samples used in this thesis, as exemplified for sample R8. The corresponding measurement, shown in Fig. 4.2.4**c**, displays the averaged sum of $-\mathrm{d}/\mathrm{d}E(\mathrm{DR})$ spectra in the charge-neutral regime. The reference reflection spectrum is taken at a calculated doping level of $n \approx 2 \times 10^{13}\,1/\mathrm{cm}^2$, according to Eq. 4.2.2, where moiré-dipole moments become vanishingly small as the system exceeds the Mott transition [181–183], where the plasma screening [314] and state-filling effects [133] dominate. The observed moiré peaks' en-

ergetic offset of $10 - 20\,\mathrm{meV}$ relative to values reported in the literature may result from a slight twist between the layers or a different dielectric environment.

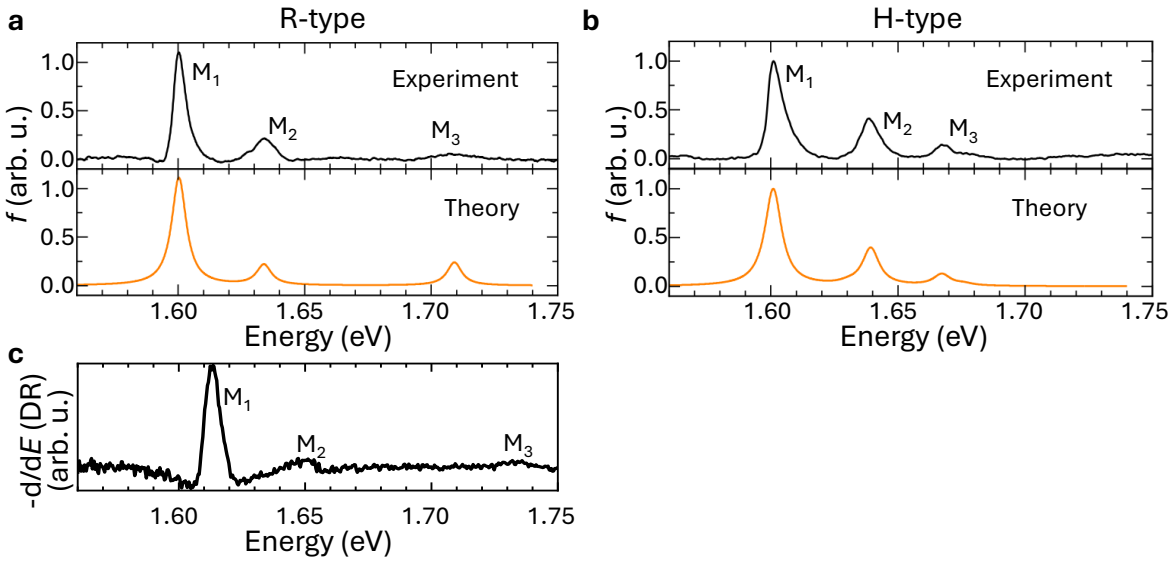

Figure 4.2.4 | Measured and calculated oscillator strength f of **a** R-type and **b** H-type $MoSe_2$-WS_2 hetero-BLs from Refs [61, 313].**c** Averaged sum of $-\mathrm{d}/\mathrm{d}E(\mathrm{DR})$ spectra of the charge-neutral regime of sample R8.

After establishing the origin of the excited moiré excitonic peaks, the spatial profile of the M_2 wavefunction—and thus its probability density—becomes important, in analogy to the localized M_1 exciton. The M_2 wavefunction, centered at the R_h^X high-symmetry stacking configuration, exhibits a non-negligible spatial extent [59, 61, 287]. Similarly, calculations for H-type stacked $MoSe_2$–WS_2 hetero-BLs show strong localization of M_1 at the H_h^M stacking point (see Fig. 4.2.3**b**), whereas M_2 and M_3 display a partial delocalization at the H_h^X and H_h^h configurations, respectively [60].

The combination of the electronic and excitonic moiré potentials in $MoSe_2$–WS_2 hetero-BLs provides a comprehensive picture of M_1 and M_2 moiré excitons' spatial distribution for both R- and H-type stacking. Furthermore, this includes their evolution into positively (M_1^+, M_2^+), negatively charged (M_1^-, M_2^-), and double-negatively charged (M_1^{2-}, M_2^{2-}) excitonic complexes, as illustrated—exemplarily for the negatively charged case—in real-space moiré-potential representation in Figs. 4.2.5**a**–**c**.

For a filling of two electrons per moiré cell, Coulomb repulsion prevents both electrons from occupying the same R_h^h or H_h^M site [287, 294, 300]. Instead, the second electron localizes at the local energy minimum at R_h^X, like in WSe_2–WS_2 moiré superlattices [73], where one electron remains fully localized and the other exhibits partial delocalization.

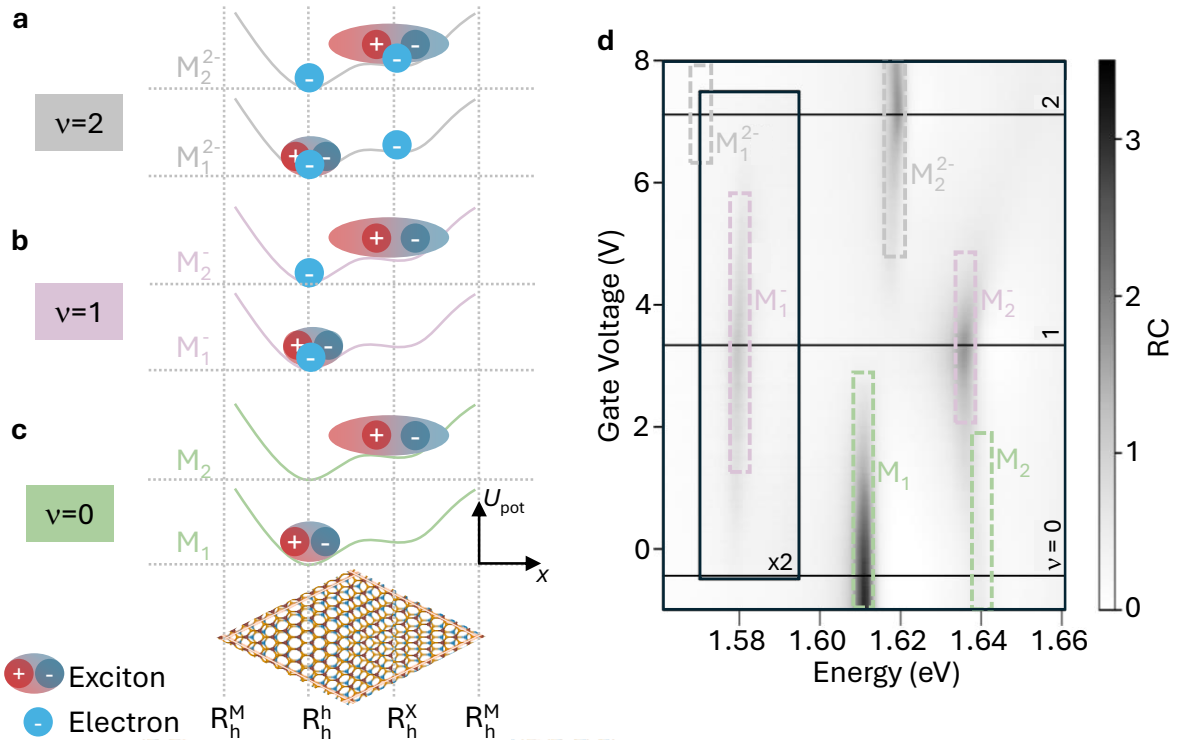

Figure 4.2.5 | Schematic of moiré excitons in real-space moiré-potential representation of an R-type $MoSe_2$–WS_2 hetero-BL at integer electron fillings $\nu = 2, 1, 0$ shown in panels **a**–**c**, respectively, indicated above a moiré cell. The moiré-trapped excitons are illustrated with finite spatial extent, while localized electrons are represented by blue charges. **d** Gate-dependent RC measurements from Ref. [59] highlight the energies of the moiré quasi-particles. The energy of M_1^{2-} is only indicated by the gray box.

An alternative scenario, that finite hopping terms for electrons exist, similar to the kinetic magnetism reported in Ref. [59], is deemed improbable or negligible as both the used excitation powers and temperatures in this thesis are well beyond the undisturbed regime of the aforementioned publication.

The spectral response in RC measurements of all excitonic complexes, including their charged states, are collected at varying symmetrically applied voltages, and are shown in Fig. 4.2.5**d**, adapted from Ref. [59].

After sample characterization and comparison with previous studies, evidence of nanoscale transfer pathways of excitonic energies between moiré sites will be presented bellow, offering fundamental insights into exciton dynamics in moiré lattices.

Programmable phonon-assisted resonant energy transfer between moiré cells

For the following experimental investigations, published in Ref. [315], a total of 14 edge-aligned $MoSe_2$–WS_2 hetero-BLs were fabricated by Nicolas Paulik during his Master's thesis [316]. A total of 10 samples are of R-type stacking, with R6, R9, and R10 functioning as single-gate devices, and R8 as a dual-gate device. In samples R8 and R9, the ground contact is connected to the WS_2 ML, whereas in R6 and R10, it is connected to both MLs. All TMDC MLs were CVD-grown in Prof. Högele's group in Munich, except the onto PDMS exfoliated WS_2 MLs in R8 and R9. The stacking order in these latter two ensures that the heterostructure interface remains PDMS-free. Additionally, four H-type samples are fabricated without gate structures, among which H3 and H4 are selected for the experiments.

Sample characterization: To characterize the samples' resonances, their emission and absorption are investigated in nonresonant μPL and white-light DR measurements. The focus of this work is placed on the R-type hetero-BL sample R8 (shown in Fig. 3.2.2**b**), as its dual-gate architecture allows the investigation of the system under zero out-of-plane electric field.

First, a PL area scan of the heterostructure region is performed to assess the interfaccial contact and sample homogeneity. The $MoSe_2$ M_1^- PL peak is fitted with a Gaussian function to extract the peak energy, which is presented in Fig. 4.2.6**a** for $U_G = 0\,V$, the PL intensity, and the FWHM. The $MoSe_2$ is identifiable in the blue region, which corresponds to a fitted energy of $\approx 1.6\,eV$. A large, homogeneous area in the center of the gated heterostructure region (marked in cyan) exhibits a clear redshift compared to this PL. Simultaneously, spots of this cyan heterostructure region show the narrowest linewidth of approximately 10 nm, gained from the Gaussian fits. These characteristics suggest high homogeneity and good interlayer contact. Equivalent PL area scans at room temperature reveal a comparable redshift, indicating that the moiré potential influences the excitonic states even when sufficient energy is introduced into the system so that the excitons' trapping is prevented—as predicted in Ref. [317].

Subsequently, low-temperature PL measurements are carried out in the identified region of high interface quality and homogeneity. A heatmap of the PL spectra as a function of symmetrically applied gate voltage is shown in Fig. 4.2.6**c**. The $MoSe_2$ PL emission is dominated by the moiré excitonic peaks M_1 and M_1^-, while the WS_2 emission shows

neutral (X_W^0) and negatively charged (X_W^-) excitons. For gate voltages exceeding $\approx 3\,\mathrm{V}$, the emergence of charged WS_2 excitons indicates population of the WS_2 CB minima, potentially due to CB hybridization across both materials.

A zoom-in of the PL heatmap to the $MoSe_2$ region is provided in Fig. 4.2.6**d**, while the corresponding DR spectra—displayed as the negative energy derivative, $-\mathrm{d}/\mathrm{d}E(\mathrm{DR})$—are shown in Fig. 4.2.6**b**. Here, the reference reflection spectrum is again obtained by increasing the doping level beyond the Mott transition. Moiré excitonic complexes are identified based on Ref. [59] and marked by vertical lines, consistent with Fig. 4.2.5**d**.

The $-\mathrm{d}/\mathrm{d}E(\mathrm{DR})$ and PL intensities of the M_1^- resonance, highlighted by pink dashed frames, are plotted normalized in Figs. 4.2.6**e** and **f**, respectively. The oscillator strength of M_1^- reaches its maximum when each moiré site hosts exactly one electron due to a reduced screening from free charges [59, 67, 72, 318]. This enables the identification of

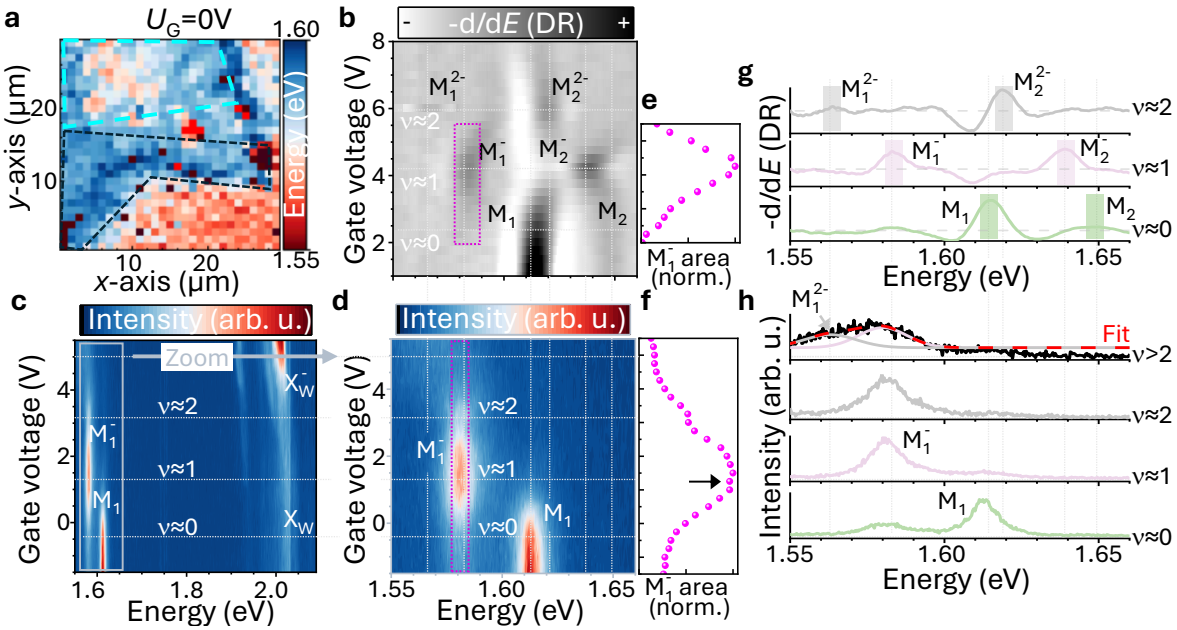

Figure 4.2.6 | a Area scan of the M_1^- PL peak energy of sample R8 recorded at zero gate voltage ($U_G = 0\,\mathrm{V}$), extracted via Gaussian fits to the PL spectra in the displayed energy range. The gated heterostructure region is highlighted in cyan and the $MoSe_2$ ML region in black. A clear redshift in emission energy indicates good interlayer contact. **b** Heatmap of the negative energy derivative of DR spectra ($-\mathrm{d}/\mathrm{d}E(\mathrm{DR})$) versus gate voltage, showing various moiré excitonic complexes and corresponding filling factors ν. **c** Heatmap of PL spectra as a function of gate voltage measured at 4 K at a high-quality location. **d** Zoom-in of gray-framed region of **b**. Normalized area of the pink-highlighted M_1^- **e** $-\mathrm{d}/\mathrm{d}E(\mathrm{DR})$- and **f** PL signal. A small intensity dip in the PL signal at filling factor $\nu \approx 1$ is marked by a black arrow. Selected **g** $-\mathrm{d}/\mathrm{d}E(\mathrm{DR})$ and **h** PL spectra from **b** and **d**, respectively.

a filling factor $\nu \approx 1$ at $U_G \approx 4.25\,\mathrm{V}$, which is shown in Fig. 4.2.6**e**. A distinct local minimum in the PL intensity near 1.5 V (marked with a black arrow in Fig. 4.2.6**f**) is attributed to the formation of a generalized Wigner crystal of electrons, which suppresses the availability of free carriers needed for M_1^- formation [74, 77]. The contradictory spectral response of an RC maximum and a PL minimum in identifying the filling factor is consistent with the literature.

Representative $-\mathrm{d}/\mathrm{d}E(\mathrm{DR})$ and PL spectra from Fig. 4.2.6**c** and **d**, respectively, taken at voltages near integer filling factors, are displayed in Figs. 4.2.6**g** and **h**. The aforementioned moiré quasi-particles in the $-\mathrm{d}/\mathrm{d}E(\mathrm{DR})$ spectra are highlighted by color-coded bars following Fig. 4.2.5. The M_1 and M_1^- PL peaks in the PL spectra at $\nu = 0$ and $\nu = 1$ each exhibit approximately 16% of the intensity of the other, indicating a degree of inhomogeneity—maybe due to inhomogeneous charging—in the sample. No significant change is observed in the PL signal's shape between $\nu = 1$ and $\nu = 2$. At higher electron densities, the emergence of an asymmetric peak—comprising the M_1^- and a shifting M_1^{2-} resonance—alongside the previously mentioned charged WS_2 exciton PL suggests CB hybridization between $MoSe_2$ and WS_2. However, this phenomenon lies beyond the scope of the present thesis and should be addressed in future investigations, where the previously simplified picture—of two mutually repelling, moiré-trapped electrons occupying a single moiré site in the $MoSe_2$ layer—will need to be revised.

A consistent voltage offset of approximately 3 V for $\nu = 1$ is observed between the PL and DR measurements across all samples and multiple measurement runs. This offset cannot be attributed to charging hysteresis, as identical integration times were used for both techniques. Furthermore, a power-dependent study and the use of a long-pass filter during white-light illumination exclude a photo-doping contribution. At low temperatures, only the negatively doped regime—corresponding to positive gate voltages—is reliably accessible. Spot-to-spot variations and differences between cooling cycles can introduce an additional offset of up to 1 V, as systematically discussed in Ref. [319]. Overall, the hetero-BLs remain charge-neutral over a wide voltage range extending down to at least $-10\,\mathrm{V}$, with the single-gate device R10 representing an exception that allows access to the positively doped regime.

Before moving on to the main findings in the next section, the nonresonant Raman response is examined to aid the interpretation of later results and support conclusions about the twist angle. In Fig. 4.2.7**a**, the nonresonant Raman spectrum of the

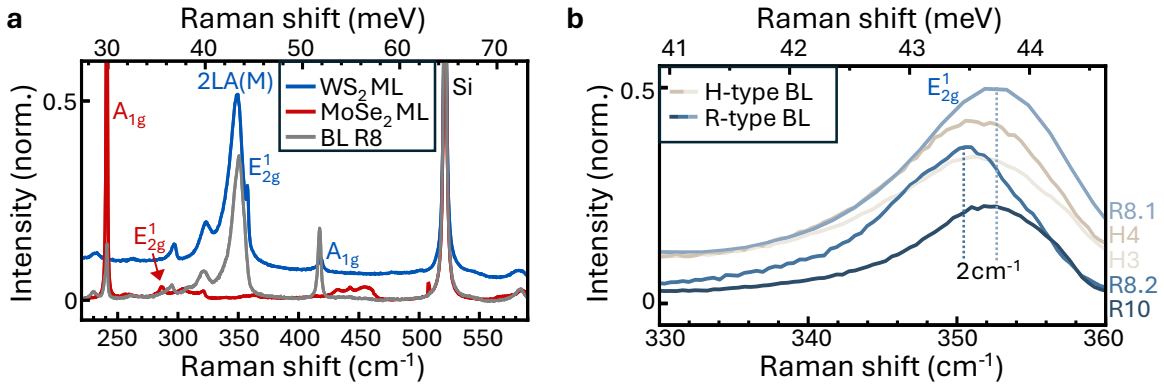

Figure 4.2.7 | Nonresonant Raman spectra at room temperature. **a** Raman spectra of ML and hetero-BL regions of the R-type hetero-BL R8, normalized to the silicon phonon mode at $\approx 521\,\mathrm{cm}^{-1}$. Unlabeled peaks arise from phonon sum and difference processes. **b** Raman spectra in the region of the WS_2 E^1_{2g} mode for two H-type (gray hues) and two R-type (blue hues) hetero-BLs. For sample R8, two spectra from different locations exhibit an energy shift of approximately $2\,\mathrm{cm}^{-1}$.

R8 hetero-BL is shown alongside spectra from adjacent $MoSe_2$ and WS_2 ML regions. All spectra are normalized to the silicon phonon mode. The Raman peaks of the constituent MLs dominate the hetero-BL response, with well-documented modes attributed to sum and difference modes [320, 321].

A closer analysis of the spectral region around the WS_2 E^1_{2g} phonon mode is presented in Fig. 4.2.7**b**, comparing hetero-BLs R8, R10, H3, and H4. The mode appears consistently at $\approx 351\,\mathrm{cm}^{-1}$. For sample R8, spectra from two distinct positions reveal a maximal energy variation of approximately $2\,\mathrm{cm}^{-1}$. In a previous study on twisted WSe_2–WS_2 hetero-BLs [322]—a similar system with a comparable lattice mismatch—the WS_2 E^1_{2g} mode energy is reported to be sensitive to the twist angle, appearing at $\approx 351\,\mathrm{cm}^{-1}$ for 0° twist, with blueshifts of up to $4\,\mathrm{cm}^{-1}$ at 3°. Comparing the measured E^1_{2g} mode positions with these values suggests that all investigated samples are near-angle-aligned, with local twist angles likely $\lessapprox 3°$. Further insights remain speculative, however, due to the lack of reported twist-angle-dependent data close to the H-type alignment in the literature.

These twist-angle-dependent phonon energies, together with the previously discussed stacking-dependent moiré exciton energies and the aligned crystallographic edges during sample fabrication, provide a consistent confirmation of the samples' stacking configuration.

Moreover, the small estimated relative twist angle of $\lessapprox 3°$ in combination with the relative insensitivity of the moiré period to local twist-angle disorder promises a robust moiré lattice constant. This characterization supports the suitability of the hetero-BL for the following investigation of moiré effects.

Phonon-assisted resonant energy transfer: Having confirmed the heterostructures' suitability for further experiments, the focus now shifts to the main findings on exciton dynamics in $MoSe_2$-WS_2 hetero-BLs: phonon-assisted resonant energy transfer (RET) processes. The experimental results from resonant μPL measurements are presented first, followed by their interpretation.

The resonant PL spectra are recorded using a tunable cw Ti:sapphire laser with a power of 800 μW to excite excitonic complexes selectively. For identifying spectral resonances, the dual-gated device R8 is measured at various symmetrically applied voltages to exclude the influence of external electric fields. Fig. 4.2.8**a** displays a heatmap of near-resonantly excited μPL spectra at a gate voltage of $U_\mathrm{G} = -0.5\,\mathrm{V}$. The vertical axis denotes the excitation laser energy, and the horizontal axis the energy shift relative to the laser energy—akin to Raman spectral presentations.

Raman modes appear at constant energy shifts (marked by white arrows) and match those from the nonresonant experiments in Fig. 4.2.7**a**. In contrast, PL emission shifts linearly with excitation energy, which is indicated by the dashed lines tracking the M_1 and M_1^- peaks. The excitonic resonances M_1 ($\approx 1.612\,\mathrm{eV}$), $\mathrm{M}_2/\mathrm{M}_2^-$ (gray-bullet, $\approx 1.64\,\mathrm{eV}$), and M_1^- ($\approx 1.574\,\mathrm{eV}$) can be identified by the RF maxima, which are in agreement with the $-\mathrm{d}/\mathrm{d}E(\mathrm{DR})$ spectra shown in Fig. 4.2.6**c**. The filling factor per moiré cell in the near-resonant PL measurements is determined by evaluating the RF signal (at an arbitrary energy redshift of approximately 3.5 meV) of the excited charge-neutral moiré M_2 exciton and the excited single-charged M_2^- exciton at different gate voltages. Their small energy difference and their resonance linewidth allow an evaluation of the RF signal at one excitation energy, which is indicated as a gray bullet in Fig. 4.2.8**a**, in order to monitor both resonances. The resulting RF signal is shown as a function of the gate voltage in Fig. 4.2.8**c** for the temperatures $T = 5\,\mathrm{K}$ and $T = 60\,\mathrm{K}$ in order to highlight the validity of this approach independent from temperature. The distinct maxima at $U_\mathrm{G} = -0.5\,\mathrm{V}$ for both temperatures from the M_2 RF signal correspond to a filling factor of $\nu \approx 0$. The contribution of the M_2^- RF signal results in a distinct weaker maximum at $U_\mathrm{G} \approx 2.7\,\mathrm{V}$ for $T = 5\,\mathrm{K}$ and

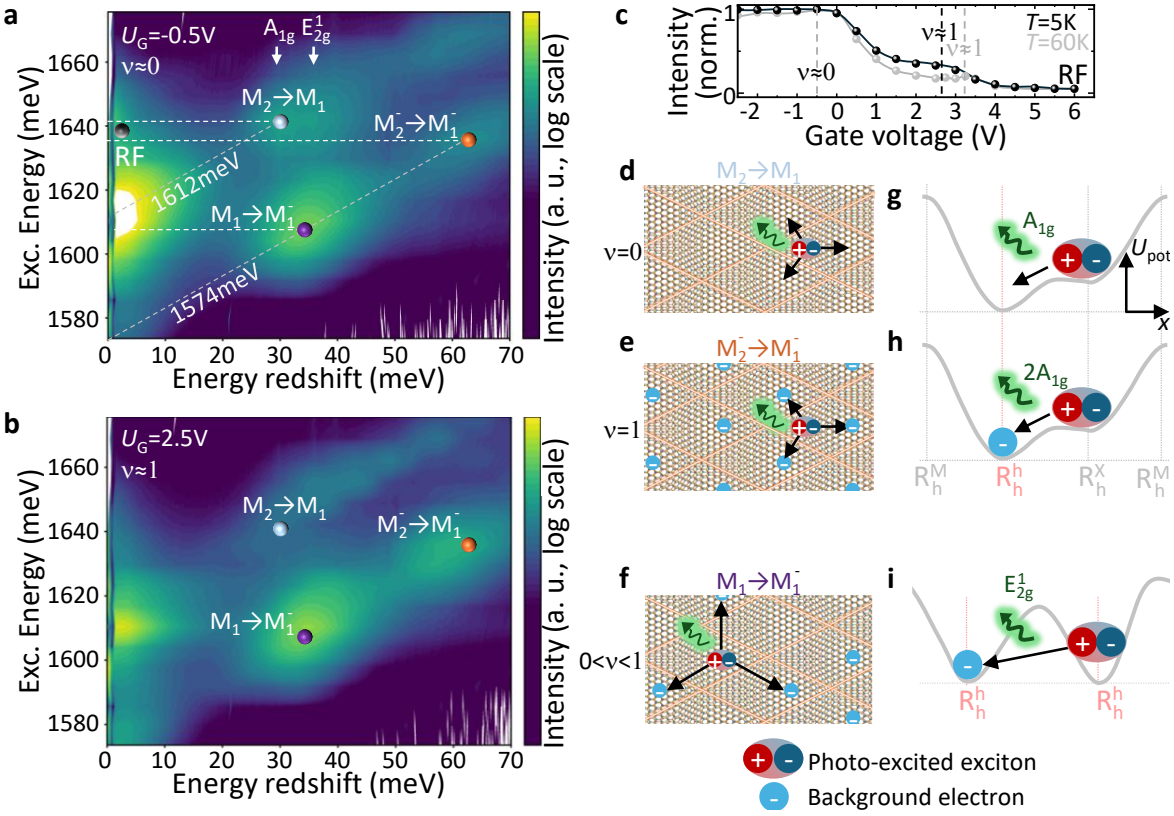

Figure 4.2.8 | a-b Heatmaps (logarithmic scale) of resonantly excited PL spectra versus energy shift relative to the excitation energy for an R-type hetero-BL with symmetrically applied gate voltages: **a** $U_G = -0.5\,V$ ($\nu \approx 0$) and **b** $U_G = 2.5\,V$ ($\nu \approx 1$). Three phonon-assisted RET processes and the M_2/M_2^- RF signal are labeled and marked by colored bullets. The M_1- and M_1^- resonances are indicated by vertical dashed lines. Small vertical arrows denote $MoSe_2$ phonon energies. **c** Normalized M_2/M_2^- RF signal from marked energy in **a** by a gray bullet as a function of the gate voltage for temperatures $T = 5\,K$ and $T = 60\,K$ to determine the filling factor. **d-f** Real-space schematic illustrating phonon-assisted RET processes within a moiré cell and between neighboring moiré cells at different moiré-cell fillings ν. **g-i** Corresponding moiré-potential schematics of the phonon-assisted transfer processes from **d-f**.

$U_G \approx 3.1\,V$ for $T = 60\,K$, correspondingly. The slight voltage shift between the temperatures is attributed to thermal effects. The gate voltage for $\nu = 1$ during near-resonantly measured PL closely matches the values determined from white-light DR measurements, where $\nu = 1$ shows a spot-to-spot variability between $U_G = 3.1\,V$ to $U_G = 4.3\,V$.

Interestingly, when exciting the M_1 resonance, M_1^- is simultaneously observed (purple bullet in Fig. 4.2.8**a**), indicating the presence of single-charged moiré sites—likely due to the reported sample inhomogeneities. The transitions $M_2 \rightarrow M_1$ (light-blue bullet)

and $M_2^- \rightarrow M_1^-$ (orange bullet) require the integer filling factors $\nu = 0$ and $\nu = 1$, respectively. The energy differences between $M_2 \rightarrow M_1$ and $M_1 \rightarrow M_1^-$ transitions match the $MoSe_2$ A_{1g} and E_{2g}^1 phonon energies. The energy offset in the $M_2^- \rightarrow M_1^-$ transition corresponds approximately to twice the A_{1g} phonon energy, suggesting a highly efficient energy down-conversion process as a resonance is achieved by one or two phonons, depending on the energy difference.

Phonon-assisted up-conversion—excitonic anti-Stokes PL—is reported in TMDC MLs [118, 323–327] and in twisted WSe_2 BLs [328]. Theoretical calculations of up/down-conversion rates in TMDC MLs, considering temperature and doping, can be found in Ref. [329]. In the present study, a phonon-assisted down-conversion of excitonic complexes with defined spatial separation is considered and will be introduced in the following.

The three proposed RET mechanisms are illustrated schematically in Figs. 4.2.8**d**–**f** (top-view of real-space representation) and Figs. 4.2.8**g**–**i** (moiré potential landscape in real space). In these schematics, the moiré cell is depicted such that the potential minimum at R_h^h lies at the center. For M_2 and M_2^- to M_1 and M_1^-, respectively, a phonon-assisted energy transfer occurs predominantly within a single cell or between adjacent cells of identical charging state. In contrast, the M_1 state, photo-excited in a charge-neutral cell, undergoes a phonon-mediated transfer to a neighboring charged moiré cell, i.e., requiring an inter-cell RET process. As mentioned above, all the processes become resonant due to the phonon emission. The inverse process—an electron moving to the photo-excited moiré exciton—is deemed unlikely due to Coulomb repulsion [287, 294, 300].

Next, the measurements at a charge filling of $\nu \approx 1$ (corresponding to $U_G = 2.5\,V$ at $T = 5\,K$, Fig. 4.2.8**b**) are considered. Compared to $\nu \approx 0$, the M_1 and M_2 RF signal is noticeably reduced. Consistently, the phonon-assisted transfer process $M_2 \rightarrow M_1$ becomes indistinguishable from the diffuse background. In contrast, the increased prominence of the $M_2^- \rightarrow M_1^-$ and $M_1 \rightarrow M_1^-$ transitions will be more clearly evident in the subsequent analysis of RET intensities as a function of gate voltage.

The transition probabilities are compared by normalizing the spectra to the RF signal. Since the RF intensity is proportional to the oscillator strength of the excitation, this normalization provides a measure of the transfer process probabilities, which depend on the initially photo-excited states. To illustrate measurements not only at integer fillings but also at a filling $0 < \nu < 1$, a normalized PL heatmap at $U_G = 1.0\,V$ is

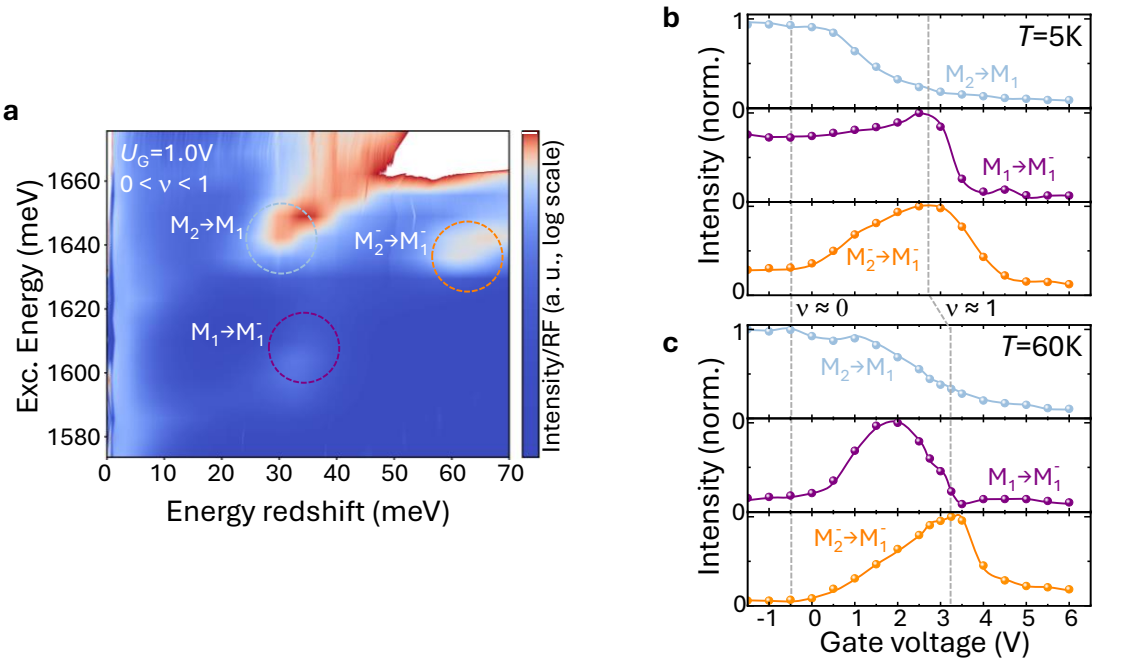

Figure 4.2.9 | a Relative intensity heatmap (logarithmic scale) of resonantly-excited PL spectra at $U_G = 1.0\,V$, normalized to the RF intensities at an arbitrary energy shift of 3.5 meV. **b, c** Normalized PL intensities as a function of gate voltage at the positions indicated by dashed circles in **a** and colored bullets in Figs. 4.2.8**a, b**, measured at **b** $T = 5\,K$ and **c** $T = 60\,K$.

shown in Fig. 4.2.9**a**. Here, the intra-cell processes $M_2 \rightarrow M_1$ and $M_2^- \rightarrow M_1^-$ are more efficient than the inter-cell $M_1 \rightarrow M_1^-$ transition consistent with the proposed RET mechanism, where larger spatial separations and increased potential walls reduce transfer probability. This holds despite the $M_1 \rightarrow M_1^-$ process being expected to have its maximum at $\nu = 1/2$ when a charged moiré cell neighbors an uncharged one, as highlighted in the following.

The three RET processes are now analyzed as a function of gate voltage. The normalized RET transfer rates measured at temperatures of 5 K and 60 K are shown in Figs. 4.2.9**b** and **c**, respectively, where the previously determined charge-filling factors are marked. At 5 K, the $M_2 \rightarrow M_1$ transfer reaches its maximum near $\nu \approx 0$, as expected. Meanwhile, the $M_2^- \rightarrow M_1^-$ process increases and peaks around $\nu \approx 1$.

The inter-cell transfer $M_1 \rightarrow M_1^-$ shows a finite strength near charge neutrality, likely due to sample inhomogeneities that prevent perfect neutrality. Its intensity rises at positive voltages, peaking at $\nu \approx 1$, which is surprising, since one would expect a maximum around $\nu \approx 1/2$ for a RET between unoccupied and neighboring occupied sites. At the higher temperature of 60 K (Fig. 4.2.9**c**), the curves, including that of the

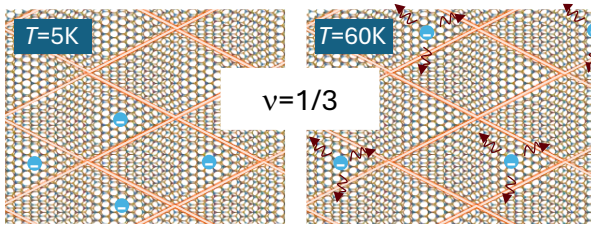

Figure 4.2.10 | Schematic illustration of moiré-lattice charging at $\nu = 1/3$ for temperatures 5 K and 60 K. The thermal energy alongside Coulomb repulsion between the charges, indicated by arrows, result in homogeneous charging of the moiré lattice.

$M_1 \rightarrow M_1^-$ process, follow the expected behavior with a slight shift toward higher gate voltages. This shift suggests that thermal energy in combination with the Coulomb repulsion of electrons overcome local potential variations and allow for a redistribution of charges. This results in a homogeneous charging of the moiré lattice and, thus, in a maximum of unoccupied moiré minima adjacent to occupied ones. The charging of a moiré lattice at $\nu = 1/3$ is schematically illustrated in Fig. 4.2.10 for $T = 5\,\mathrm{K}$ and $T = 60\,\mathrm{K}$. Arrows hereby indicate the homogeneous charging at elevated temperatures due to thermal energy and Coulomb repulsion.

Before discussing the origin of the RET processes, their reproducibility across multiple samples—not just different measurement spots—is demonstrated. Near-resonant PL measurements on the single-gate R-type devices R6, R9, and R10 are shown as heatmaps of the PL spectra versus energy redshift in Figs. 4.2.11**a-c**. For these gated devices, heatmaps corresponding to charge fillings of $0 < \nu < 1$ are presented. In all three R-type samples, the three RET processes $M_2 \rightarrow M_1$, $M_2^- \rightarrow M_1^-$, and $M_1 \rightarrow M_1^-$ can be unambiguously identified, except for the $M_2^- \rightarrow M_1^-$ process, which is comparably weak in sample R6. The gate-voltage dependence of the $M_1 \rightarrow M_1^-$ process is shown in Figs. 4.2.11**d-f**, alongside the M_2/M_2^- RF signal for the samples R6 and R9 and the M_1 RF signal for R10, which is used to identify the charge-neutral state. The sample R9, like R8, can only be negatively doped, and R9 approaches charge neutrality more closely than R8. The strong decrease in the M_2 and M_1 RF signal at negative voltages in samples R6 and R10, respectively, alongside a rise in the $M_1 \rightarrow M_1^-$ intensity suggests positive doping, potentially due to direct contact between the ground and the $MoSe_2$ ML in these samples—a characteristic absent in R8 and R9. Nevertheless, in all three samples, the $M_1 \rightarrow M_1^-$ process, which will be crucial for the following discussion, shows a minimum at $\nu = 0$ and increases with negative doping. In these

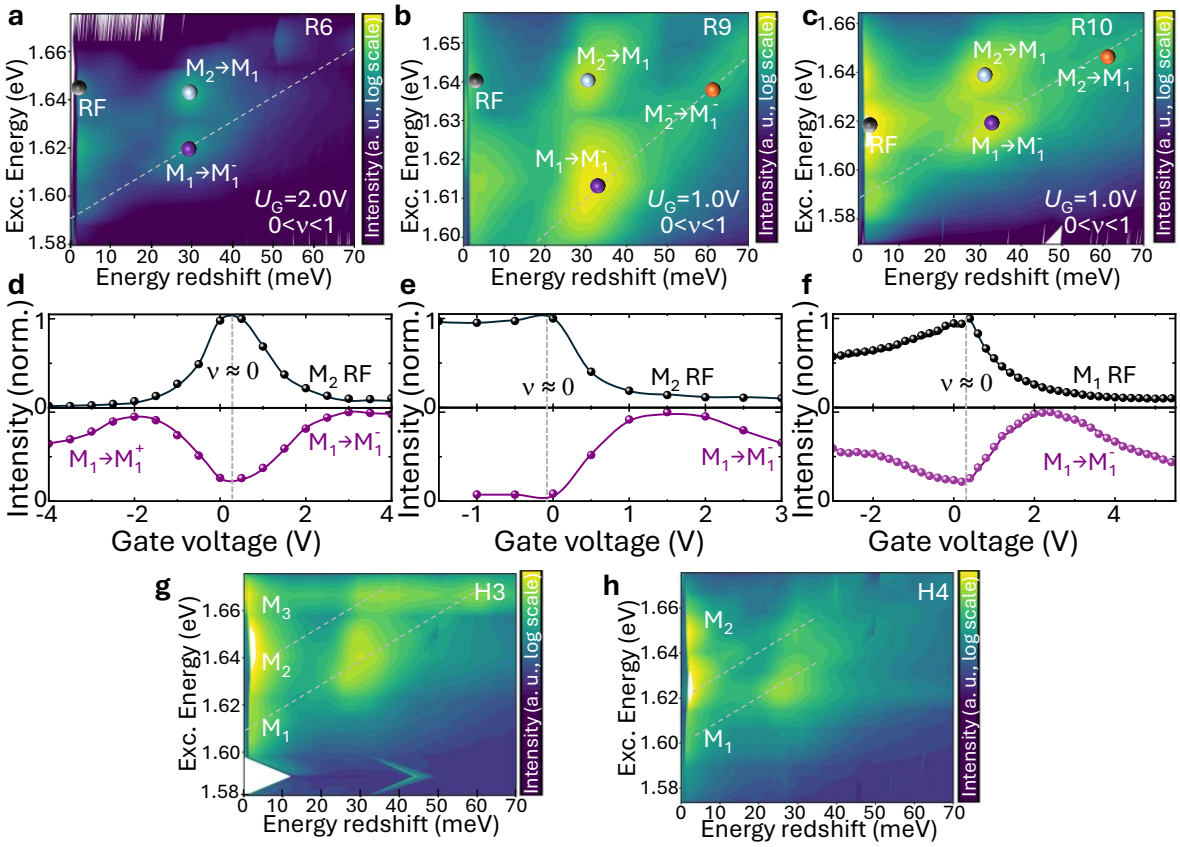

Figure 4.2.11 | Heatmaps (logarithmic scale) of resonantly-excited PL spectra versus energy shift relative to the excitation energy for single-gate R-type hetero-BLs: **a** R6, **b** R9, and **c** R10, at gate voltages corresponding to $0 < \nu < 1$. The RET processes $M_2 \rightarrow M_1$, $M_2^- \rightarrow M_1^-$, and $M_1 \rightarrow M_1^-$, as well as the M_2/M_1 RF signal, are marked by colored bullets. **d-f** Normalized PL intensities versus gate voltage for the M_2 RF signal and the $M_1 \rightarrow M_1^-$ process, shown with matching colors for the three R-type samples from **a-c**. The M_1 RF signal is used to identify $\nu \approx 0$. Heatmaps (logarithmic scale) of resonantly-excited PL spectra versus energy redshift of the H-type hetero-BL samples **g** H3 and **h** H4.

single-gate devices, the accompanying out-of-plane electric field complicates analysis beyond phenomenological confirmation and is, therefore, not further discussed.

Equivalent near-resonant measurements are performed on the H-type samples H3 and H4, shown in Figs. 4.2.11**g** and **h**. For each sample, three RF maxima are observed alongside RET processes. Comparing these results with the negative first derivative of RC measurements from Ref. [61, 313] in Fig. 4.2.4**b** suggests the presence of three charge-neutral moiré absorption peaks. This allows a tentative assignment of the three observed RF maxima in sample H3 to the moiré excitons M_1, M_2, and M_3, with energies in good agreement with the literature. To more clearly identify the RF peaks in sample

H4 and to explore possible RET processes in general, gated devices enabling doping-dependent near-resonant PL measurements are required, but beyond the scope of this thesis.

Discussion: Two mechanisms are likely to be the origin of the observed RET processes: phonon-assisted resonant tunneling and/or phonon-assisted Förster resonance energy transfer (FRET), a non-radiative dipole-dipole energy transfer. It is important to emphasize again that the energetic resonance condition between the initial and final states in all three processes is fulfilled by the emission of one optical phonon (A_{1g} for $M_2 \rightarrow M_1$ and E^1_{2g} for $M_1 \rightarrow M_1^-$) or two optical phonons ($2 \times A_{1g}$ for $M_2^- \rightarrow M_1^-$) during the transfers between moiré sites or cells.

The general down-conversion process from a neutral exciton to a charged exciton has been theoretically analyzed for TMDC MLs in Ref. [329]. There, Fermi's golden rule is applied within the effective-mass approximation to investigate population transfer. The electron–phonon interaction is incorporated via the Fröhlich interaction for the in-plane E^1_{2g} phonon mode and the deformation potential for the out-of-plane A_{1g} mode. This analysis concludes that the transfer becomes unlikely at elevated temperatures and low background doping, as the conversion time exceeds the exciton's radiative lifetime—consistent with experimental observations reported in Ref. [330]. This decrease in the down-conversion rate is, thereby, primarily attributed to free electrons acquiring larger wave vectors at higher temperatures. However, the relevance of these results to moiré-trapped electrons and excitons remains under debate, since the theoretical framework assumes, for example, a background doping described as a free-electron gas rather than as localized electrons.

The spatial separation d between moiré sites involved in the observed processes exceeds the characteristic range of Dexter-type energy transfer, which is limited to a few nanometers by the required wavefunction overlap. Therefore, a Dexter mechanism can be excluded [331–333]. This leaves the previously mentioned two viable candidates for the observed energy transfer: exciton tunneling between moiré potential minima and non-radiative dipole–dipole coupling, i.e., the FRET mechanism [334–336]. Tunneling exhibits an exponential decay with distance, whereas FRET scales with $1/d^4$ in a 2D system [337]. The FRET process has been theoretically predicted [317, 338, 339] and experimentally confirmed in various TMDC-based systems [221, 260, 333, 340–345], including heterostructures. For lateral FRET processes within a single layer, dielec-

tric screening further reduces the effective transfer distance. Notably, the condition of aligned optical dipole moments is fulfilled [336]. To distinguish between tunneling and FRET via a detailed analysis of the spatial dependence on d, one would need to conduct a hetero-BL study across samples with varying twist angles—similar to the approach in Ref. [56]—which is, however, beyond the scope of this thesis.

A more in-depth analysis of the $M_1 \rightarrow M_1^-$ process can only be performed by examining its temperature dependence. This RET process is chosen because it is the lowest-energy transition and because the maximal spatial distance between moiré sites is bridged. It is therefore most sensitive to environmental changes as competing RET processes are absent. One straightforward approach is to vary the sample temperature and monitor the M_1^- intensities as a function of the symmetrically applied gate voltage, when exciting in M_1 resonance. This is shown for four different temperatures in Fig. 4.2.12**b**. To reduce statistical uncertainty, each data point represents the average of measurements taken at five different sample spots.

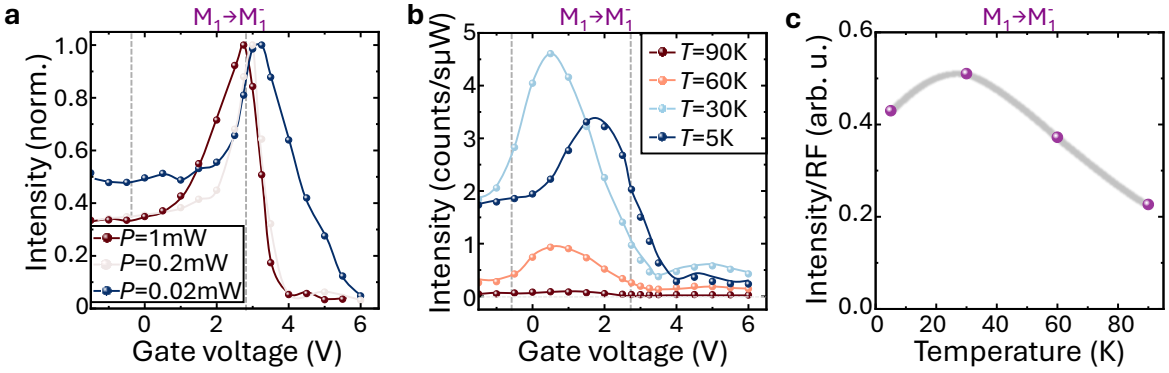

Figure 4.2.12 | Intensity of the $M_1 \rightarrow M_1^-$ RET process as a function of the gate voltage: **a** normalized power-dependent measurements and **b** temperature series. All data of the latter are averaged over measurements conducted on five different sample spots. **c** Maximum $M_1 \rightarrow M_1^-$ intensity at each temperature from panel **b**, normalized to the corresponding RF signal. The drawn-through lines serve as guides to the eye.

As discussed earlier, thermal energy in combination with Coulomb repulsion results in a more homogeneous electron distribution of the moiré lattice. This should maximize the number of unoccupied sites adjacent to occupied ones, thereby enhancing the energy transfer rate and increasing the M_1^- intensity. Furthermore, thermal activation may help equilibrate local energy variations across moiré sites, potentially promoting the tunneling rate.

Scattering with thermal phonons also broadens the exciton distribution in momentum space, which has been predicted to enhance the Förster transfer rate [339]. It

is also noteworthy that the acoustic moiré phonon modes of $MoSe_2$ have energies of approximately 2 meV and 3 meV for a moiré period of $d \approx 7.5$ nm (see Ref. [346] and the following Section 4.2.3). These phonons become thermally activated at $T \gtrsim 30$ K, which may further support energy transfer between moiré cells via higher-order processes.

Alternatively, thermal activation can be induced by increasing the excitation power. However, this approach introduces a competing effect—the saturation of excitonic states—which limits the analysis to a complementary role. The M_1^- intensity as a function of gate voltage, under resonant excitation at M_1, is shown normalized for three different excitation powers in Fig. 4.2.12**a**. An increase in excitation power results in a shift of the M_1^- maximum toward lower gate voltages. This behavior is consistent with the thermal-activation mechanism discussed for the elevated-temperature case, while a possible contribution from saturation effects cannot be ruled out. The gate voltage corresponding to the integer charge filling per moiré site $\nu = 1$ varies slightly between the temperature- and power-dependent measurements, as they were conducted during different cooling cycles.

A more detailed analysis of the temperature dependence can be performed by using that the M_1^- intensity is proportional to the population of the initial M_1 states. As before, this allows normalization of the intensities to the RF signal, as already shown in Fig. 4.2.9**a**. The resulting relative intensities at the M_1^- maxima are extracted for each temperature and plotted in Fig. 4.2.12**c** as a function of temperature. The transfer probability increases up to 30 K, which is attributed to an increasingly homogeneous charge distribution in the moiré superlattice. At higher temperatures, however, the $M_1 \rightarrow M_1^-$ RET process exhibits an apparent decline in transfer probability. In contrast, the relative intensities show, as expected, no significant variation with excitation power.

Recent theoretical predictions on trapped moiré excitons suggest that the FRET mechanism follows a power-law increase with temperature [317], as the dipole-dipole coupling strengthens similarly to the free-exciton case discussed earlier [339]. This effect might contribute to the observed rise in transfer rate at low temperatures. Experimental studies involving TMDCs, however, report varied behaviors. Some find the energy transfer rate to remain constant up to 300 K [340, 347], while others observe an increase [342, 345]. A decrease in FRET rate with increasing temperature was only reported in Ref. [344], where enhanced exciton-phonon scattering [348] accelerates ex-

citon thermalization, thereby hindering energy transfer of excited excitonic complexes. This mechanism is not considered relevant for the already thermalized trapped moiré excitons during the experiments presented in this thesis. Therefore, a potential FRET process being the predominant RET process can be tentatively excluded.

The following paragraph focuses on quantum tunneling in moiré heterobilayers and its temperature dependence. The increase in exciton-phonon scattering with rising temperature is predicted to be crucial in moiré superlattices [317, 349] as the resulting reduction in energy transfer efficiency may be explained in the polaron picture, where polaron–acoustic-phonon interactions renormalize moiré-exciton energies, leading to a decrease in energy tunneling rates as temperature increases [350]. The influence of charges within the moiré superlattice on energy-transfer rates remains unclear, as the existing literature [317, 349, 350] primarily addresses neutral excitons. With these supporting theoretical calculations on energy transport in moiré lattices and after eliminating the FRET as the primary RET process, the observed phonon-assisted RET processes can be tentatively attributed to phonon-assisted resonant tunneling.

This study on excitonic complexes in moiré superlattices and the observed phonon-assisted RET processes is published in Ref. [315] and the corresponding Supplementary Information [319]. It marks a key step toward understanding the fundamental dynamics in artificially stacked BLs and toward engineering tailored excitonic landscapes. In particular, the observation of lateral phonon-assisted RET processes in $MoSe_2$–WS_2 hetero-BLs provides a foundation for future theoretical studies on the lateral diffusion of trapped moiré excitonic complexes and the influence of resident carriers.

4.2.2 Outlook: The Hunt for generalized Wigner phonons

In the following, a more in-depth discussion of the previously introduced generalized Wigner crystal and the associated physical phenomena is provided, offering a novel avenue of research into Raman spectroscopy in correlated systems.

To understand the emergence of correlated electronic phases in moiré materials, it is imperative to first introduce the concept of an electron lattice. In low charge carriers densities, Coulomb repulsion dominates over kinetic energy, resulting in the formation of an ordered charge lattice—a Wigner crystal [351–353]. In an ideal two-dimensional system, the electrons or holes arrange in a triangular lattice with a single-charge basis.

The collective vibrations of this crystal can be described by two acoustic phonon modes, transverse acoustic (TA) and longitudinal acoustic (LA) [354, 355].

When a periodic potential such as the moiré potential in $MoSe_2$–WS_2 hetero-BLs is present, charge carriers may become trapped at moiré sites. In this case, a generalized Wigner crystal is formed, governed by the interplay between Coulomb repulsion and moiré pinning [62, 64, 68]. As an example, the resulting TA phonon of such a generalized Wigner crystal is shown in Figs. 4.2.13**a** and **b** for hole filling factors $\nu = 1$ and $\nu = 1/3$, respectively. In this case, the harmonic confinement potential introduces a finite zero-point energy [64, 296, 356, 357]. As a consequence, the crystallized phase can remain stable up to elevated temperatures and can be investigated in resonant optical experiments [71, 299].

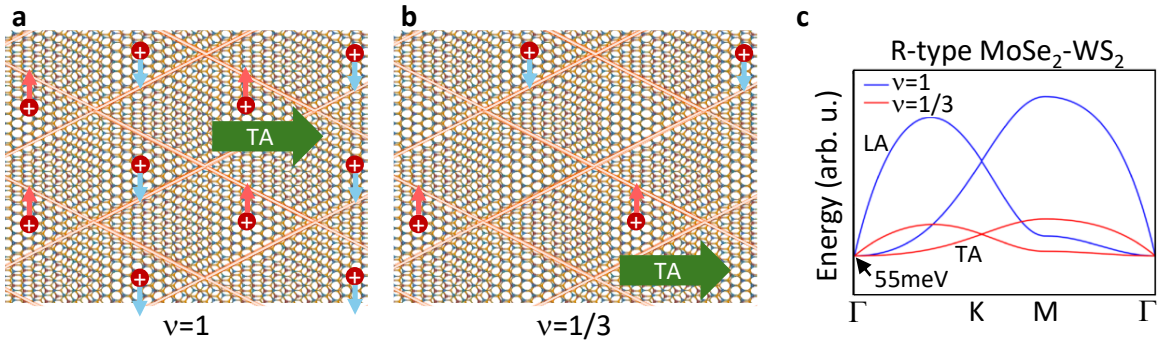

Figure 4.2.13 | TA generalized Wigner-crystal phonon at hole fillings **a** $\nu = 1$ and **b** $\nu = 1/3$. **c** Calculated LA (upper branch) and TA (lower branch) Wigner-phonon dispersions (for hole fillings $\nu = 1$ and $\nu = 1/3$) of R-type $MoSe_2$-WS_2 hetero-BLs with a calculated zero-point energy of ≈ 55 meV[358].

Additionally, the Wigner phonon dispersion is dependent on the charge filling factor as the Coulomb interaction between the electrons is influenced by the crystal lattice constant [64, 356, 357]. The calculated dispersions for fractional $\nu = 1/3$ and integer $\nu = 1$ hole fillings are shown in Fig. 4.2.13**c**, displaying the Wigner-phonon dispersions in R-type $MoSe_2$–WS_2 hetero-BLs, calculated by Dr. D. Erkensten [358]. Importantly, the high-symmetry points in reciprocal space correspond to the generalized Wigner crystal rather than the moiré superlattice. Since the generalized Wigner crystal at $\nu = 1/3$ is three times larger in real space than the moiré superlattice, its corresponding BZ is 1/3 the size. The zero-point energy of this hole crystal is approximately 55 meV.

Furthermore, the moiré potential can induce backfolding of the generalized Wigner-phonon branches to the BZ center, rendering them Raman-active. These moiré-induced

Raman-active modes are referred to as moiré-Wigner phonons. A more detailed introduction will be provided in the following section. As the moiré lattice period is equivalent to the Wigner-crystal size at $\nu = 1$, this results in the Raman activation of the Wigner phonons at the K points. In this case, the LA and TA Wigner phonons are energetically degenerate with a calculated energy of ≈ 61 meV for a generalized hole crystal. For equivalent generalized moiré-Wigner phonons at $\nu = 1/3$, further theoretical calculations are needed. Altogether, this theoretical framework provides an initial basis for experimental investigations.

First resonant Raman experiments on the R-type $MoSe_2$–WS_2 hetero-BL R10, introduced in the previous section, are conducted in collaboration with M. Lorenz. To remain non-invasive and below the melting temperature, the excitation power is reduced to the tens-of-μW range. Additionally, the reduction of the PL background and IMBEs (c.f. 4.2.1 and Ref. [289]) is achieved by tuning into extreme resonance with the M_1^- exciton at ≈ 1.58 meV. Spot-to-spot variations and differences between successive cooling cycles result again in charge-filling variations of approximately 1 V. For this reason, the RF signal is considered a reliable indicator of the charge-filling factor, as this information is gained from the same Raman spectra.

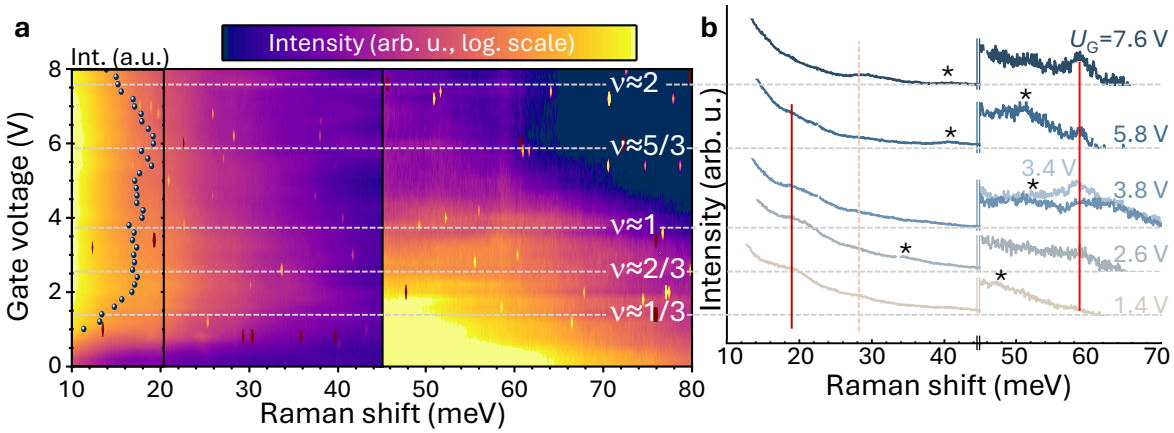

Figure 4.2.14 | a Heatmap (logarithmic scale) of Raman spectra versus Raman shift relative to the applied gate voltage in the electron-doped regime excited at M_1^-. The intensities are rescaled for shifts from 45 meV. The inset displays the averaged RF intensities in the interval 10-13 meV, which are used to estimate the electron-filling factors ν, indicated by dashed lines as guides to the eye. **b** Selected Raman spectra at the marked moiré-site fillings from **a**, including one at $U_G = 3.4$ V. The spectra are individually rescaled starting from 45 meV upward. The solid red lines indicate potential IMBEs, and the orange-dashed line marks the potential zero-point energy Wigner-phonon. Peaks appearing exclusively at the identified filling factors are highlighted with asterisks.

In the first resonant Raman experiments, the hole-doped and electron-doped regimes are investigated simultaneously. The results for the electron-doped regime are displayed in Fig. 4.2.14**a** as a heatmap, where the intensities are shown on a logarithmic scale and rescaled for Raman shifts above 45 meV. The RF signal intensities, extracted by averaging over the energy range 10-13 meV, are displayed in the inset of the heatmap and used to estimate the electron filling factors. While in experiments of the previous section only broad RF signal maxima are visible due to elevated excitation powers and large voltage steps, in the present measurements clear local minima of the RF signal are observed at gate voltages of approximately 1.4 V, 2.6 V, 3.8 V, 5.9 V, and 7.6 V. Due to their equidistant separation and the emergence of additional peaks, these signatures are tentatively assigned to moiré-site filling factors of $\nu \approx 1/3$, 2/3, 1, 5/3, and 2, respectively. Here, the duality of the absorption maximum [59, 67, 72, 318] and the PL minimum [74, 77] at Wigner-crystallized states leaves the interpretation of the RF signal open to debate.

Selected spectra corresponding to these voltages, together with an additional spectrum at $U_G = 3.4$ V, is shown in Fig. 4.2.14**b**. The intensities are individually rescaled starting from 45 meV. A distinct peak at ≈ 19 meV, highlighted by a dark-red line, is consistently observed in all spectra but weakened as $\nu \approx 2$ is approached. This signature is likely related to an IMBE between moiré CBs. Similar collective excitations are reported in hole-doped twisted WSe_2 homo-BLs in Ref. [289]. The lower energy of ≈ 19 meV, in contrast to the ≈ 50 meV reported for hole IMBEs, can be explained by the small CB splitting and therefore moiré-CB splitting, when compared to the large VB splitting. Consistent with this interpretation, the peak vanishes when the filling exceeds $\nu \approx 2$, which can be attributed to the Pauli blocking of the IMBE between the lowest CB and first moiré CB. Although confirmation will require further tests, such as resonance determination, an assignment to a Wigner phonon can be excluded due to the signal's weak dependence on the filling factor. Additional faint peaks around 60 meV, marked by bright-red lines in Fig. 4.2.14**b**, may arise from related higher-order IMBEs.

The lowest-energy Wigner-phonon mode is expected at the zero-point energy and should be observable only for all integer and fractional moiré-site fillings. A candidate peak is indicated by the orange-dashed line at ≈ 28 meV. The expected energy may be smaller than the calculated hole Wigner-phonon energy of ≈ 55 meV due to the smaller electron mass [358]. The dependence of its intensity on gate voltage could

be reliably analyzed only near $\nu \approx 2$. The intensity is found to be highest close to the identified integer filling. Some overlap with the $MoSe_2$ A_{1g} phonon cannot be ruled out. Furthermore, the moiré–Wigner phonons are expected at higher energies. For a possible peak assignment in the experimental spectra, phonon dispersion calculations for generalized electron crystals are needed.

Additional unidentified peaks appear solely at the assigned integer or fractional fillings. Such signals are marked by asterisks in Fig. 4.2.14**b**. Their origin has to be investigated in further studies.

At this stage, the assignment of the observed peaks to moiré–Wigner phonons is not possible, especially without supporting theoretical calculations. For an unambiguous peak identification, homogeneous, high-quality samples with reduced RF signal linewidth are required.

In contrast to this, the hole-doping regime is predicted to yield more stable Wigner crystals due to the higher hole effective mass and the resulting larger zero-point energy. In the first doping-dependent investigations, excitation energies at M_1^+ ($\approx 1.59\,\mathrm{meV}$) and below the M_1^+ ($\approx 1.58\,\mathrm{meV}$) resonances are employed. The key findings are similar for both cases. For a direct comparison with the electron-doped regime, the spectra presented as a heatmap in Fig. 4.2.15**a** are from the earlier presented measurement run with an excitation at $E_{\mathrm{exc}} = E_{\mathrm{M}_1^-}$. The RF signal, again extracted by averaging over the energy range 10-13 meV, is shown in the inset. Small modulations are observed, with local minima again interpreted as signatures of Wigner crystallization. Horizontal lines as guides to the eye are drawn at the same voltages as in the electron-doped case, consistent with the expected symmetry, except for a rigid intrinsic offset arising from the background doping. Agreement of the filling factors with the electron-doping regime is observed as some minor local minima appear. A similar accordance can be found in a second dataset, obtained at $E_{\mathrm{exc}} = E_{\mathrm{M}_1^+}$.

All further observable peaks are broad and extend over a wide doping regime, suggesting an IMBE origin as discussed in Ref. [289]. This is unexpected since the excitation energy is below the M_1^+ resonance. Nevertheless, the intensities of the most prominent peaks at $\approx$ 35 meV, 48 meV, and 56 meV—the latter with a similar energy to the electron-doping regime—plotted as a function of gate voltage in Fig. 4.2.15**b**, display clear oscillations and both minima and maxima at the estimated hole fillings ν. The only apparent exception is the 48 meV peak at $\nu \approx 1/3$, which is close to the zero-point energy of generalized hole Wigner crystals predicted by Dr. D. Erkensten [358].

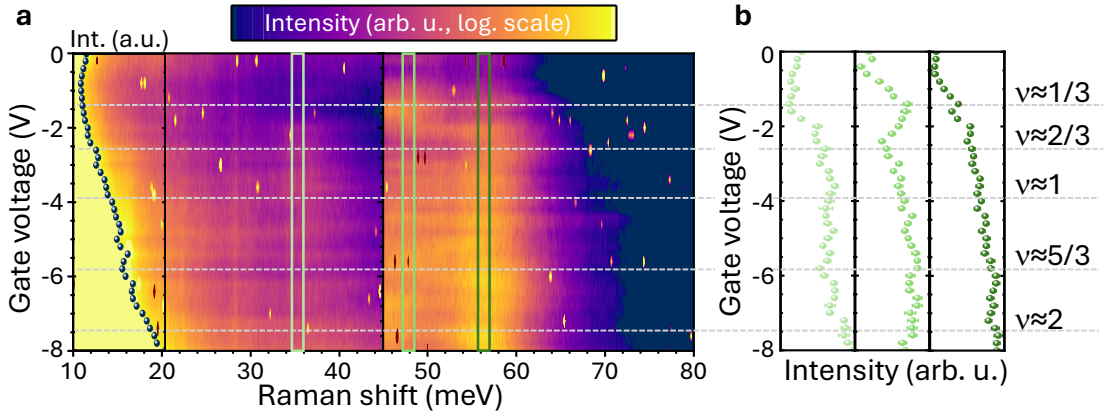

Figure 4.2.15 | a Heatmap (logarithmic scale) of Raman spectra versus Raman shift relative to the applied gate voltage in the hole-doped regime excited at M_1^-. The intensities are rescaled starting from 45 meV. The inset shows the RF intensities averaged in the interval 10-13 meV. The estimated hole-filling factors ν are taken from the negative doping case in Fig. 4.2.14**a** and are marked by dashed lines as guides to the eye. Prominent peaks are marked by green boxes. **b** Integrated intensities of the green-colored boxes from **a**.

This local maximum may therefore represent the first experimental indication of a generalized Wigner phonon.

Additional unidentified peaks appear at $\approx$ 18 meV, 26 meV, and 70 meV. For a more conclusive interpretation of these feature-rich moiré heterostructures, distinguishing between IMBEs and moiré-Wigner phonon modes is required. This can be achieved through measurements on high-quality samples combined with a systematic investigation of the resonance behavior of the individual excitations.

Once this fundamental groundwork is established, the inversion asymmetry at $\nu = 2$ arising from the two inequivalent moiré minima or the time-reversal asymmetry due to the application of a finite magnetic field in these hetero-BLs is predicted to give rise to chiral phonons of the electron lattice [356, 357]—lattice vibrations that carry a well-defined angular momentum, corresponding to circular atomic motion with a distinct chirality. These chiral phonons couple to electronic and excitonic complexes and can be probed through helicity-resolved Raman/PL spectroscopy [359–362].

4.2.3 Vibrational properties in moiré superlattices

Besides the profound impact on electronic and excitonic behavior, the presence of a moiré superlattice also significantly modifies the vibrational properties of vdW BLs, similar to the influence on electronic lattices as mentioned in the previous section.

A significant effect of the moiré supercell is its influence on the phonon modes of the constituent TMDC MLs. Analogous to the electronic band structure, the phonon dispersion is modified by the emergence of a moiré mini-BZ. As a result, phonon branches experience Bragg reflection at the mini-BZ edges and are backfolded to the Γ point. This backfolding is illustrated in Fig. 4.2.16**a** for the TA and LA $MoSe_2$ ML phonon branches.

The analysis of twisted homo-BLs, like in Refs. [210, 211, 346] is a convenient starting point. Without a lattice constant mismatch, the general expression for the moiré period from Eq. 4.2.1 simplifies to

$$a_m = \frac{a}{2\sin(\theta/2)}, \tag{4.2.3}$$

where a is the lattice constant of the MLs and θ is the twist angle. The corresponding reciprocal moiré lattice constant becomes

$$g = 2b\sin(\theta/2), \tag{4.2.4}$$

with $b = \frac{4\pi}{\sqrt{3}a}$ being the magnitude of the reciprocal lattice vector of the ML.

The following considerations are made analogously to Ref. [346]. The phonon dispersion along the moiré reciprocal lattice vector $\boldsymbol{g}$ is estimated for twist angles in the range $0° \leq \theta \leq 30°$. Therefore, a weighted interpolation between the acoustic phonon branches along the high-symmetry directions Γ–K and Γ–M can be employed. Note that dispersions for $30° < \theta \leq 60°$ are equivalent by symmetry in a hexagonal lattice. This interpolation path is illustrated as a red dashed arc in Fig. 4.2.16**b**, which shows the first and neighboring BZ of a ML together with a second reciprocal lattice vector of a twisted second layer, comprising a twisted BL system.

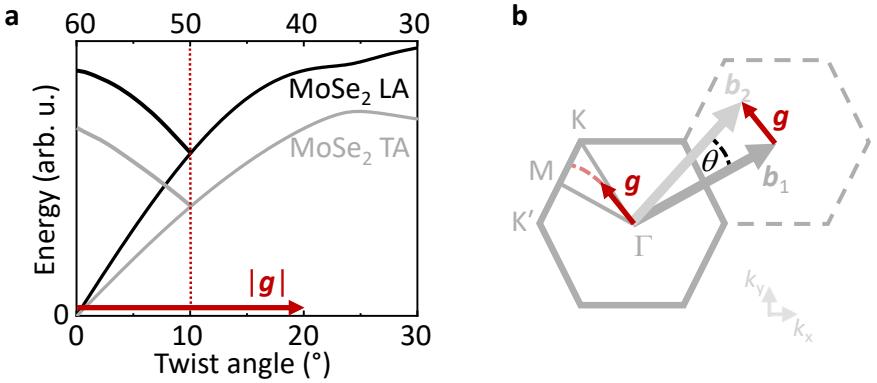

Figure 4.2.16 | Backfolding of phonon branches at the moiré-BZ edge. **a** Calculated twist-angle dependent LA and TA phonon branches of $MoSe_2$ along $\boldsymbol{g}$, backfolded to the Γ point at $|\boldsymbol{g}|/2$. The phonon dispersion is plotted as a function of twist angle θ, using Eq. 4.2.4. **b** First- and neighboring BZ of one ML. The reciprocal lattice vectors $\boldsymbol{b}_1$ and $\boldsymbol{b}_2$ correspond to the two constituent layers, twisted by an angle θ. The resulting reciprocal moiré lattice vector $\boldsymbol{g}$ is shown in red and projected onto the first BZ. The red dashed arc illustrates the evolution of $\boldsymbol{g}$ with twist angle θ.

It is important to note, however, that this estimate does not account for moiré-induced phonon renormalization effects arising from interlayer coupling and lattice reconstruction, which can significantly modify the actual backfolded phonon modes [363, 364].

The resulting phonon branches along the moiré reciprocal lattice vector $\boldsymbol{g}$ are backfolded to the Γ-point at the moiré-BZ edge, located at $|\boldsymbol{g}|/2$. As a result, these modes become Raman-active due to the satisfied momentum conservation during the scattering event. The backfolded dispersion depends on the magnitude of the moiré reciprocal lattice vector $|\boldsymbol{g}|$ and, therefore, on the twist angle θ between the constituent layers, as follows from Eq. 4.2.4. This is illustrated in Fig. 4.2.16**a**.

Non-invasive relative twist-angle determination via moiré phonons

The next logical step is to extend the knowledge of moiré-phonon modes from the reported homo-BL cases [210, 211, 346] to hetero-BLs, where precise control of the twist angle between adjacent layers is inherently limited. Even in twisted homo-BLs fabricated using the widely adopted "tear-and-stack" technique [192], significantly large-scale twist-angle inhomogeneities are reported [211]. This casts doubt on the reliability of estimating the local twist angle in hetero-BLs via second-harmonic generation (SHG) performed on adjacent MLs, as crystallographic alignment may not accurately reflect the twist in the stacked area.

However, accurate knowledge of the local twist angle is essential for reproducibility and meaningful interpretation of twist-sensitive phenomena—such as the earlier-reported moiré exciton dynamics. In this context, Raman spectroscopy can be used as a fast and non-invasive tool. It offers spatially resolved access to local vibrational properties and is compatible with the essential hBN encapsulation. It enables robust characterization of twist angle without compromising sample integrity.

The following experimental results on hetero-BLs are gained by investigating $MoSe_2$-WSe_2 hetero-BLs, where the relative lattice mismatch is only 0.004. The backfolded moiré phonon energies are estimated based on the known ML phonon dispersions of $MoSe_2$ and WSe_2 and the moiré lattice constant. The $MoSe_2$-WSe_2 system is an ideal platform for investigating moiré phonons and, by extension, for extracting information about the local relative twist angle. These experimental results, presented in Fig. 4.2.17 and Fig. 4.2.18, were revisited and further analyzed at the beginning of my PhD thesis, expanding upon work originally carried out during my Master's thesis in collaboration with Dr. J. Holler [346, 365].

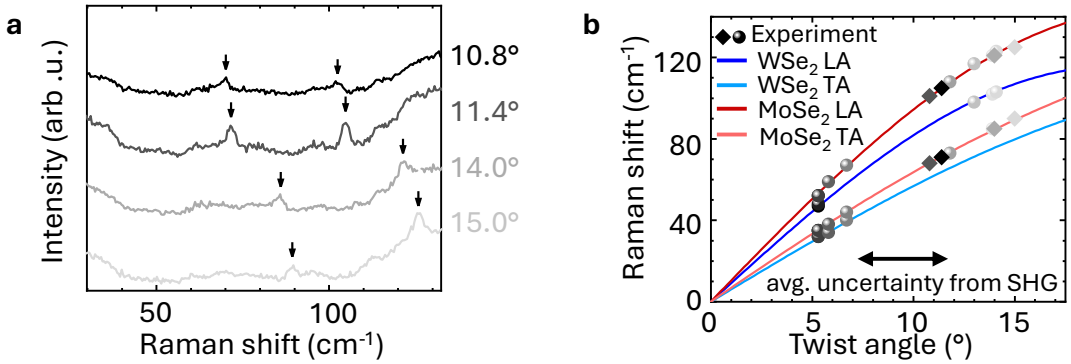

Figure 4.2.17 | a Unpolarized LF Raman spectra of four hetero-BL samples with twist angles determined from moiré-phonon mode energy compared to calculated phonon dispersions. Moiré-phonon modes are marked by arrows. **b** Comparison of experimental moiré-phonon mode energies (diamonds from spectra in **a**, orbs from additional samples) to calculated LA and TA phonon dispersions of $MoSe_2$ and WSe_2 ML as a function of twist angle. The uncertainty of the twist angle is smaller than the symbol size. The averaged uncertainty from SHG measurements is indicated by a black double arrow.

The relative twist angles of 33 $MoSe_2$–WSe_2 hetero-BLs are determined by measuring the SHG signal from adjacent ML regions. The extracted twist angles exhibit an average uncertainty of approximately 4°, arising from a combination of systematic error and large-scale twist inhomogeneity across the samples. In 12 of these samples, two to four moiré phonon modes are unambiguously identified in the LF Raman spectra. Four

representative spectra are shown in Fig. 4.2.17**a**, where the moiré modes are marked by black arrows. The observed moiré phonon energies are compared with calculated twist-dependent LA and TA phonon dispersions of ML $MoSe_2$ and WSe_2, allowing the local twist angle to be extracted with an uncertainty of approximately 0.1°. The results for all 12 samples are presented in Fig. 4.2.17**b**, where modes from the same sample are shown in the same color, and the phonon energies shown in Fig. 4.2.17**a** are indicated by diamonds.

In a next step, the local twist angle is further examined for the 55° ± 3° hetero-BL sample, which is highlighted by a white frame in the microscope image in Fig. 4.2.18**a**. To this end, a low-temperature area scan of the IX^0 PL intensities is carried out. The intensities are extracted by fitting the μPL spectra around 1.39 eV with a Gaussian function and are presented as an area heatmap in logarithmic scale in Fig. 4.2.18**b**. In the unpolarized LF Raman spectrum taken at the dark region (indicated by a green circle), four moiré phonon modes are identified (see Fig. 4.2.18**c**). These modes are

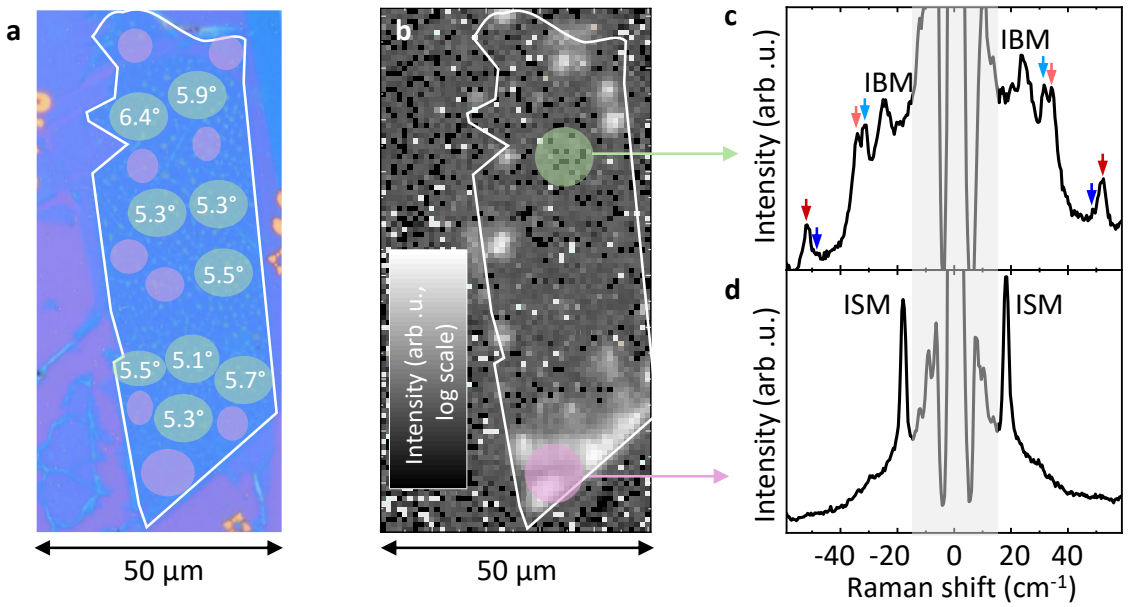

Figure 4.2.18 | a Microscope image of a 55° ± 3° hetero-BL. Pink circles mark regions where the ISM is detected, and green circles indicate regions where moiré-phonon modes are measured. The local twist angles extracted from moiré-mode analysis are labeled. A spatial variation of ≈ 1° is observed and confirmed by sampling multiple positions per region. **b** Heatmap (logarithmic scale) of low-temperature IX^0 PL intensities of the hetero-BL. **c, d** Unpolarized LF Raman spectra from areas marked by green and pink circles in **b**, respectively. Moiré-phonon modes are color-coded according to Fig. 4.2.17**b**, and the ISM and IBM are annotated.

associated with the phonon branches from Fig. 4.2.17**b** and are color-coded accordingly. Additionally, a LF interlayer breathing mode (IBM) is observed, which will be discussed in detail in the following section. In contrast, the unpolarized LF Raman spectrum recorded at the bright IX PL region (marked by a pink circle) reveals an interlayer shear mode (ISM), as shown in Fig. 4.2.18**d**.

A large-scale twist-angle analysis of this sample is presented in the microscope image in Fig. 4.2.18**a**. In the individual green-encircled regions, the local relative twist is identified based on the observed moiré-mode energies, revealing a large-scale twist of approximately $\Delta\theta = 1.3°$ between the respective moiré regimes. Regions where an ISM is detected are marked by pink circles. The emergence of the IX^0 PL is found to correlate with the appearance of the ISM for small twist angles ($\theta \lesssim 4°$) between the individual layers.

Through this hyperspectral analysis, non-invasive and fast insight into the local relative twist of BLs is provided, and the appearance of a LF Raman mode—the ISM—is linked to regions exhibiting bright IX^0 PL. The underlying origin is attributed to spatial relaxation at the atomic scale, as elucidated in the following section.

4.3 Atomic reconstruction

A distinction must be made regarding the choice of material system for BL heterostructures. Besides differences in electronic band alignment, which follow Anderson's rule (see Section 4.1.1), the moiré period exhibits strong twist-angle dependence, particularly for systems with negligible or small lattice mismatch (see Fig. 4.2.3**d**). Especially for near angle-aligned stacking, large moiré periods occur for homo-BLs and $MoSe_2$–WSe_2 hetero-BLs due to no or a small relative lattice mismatch, respectively.

When calculating the stacking energy as a function of stacking configuration, local energy minima are found depending on the stacking type [366–369]. For H-type stacking, the H_h^h configuration is energetically favorable (see Fig. 4.3.1**a**). For R-type stacking, two minima exist: the R_h^X and R_h^M stacking configurations (see Fig. 4.3.1**b**). As a consequence, relaxation of the lattice toward these high-symmetry stackings is energetically favorable for large moiré periods, leading to the formation of domains in which a single atomic registry dominates. However, the fundamental periodicity remains defined by the moiré superlattice. Additionally, domain walls allow the relaxation of strain within

the system [370]. Since R-type stacking produces two stacking minima, whereas H-type produces only one, the resulting domain structures exhibit three and six neighboring domains, respectively, forming trigonal and hexagonal arrangements. These are illustrated schematically in the insets of Figs. 4.3.1**a** and **b**. This atomic reconstruction can be resolved using conductive AFM (CAFM) [368, 369] or STM [275, 369], as exemplified in Figs. 4.3.1**c** and **d**, which are adapted from Ref. [368]. As a result, in a perfectly homogeneous sample, mesoscopic domains form, consisting of high-symmetry stackings [275].

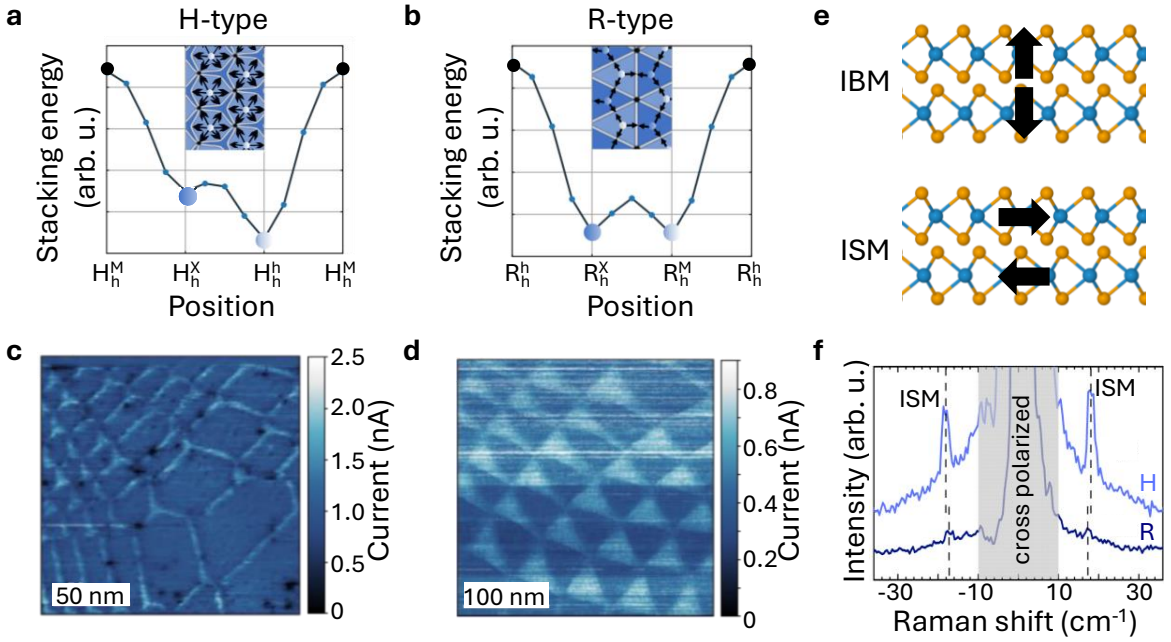

Figure 4.3.1 | Calculated interlayer stacking energy as a function of the stacking configuration for **a** H-type and **b** R-type $MoSe_2$-WSe_2 hetero-BL (adapted from Ref. [368]). The insets show the corresponding reconstructed domains (adapted from Ref. [272]). CAFM measurements of reconstructed **c** H-type and **d** R-type hetero-BLs, respectively (adapted from Ref. [368]). **e** Schematic illustration of the IBM and the ISM. **f** Cross-polarized LF Raman spectra of encapsulated H- and R-type $MoSe_2$-WSe_2 hetero-BL show the redshifted and low-intensity R-type ISM compared to the H-type ISM (adapted from Ref. [371]).

Starting from twist angles $\theta \geq 4°$, the domain size decreases to the extent that reconstruction is no longer energetically favorable. This leads to the formation of a regular moiré superlattice with only minor reconstruction around the high-symmetry points but all the relevant moiré physics instead. Therefore, in reconstructed hetero-BLs, the IX^0 PL (see Section 4.1.2) is bright as the recombination of the electron-hole pairs, situated in the K valleys of the adjacent layers, exists within the light-cone. For larger

twist angles— and thus a regular moiré superlattice—the IX becomes momentum-dark, and the PL consequently quenches [263, 346].

In this thesis, the focus is on the earlier-encountered phononic effects—specifically, the two interlayer Raman modes: the ISM and the IBM. As their names suggest, the ISM corresponds to a shearing motion between the adjacent layers. At the same time, the IBM involves an out-of-plane breathing motion. Both motions are schematically illustrated in Fig. 4.3.1**e**.

The restoring force for both interlayer modes originates from vdW interactions. The IBM is thus primarily sensitive to the interlayer distance. In twisted BLs, the underlying moiré potential induces an undulated interlayer separation [372], which leads to an energy shift of the IBM [211].

In contrast, the ISM depends on the long-range atomic registry. A small in-plane displacement of the energetically favorable stacking configuration results in a restoring force. Therefore, the existence of the ISM requires atomic reconstruction, linking this interlayer phonon mode to the emergence of the bright IX^0 exciton, as observed in Figs. 4.2.17**d, e** in the previous section.

A comparison of the LF Raman spectra of encapsulated H- and R-type $MoSe_2$-WSe_2 hetero-BLs is shown in Fig. 4.3.1**f**. It reveals a significantly lower ISM intensity and a slightly redshifted, by $2\,cm^{-1}$, ISM energy for the R-type stacking [207, 371]. This behavior is attributed to the reduced interlayer bond polarizability in the R-type configuration [207]. In general, the interlayer shear phonon mode is reported to be sensitive to the layer number, lattice constants, stacking configuration, and interlayer distance. As they are, thus, highly specific to each material system and can be used for characterization purposes, they have been extensively studied [152, 204–213, 263, 371, 373–375].

Notably, both interlayer modes can be detected in a co-polarized Raman experiment (see Section 3.1), where the excitation and detection are performed with parallel linear polarizations. A distinction between the ISM and the IBM can be achieved using a cross-polarized Raman configuration, in which the structure is excited with linearly polarized light and the Raman signal is detected through an analyzer oriented perpendicular to the laser polarization. In this orthogonal configuration, the Raman signal of the IBM is strongly suppressed [205, 376, 377].

4.3.1 Emergent trion-phonon coupling in reconstructed $MoSe_2$-WSe_2 heterostructures

For a comprehensive understanding of the phononic properties and potential related insights into the excitonic characteristics of reconstructed $MoSe_2$-WSe_2 hetero-BLs, our findings on emergent trion–phonon coupling reported in Ref. [187] will be discussed in the following.

Here, LF Raman measurements are performed on reconstructed (both R- and H-type) $MoSe_2$–WSe_2 hetero-BLs at cryogenic temperatures using a tunable Ti:Sapphire laser at various excitation energies E_{exc} near the ML exciton resonances. The samples are nominally undoped but have some n-type background doping. An exemplary E_{exc} scan, excited with equidistant energy steps of $\approx 4.5\,\mathrm{meV}$, across the $MoSe_2$ exciton resonances is shown in Fig. 4.3.2**a**, where well-known Raman modes are indicated by arrows. A bright redshifted PL appears in the pink-highlighted spectra when the excitation is resonant with the $MoSe_2$ X^0 transition. This peak is identified as the HX^- quasi-particle, introduced in Section 4.1.2. The emergence of the HX^- PL under X^0 excitation corresponds to a phonon-assisted down-conversion process, analogous to the one discussed earlier in $MoSe_2$-WS_2 hetero-BLs, without the required lateral energy transfer and without electrostatic doping control. In nonresonant μPL measurements, good interlayer contact is confirmed by the quenched intralayer PL and a bright IX^0 signal.

An evaluation of the RF at an arbitrary Raman shift of $12\,\mathrm{cm}^{-1}$ reveals an energy difference of approximately 25 meV between the X^0 and HX^- peaks. This indicates a reduced binding energy (of $\approx 4\,\mathrm{meV}$) for the HX^- quasi-particle in the hetero-BL compared to the X^- trion in a $MoSe_2$ ML (see Fig. 4.3.2**c**). This observation is further supported by calculations of the trion binding energy as a function of charge separation distance [378]. The argument also holds for a hybridized Fermi sea, which would give rise to hybridized Fermi polarons, thereby establishing a more universal picture.

Furthermore, the measurements in Fig. 4.3.2**a** reveal an emergent LF Raman excitation that appears in resonance with the $MoSe_2$ and WSe_2 HX^-, which is labelled the hybrid shear mode (HSM). The Raman signal is extracted by subtracting the RF background, which is obtained by an exponential decay fit and is displayed for H- and R-type heterostructures excited at the $MoSe_2$ and WSe_2 HX^- resonance in Fig. 4.3.2**b**. Notably, the HSM resonance coincides with the HX^- resonances (see Fig. 4.3.2**c**). Here, the

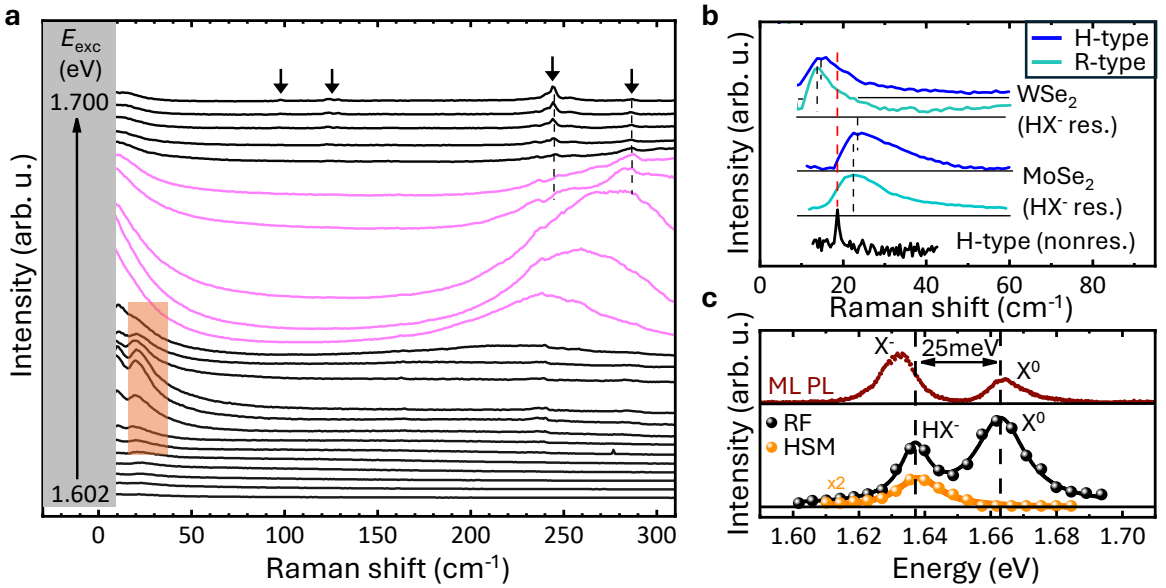

Figure 4.3.2 | a Resonant Raman excitation energy scan of an R-type $MoSe_2$-WSe_2 hetero-BL displayed as a waterfall plot of the individual LF spectra. E_{exc} increases from bottom to top in equidistant energy steps of approximately 4.5 meV. Well-known ML Raman peaks are indicated by arrows, and the pink spectra are excited in resonance with $MoSe_2$ X^0. A LF Raman peak emerges within the orange-shaded region. **b** Comparison of the background-subtracted HSM from H-type and R-type samples at two different excitation energies: $E_{exc} \approx 1.722$ eV, corresponding to the WSe_2 HX^- resonance (top), and $E_{exc} \approx 1.630$ eV, corresponding to the $MoSe_2$ HX^- resonance (bottom). A nonresonant Raman spectrum from an H-type sample is shown at the bottom for comparison to the ISM. **c** The nonresonant PL spectrum from a $MoSe_2$ ML region (upper panel) is compared to the RF intensity taken at a Raman shift of 12 cm^{-1} (black dots, lower panel) and to the HSM intensities (orange dots, lower panel). The solid lines in the lower panel represent Loretzian fits to the experimental data. (Adapted from Ref. [187])

phonon energy depends not only on the stacking configuration—similar to nonresonant room-temperature experiments [371]—but also on the resonance condition, i.e., whether the excitation energy is tuned to the $MoSe_2$ or WSe_2 HX^- (see Fig. 4.3.2**b**). An excitation at the $MoSe_2$ HX^- resonance yields a Raman mode at ≈ 22 cm^{-1}, whereas an excitation at the WSe_2 HX^- results in a redshifted and roughly four times weaker mode, indicating reduced phonon coupling. Here, the observed asymmetric lineshape is attributed to either a recoil effect on the remaining electron [379] or the k-dependent electron-phonon coupling.

A detailed description of the implementation of the trion envelope wavefunction and the calculation of the Raman intensity, based on electron–phonon coupling, can be found in Ref. [378]. These theoretical results predict that the electron–phonon cou-

pling strength depends on specific regions in momentum space. The results are visualized in Fig. 4.3.3**a**, where the single-particle shear mode coupling strength g for an R-type hetero-BL is projected onto the first BZ. The resulting trion–phonon coupling agrees well with the experimental observations, as only the HX^-—which includes an additionally bound electron at the Q valley—leads to interlayer coupling. Further supporting this picture is the polarization dependence of the HSM. Unlike the ISM, the HSM adopts the trion polarization and can therefore only be detected in a co-polarized configuration.

When an out-of-plane magnetic field is applied, time-reversal symmetry is broken, lifting the valley degeneracy. The energy shift of the individual valleys—and consequently of the corresponding quasi-particles—can be calculated using density functional theory with first-order perturbation theory [272, 380–382]. Experimentally, the individual valleys can be selectively addressed by exciting with $\sigma^{\pm}$ circularly polarized light and measuring the corresponding energies, $E_{\sigma^{\pm}}$. The resulting energy splitting is expressed as

$$E(B) = g\mu_B B, \tag{4.3.1}$$

where μ_B is the Bohr magneton, B is the externally applied out-of-plane magnetic field and g is the exciton gyromagnetic factor.

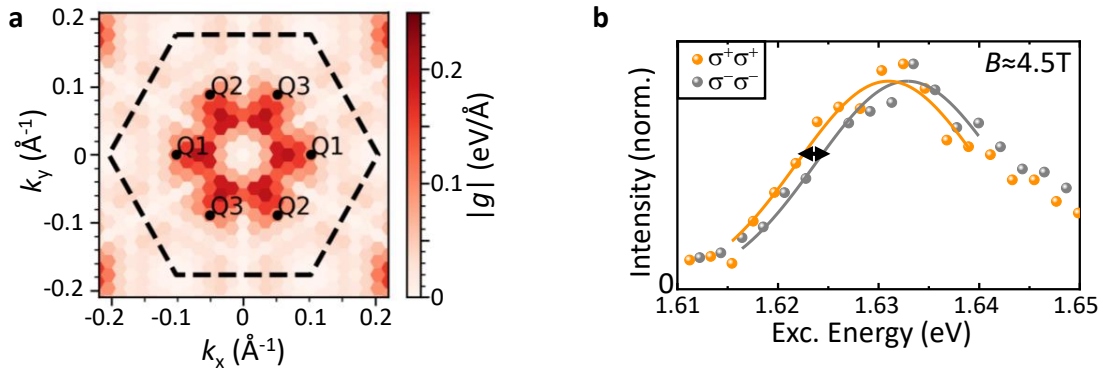

Figure 4.3.3 | **a** Contour plot of the single-particle shear mode coupling strength projected in the first BZ of the R-type hetero-BL. **b** RF signal intensity as a function of E_{exc} from circularly polarized excitation and detection of LF Raman spectra under an out-of-plane magnetic field $B \approx 4.5$T. The experimental data for the σ^+ (σ^-) excitation and σ^+ (σ^-) detection configuration are shown as orange (gray) dots. Gaussian fits to the data in the range $1.615\,\text{eV} \leq E_{exc} \leq 1.640\,\text{eV}$, with identical amplitude, offset, and FWHM, are shown as solid lines.

The theoretical prediction can be compared to the experimentally extracted effective g_{eff}-factor, defined as

$$g_{\text{eff}} = \frac{E_{\sigma^+} - E_{\sigma^-}}{\mu_{\text{B}} B}. \tag{4.3.2}$$

This effective g_{eff}-factor differs significantly between intra- and interlayer excitons.

The experimental g_{eff} values for TMDC intralayer excitons are typically around -4 [107, 114, 381]. In contrast, for interlayer excitons in $MoSe_2$-WSe_2 hetero-BLs, g_{eff} depends strongly on the stacking configuration. For the most prominent stackings in R-type BLs, the interlayer exciton g-factors are approximately $g_{\text{eff}} \approx 6$ for $\text{R}_{\text{h}}^{\text{X}}$ and $g_{\text{eff}} \approx 10$ for $\text{R}_{\text{h}}^{\text{M}}$. In the $\text{H}_{\text{h}}^{\text{h}}$ configuration, a much larger negative value of $g_{\text{eff}} \approx -16$ is documented [272, 275]. These distinct g-factor values between intra- and interlayer excitons offer a powerful tool for probing excitonic character and gaining real-space insight into the stacking configuration and into novel excitonic effects.

A magnetic field study of the HX^- g_{eff}-factor is conducted on an R-type $MoSe_2$-WSe_2 hetero-BL. The RF signal, shown in Fig. 4.3.3**b**, is extracted from LF Raman spectra taken at $B \approx 4.5\,\text{T}$ in a $\sigma^\pm$ co-polarized detection setup—that is, with identical circular polarizations in both excitation and detection—tuned close to the $MoSe_2$ HX^- resonance and evaluated at an arbitrary Raman shift of $14\,\text{cm}^{-1}$. Gaussian fits to the $\sigma^\pm$ experimental data, using shared amplitude, offset, and FWHM in the excitation energy range $1.615\,\text{eV} \leq E_{\text{exc}} \leq 1.640\text{eV}$, yield an energy difference of $E_{\sigma^+} - E_{\sigma^-} \approx -2\,\text{meV}$. Using Eq. 4.3.2, this corresponds to a $g_{\text{eff}} = -7.7 \pm 2$. The relatively large uncertainty reflects both fitting error and a systematic uncertainty due to the modified cryostat, where the magnetic field strength can only be estimated due to the piezos elevating the sample beyond the maximal magnetic field position [383].

Using this extracted g_{eff} value, which matches closely the known R-type IX^0 g-factor of ≈ 6, and lies between the interlayer and intralayer g-factors of ≈ 10 and 4, respectively, supports the hybridized character of the HX^- over both layers. This provides direct experimental evidence that the additionally bound electron is hybridized across both layers.

To enable a more systematic and precise investigation of HX^- g-factors in both H- and R-type $MoSe_2$-WSe_2 hetero-BLs, higher-quality samples are required—ideally with reduced RF linewidths approaching the exciton lifetime limit.

4.3.2 Programmable trion-phonon coupling

Having introduced the emergent trion-phonon coupling in reconstructed heterostructures, the question arises whether this coupling can be exploited in a programmable device by controlling the doping of the hetero-BL—and thereby enabling or disabling the coupling.

In this investigation, three H-type gated devices (S1–S3) fabricated by Jakob Lichtenberger [384] are examined individually, as significant discrepancies are observed among them. The devices are built equivalently to the earlier introduced $MoSe_2$-WS_2 devices, schematically depicted in 3.2.2**a** but with a WSe_2 ML instead of WS_2. The hetero-BL is encapsulated between two hBN flakes with equivalent thicknesses, and a graphite flake in direct contact with the heterostructure functions as the ground electrode. A top and bottom graphite flake serves as a top and bottom gate, enabling electrostatic doping. All TMDC MLs are CVD-grown, except the WSe_2 ML in sample S3, which is exfoliated. In contrast to the earlier devices, platinum contact pads are used in samples S1 and S2.

First, the nonresonant, doping-dependent PL spectra of each sample are analyzed and presented in Figs. 4.3.4**a, c** and **e**. The corresponding doping-dependent LF Raman spectra, taken near the $MoSe_2$ HX^- resonance, are shown in Figs. 4.3.4**b, d** and **f** and discussed for each device in parallel. The applied voltages are symmetrically applied between the top and bottom gates. All measurements are performed with an excitation energy resonant with the $MoSe_2$ HX^-, due to the strong trion-phonon coupling observed at this resonance. All results are documented in Jakob Lichtenberger's Master's thesis [384].

The sample S1 exhibits, under nonresonant excitation, a quenched intralayer PL and broad IX^0 PL peaks at approximately 1.34 eV and 1.39 eV, confirming again good interlayer contact. The high-energy (1.39 eV) PL, shown in Fig. 4.3.4**a**, can be attributed to the H-type stacking and the low-energy (1.34 eV) one to the adjacent R-type domain [276]. Both PL signatures can be detected simultaneously due to a mirror twin boundary in the used CVD-grown ML [368], resulting in neighboring R- and H-type stacking configurations within a single sample. The discussion will focus on the IX peaks at 1.39 eV, which are shown in Fig. 4.3.4**a**, as they correspond to the resonant Raman measurements. Upon applying a gate voltage, the IX peaks at an energy

of around 1.39 eV show a doping-dependence. They can be identified by referring to the energies introduced in Fig. 4.1.3. At a gate voltage of $-0.75\,\mathrm{V}$, the asymmetric PL peak has distinct high- and low-energy shoulders. The energy separation between these signatures is approximately $10\,\mathrm{meV} \pm 2\,\mathrm{meV}$—similar to the previously reported 7 meV separation between the charged and neutral $\mathrm{IX_T}$ states. Since the high-energy peak disappears at both higher and lower gate voltages, this spectrum likely corresponds to the charge-neutral doping regime, with additional broadening caused by local charging inhomogeneities, as discussed in Section 4.2.1.

Repeated measurements show that the voltage corresponding to the neutral regime shifts between cooling cycles, preventing a reliable comparison between gate voltages in the PL- and resonant LF Raman experiments. In the PL, an unidentified PL peak emerges about 18 meV above the $\mathrm{IX_T^+}$ at $U_\mathrm{G} = -1.25\,\mathrm{V}$. This resonance may be attributed to the positively charged triplet exciton, where the additionally bound hole resides in the opposite valley of the triplet exciton. At higher doping levels (e.g., $U_\mathrm{G} = 2\,\mathrm{V}$ or $U_\mathrm{G} = -6\,\mathrm{V}$), the IX peaks are quenched. This behavior is consistent with plasma screening [314] and state-filling effects, wherein the presence of free carriers screens the Coulomb interaction and occupies the band-edge states that are required to form excitons [133].

After confirming the device's functionality via PL measurements, resonant LF Raman measurements at the $\mathrm{MoSe_2}$ $\mathrm{HX^-}$ resonance are performed on sample S1. The resulting spectra are shown in Fig. 4.3.4**b**, with an equidistant offset applied for visual clarity. A clear HSM, marked by an asterisk, is observed, along with the appearance of a RF signal—but only at positive gate voltages.

The HSM's energy remains constant across the measured doping range. The intensities of both the RF and HSM signals initially increase with rising positive gate voltage, but then decrease at higher doping levels. This trend is similar to the doping dependence of the interlayer PL and aligns well with the plasma screening and state-filling arguments. The transition from negative doping to the charge neutrality point occurs approximately between the two pink-highlighted spectra, where the RF signal vanishes due to the absence of background doping and, consequently, the disappearance of the repulsive Fermi-polaron's oscillator strength.

Interestingly, both the HSM and RF signals are absent in the positive-doping regime, despite the presence of the positively charged hybrid trion $\mathrm{HX^+}$ in the PL spectra. The lack of HSM signal can be attributed to the fact that the additional hole in the $\mathrm{HX^+}$ is

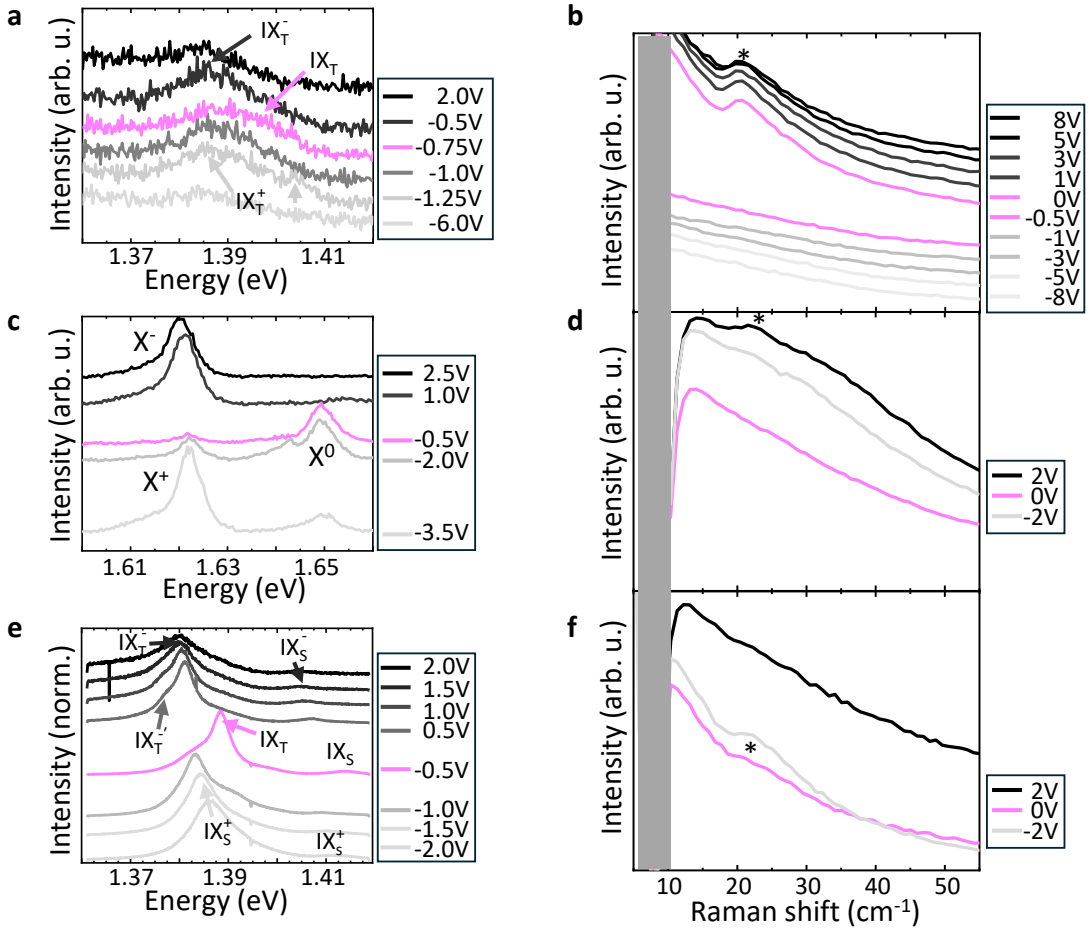

Figure 4.3.4 | a, c, e Nonresonant doping-dependent PL spectra of samples S1-S3 (from top to bottom). The applied voltages are symmetrically applied to both the top and bottom gates. An individual vertical offset is added to each spectrum for clarity. The spectra in **e** are normalized. **b, d, f** Doping-dependent LF Raman spectra of samples S1–S3 (from top to bottom), recorded with excitation at the $MoSe_2$ HX^- resonance. The positive and negative doping regimes are indicated in gray and black, respectively. The HSM is indicated by asterisks. An equidistant vertical offset is added to the spectra in **b** for better visibility.

located at either the K- or the Γ valley, neither of which couples effectively to the shear mode (cf. Fig. 4.1.2**a** and Fig. 4.3.3**a**). Notably, the RF signal associated with the HX^+ is significantly weaker than that of the HX^-, for reasons that remain unclear, as the 4 meV offset between the trion resonances, as seen in PL measurements, would account for only a minor decrease. Further measurements cannot be performed on sample S1, as the device became defunct during subsequent experiments.

Similarly, for the sample S2, the nonresonant PL spectra are shown in Fig. 4.3.4**c** with an arbitrary vertical offset for clarity. The displayed spectral region corresponds to the intralayer PL, as the interlayer PL is very weak, which suggests a poor interlayer contact. Nevertheless, the intralayer PL exhibits the typical doping-dependent behavior reported in Ref. [133].

Despite this, doping-dependent LF Raman measurements with excitation tuned to the $MoSe_2$ HX^- resonance reveal a distinct LF Raman mode, as is shown in Fig. 4.3.4**d**. Here, the RF signal displays a clear minimum near zero doping at 0 V and increases symmetrically with both positive and negative doping. The HSM is unambiguously identifiable at the negative-doping regime and absent at the positive-doping regime, despite the bright intralayer RF signal.

The absence of a discernible IX PL raises questions about the sample quality, particularly regarding the interlayer coupling, which appears to be weaker compared to other samples.

For the third sample S3, the nonresonant μPL spectra shown in Fig. 4.3.4**e** exhibit bright IX^0 peaks with a narrow linewidth of approximately 4 meV, enabling a clear identification of charge-neutral and charged singlet (IX_S) and triplet (IX_T) states, in accordance with Fig. 4.1.3. Near charge neutrality, at -0.5 V, the IX_S and IX_T are observed at 1.414 eV and 1.388 eV, respectively, showing the well-known singlet-triplet splitting of 26meV [279].

Upon electron doping (positive voltages), the IX peaks shift to lower energies by ≈ 7 meV, which is consistent with literature values for the charged triplet state. The redshift of both peaks with increasing applied voltage suggests coupling between a finite out-of-plane electric field to the interlayer exciton, potentially caused by an asymmetry in the hBN layer thicknesses. Additionally, a broad low-energy shoulder around 1.377 eV may correspond to the excited charged triplet state, $IX_T^{-\prime}$. For hole doping (negative gate voltages), redshifted singlet and triplet trions are observed, with an energy shift of ≈ 5 meV.

The corresponding doping-dependent resonant LF Raman spectra are displayed in Fig. 4.3.4**f**. As in sample S2, the RF signal exhibits a minimum near charge neutrality and increases for both electron and hole doping. In contrast to earlier observations, the HSM appears only under hole-doped conditions.

In conclusion, the resulting overall picture of the trion-phonon coupling of the HX^- to the ISM remains unclear. However, the fabricated samples demonstrate a clear degree of programmability, as the coupling can be effectively switched on or off by tuning the system into or out of charge neutrality. While the current model—suggesting that additional free holes reside at the K or Γ valleys and therefore do not couple to the ISM—is consistent with some observations, it cannot be definitively confirmed. Notably, sample S3 exhibits behavior that contradicts this interpretation, suggesting that further statistics is needed to fully validate the model.

4.3.3 Probing hybridization of excitonic complexes in reconstructed WSe_2 homobilayers

Having demonstrated a programmable trion-phonon coupling in reconstructed $MoSe_2$-WSe_2 hetero-BLs, the next step is to investigate the HSM signal in other vdW stacks. The presence of trion–phonon coupling provides insight into the electron distribution in both real and reciprocal space, specifically by revealing the hybridized nature of the additionally bound Q-valley electron.

A natural starting point is WSe_2 homo-BL systems, as both theoretical and experimental foundations—particularly for atomically reconstructed BLs—are already partially established in the literature.

It is well known that both H- and R-type WSe_2 homo-BLs are momentum-indirect semiconductors [201, 203, 254], hosting momentum-dark excitons composed of an electron at the Q valley and a hole at the K valley at an energy $\approx 1.55\,\mathrm{eV}$. In H-type stacking, the electron state hybridizes across the two layers, resulting in an exciton with a mixed intralayer and interlayer character. In contrast, the R-type stacking leads to an exciton with a predominantly interlayer character, as the electron is localized in the layer opposite to the hole [200, 201, 385]. These momentum-dark excitons give rise to phonon-assisted PL peaks—labeled P_1 to P_4 for H-type stacking and P_1 to P_4 and P'_1 to P'_3 for R-type stacking—where one or multiple phonons mediate the radiative decay process [130, 200, 381].

The phonon-assisted PL signatures are observable in the PL spectra in Figs. 4.3.5**a, b** for the H-type and in Figs. 4.3.6**a, b** for the R-type homo-BL. For both stackings, the spectra shown in the panels **a** are taken from Ref. [200] and serve as a reference

for comparison with the corresponding measured spectra in panels **b**, recorded on the samples used in this thesis for the following resonant Raman measurements.

The measured momentum-dark P_1 to P_4 transitions in the H-type BL agree well with Ref. [200], though slight variations in the relative intensities and larger FWHM are observed. For the R-type stacking, the measured PL in Fig. 4.3.6**b** is broader and weaker but appears at the same energies as in Ref. [200]. As shown in the RC spectra of Ref. [200], the absence of absorption near the P_1–P_4 energies confirms their momentum-indirect nature.

In the following, the focus shifts to the direct intralayer excitonic resonances and their coupling to phonons, which will be discussed separately for the H-type and R-type configurations.

In the H-type configuration, the 60° twist between the layers aligns the K point of one layer with the K′ point of the other, rendering the BL centrosymmetric in both real and reciprocal space. The lowest-energy, spin-allowed optical transition at the K and K′ points corresponds to the neutral intralayer exciton X^0, which are energetically degenerate. Their PL and RC signature can be seen in Fig. 4.3.5**a** at $\approx 1.713\,\mathrm{eV}$. The corresponding excitonic transition at the K point of one layer is illustrated schematically in Fig. 4.3.5**c**, where the layer number and the spin orientations of the bands are color-coded.

The background doping electrons occupy the Q or Q′ valleys, where they are hybridized across both layers [203]. This gives rise to the formation of bright hybrid trions, HX^-_{QK} and $HX^-_{Q'K}$, where the first index denotes the momentum-space location of the background electrons and the second corresponds to that of the electron-hole pairs, as schematically depicted in Fig. 4.3.5**d**. This figure simplifies the situation by showing the X^0 located at the K point of one layer within the first BZ, along with the two possible configurations of the background-doping electron that is additionally bound. The vertical direction serves as a proxy for real-space distribution, highlighting the hybridization of electrons at the Q and Q′ points across the two layers.

Notably, the differing real-space distributions of the hybrid trions, i.e., one electron is closer to the exciton, lead to distinct binding energies: $E_B(HX^-_{Q'K}) = 2\,\mathrm{meV}$ and $E_B(HX^-_{QK}) = 18\,\mathrm{meV}$ [386]. It is debatable whether the small binding energy of 2 meV results in a bound trion state.

The measurements are performed on two naturally stacked WSe_2 homo-BLs, WBL-H1 and WBL-H2, both of which exhibit intrinsic negative doping. The normalized non-resonant µPL spectrum of sample WBL-H1, displayed in Fig. 4.3.5**b**, shows a broad, low-intensity excitonic peak at ≈ 1.713 eV along with the earlier discussed pronounced phonon sidebands at ≈ 1.55 eV. All PL signatures are in agreement with Ref. [200], shown in Fig. 4.3.5**a**. The high-energy peak at ≈ 1.713 eV exhibits a low-energy shoulder at ≈ 1.70 eV, indicating a double-peak structure with an energy splitting of approximately 16 meV. This may originate from a superposition of HX^-_{QK} and $HX^-_{Q'K}$ emission due to the intrinsic negative doping of the sample. However, a neutral X^0 PL

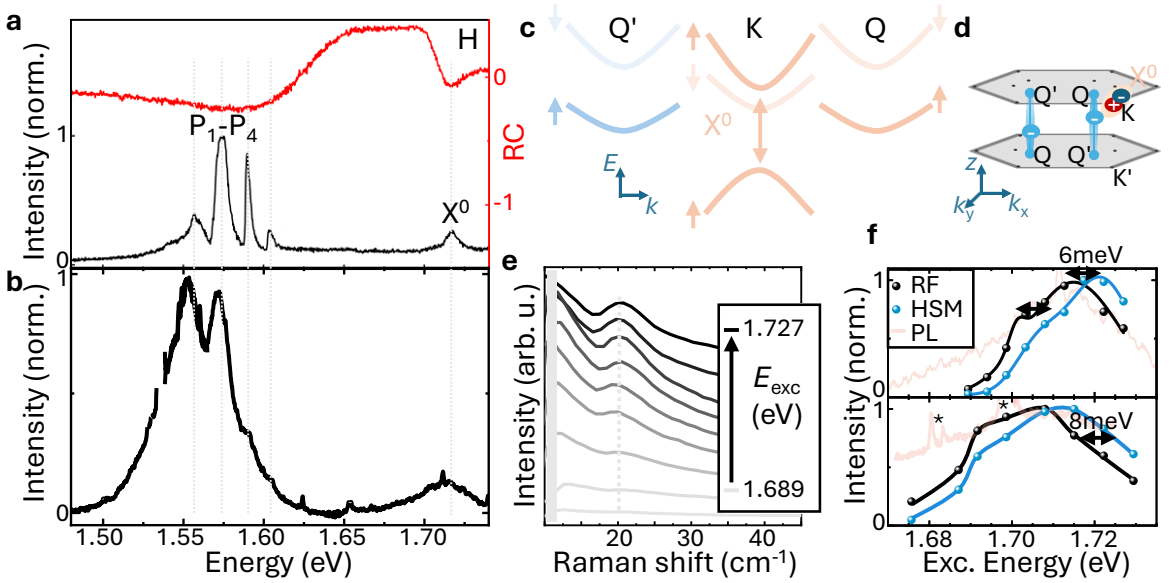

Figure 4.3.5 | Exciton and trion picture of H-type and WSe_2 homo-BLs. **a** Nonresonant PL and RC spectrum (adapted from Ref. [200]) and **b** μPL spectrum from sample WBL-H1. The phonon sideband peaks P_1-P_4 and the exciton peak X^0 are highlighted in **a**. **c** Schematic illustration of the dipole-allowed X^0 transition at the K point. Selected valleys from layer one and layer two are shown in orange and blue, respectively. **d** Illustration of the valley and layer configuration of the bright H-type WSe_2 X^-s consisting of a bright exciton at the K point in the first BZ and an additional hybridized electron at either the Q or Q′ point. This leads to two bright HX^- configurations (cf. Ref. [203]). **e** Waterfall plot of resonant LF Raman spectra measured at various excitation energies E_{exc}. The HSM is marked with a gray dotted line. **f** Normalized RF signal and HSM intensity as a function of E_{exc} for sample WBL-H1 (top panel) and WBL-H2 (bottom panel). A blowup of the PL spectrum from **b** and the PL, with $E_{exc} = 1.73$ eV, belonging to sample WBL-H2, is added in orange to the upper and lower panel, respectively. WSe_2 Raman modes are marked by asterisks. Solid lines are bigaussian fits in the upper plot and guides to the eye in the lower one, revealing an energy offset of 7 ± 2 meV.

peak, as seen in Fig. 4.3.5**a** from Ref. [200], contributing to the PL spectrum cannot be ruled out.

Next, resonant LF Raman measurements are performed near the observed excitonic resonances using excitation energies ranging from 1.689 eV to 1.727 eV in steps of approximately 5 meV. The resulting spectra are displayed as a waterfall plot in Fig. 4.3.5**e**. An asymmetric LF Raman mode emerges at $\approx 20.5\,\mathrm{cm}^{-1}$, which is again labeled as the HSM.

The HSM intensity is extracted after subtracting the background RF signal. It is plotted alongside the RF signal as a function of the excitation energy in Fig. 4.3.5**f** for sample WBL-H1 in the upper panel and for sample WBL-H2 in the lower panel. For comparison, a magnified view of the PL spectrum from Fig. 4.3.5**b** is included in the upper panel, and the PL spectrum of sample WBL-H2, excited at 1.73 eV, is shown in the lower panel. In the latter, well-known intralayer Raman modes are marked by asterisks [154–161], as the excitation is near-resonant. The HSM intensity tracks the RF signal strength but is spectrally blueshifted by approximately 7 ± 2 meV. Both signals exhibit an asymmetric shape that resembles the corresponding PL spectrum. Additionally, a second lower-energy peak in the low-energy shoulder is revealed by fitting the intensity curves with bigaussian functions, yielding a peak separation of $\approx 15 \pm 3$ meV. For the second sample, however, the fits exhibit large uncertainties, as single Gaussian functions already provide an adequate description. Therefore, only the apparent peak energy is extracted for this sample.

Further measurements reveal a linear power dependence for both the HSM and RF signals, ruling out a biexcitonic origin. Moreover, the HSM is observable only in a co-polarized detection setup, indicating that it follows the polarization of the trion—consistent with the behavior of the HSM observed in reconstructed hetero-BLs [187].

The HSM is blueshifted relative to the RF signal, suggesting that the RF signal is not solely due to HX^- trions but may also be due to ML trions with larger binding energies [187]. This implies that the observed PL and RF signals may have ML contributions that are decoupled from the H-type homo-BL structure. This can be due to the imperfect interfacial contact or strain, introduced during the fabrication process. Consequently, the HSM signal is interpreted independently of the RF signal. Here, the observed energy separation of $\approx 15 \pm 3$ meV between the two maxima of the HSM signal is attributed to two resonances that may correspond to the bright hybrid trions $\mathrm{HX}^-_{\mathrm{QK}}$ and $\mathrm{HX}^-_{\mathrm{Q'K}}$. This value agrees well with the theoretically predicted energy splitting of

16 meV reported in Ref. [203], confirming current exciton and trion picture in H-type WSe_2 homo-BLs. Further statistical analysis is required to clarify the origin of the ≈ 10 meV HSM resonance energy offset observed between the samples.

The H-type WSe_2 homo-BL serves as a model system, in which the HSM signal probes the trion–phonon coupling and reveals the hybridized nature of trion complexes with an additional Q-valley electron. Building on this understanding, the HSM signal is further employed to probe the hybridized nature of excitonic complexes in R-type WSe_2 homo-BL configurations.

In the R-type configuration, spatial inversion symmetry is broken, leading to the lifting of the energy degeneracy of the free charges and the neutral exciton X^0. As a result, it becomes energetically favorable for free charges to localize predominantly in one layer, resulting in a polar, ferroelectric homo-BL [215–223, 225, 387, 388]. This interlayer asymmetry in the excitonic landscape can be seen in an energy splitting of approximately 17 meV of the intralayer excitons—denoted as X_1^0 (in layer 1) and X_2^0 (in layer 2). This is due to asymmetric VB and CB offsets [200, 220, 385, 389], as schematically illustrated in Fig. 4.3.6**c**, where the K valley and selected Q and Q′ valleys are color-coded orange and blue for layers 1 and 2, respectively. The layer labeling is arbitrary, as the layer polarization can be reversed by applying an external out-of-plane electric field [215, 217, 223, 390]. Both polarization states typically coexist in neighboring domains.

The lowest-energy dipole-allowed transitions occur at the K and K′ valleys, and are depicted in Fig. 4.3.6**c** for the K valley. Magneto-PL studies in Ref. [200] confirm the intralayer character of both X_1^0 and X_2^0 by extracting their g_{eff}-factors. The free electrons localize at the Q and Q′ points of one layer. The again simplified BZ schematic in Fig. 4.3.6**d** shows the bright excitons X_1^0 in layer 1 and X_2^0 in layer 2 at the K points. The vertical direction illustrates the real-space interlayer distance and highlights electron localization at the Q and Q′ points of layer 1, resulting in an intralayer trion (X_1^-) and a hybrid trion (HX_2^-).

The charge-neutral excitons X_1^0 and X_2^0 in R-type BLs exhibit an energy splitting of approximately 16–20 meV [200, 220, 385], shown in the PL and RC spectra in Fig. 4.3.6**a**. The binding of an additional electron to form the trions X_1^- and HX_2^- causes a redshift of the PL peaks relative to their neutral counterparts.

The experimental investigations in this thesis are performed on an R-type WSe_2 homo-BL capped by hBN with a nominal twist angle of 0.8°. The corresponding nonresonant PL spectrum is shown in Fig. 4.3.6**b** next to the previously explained PL spectrum from Ref. [200] in Fig. 4.3.6**a**, which displays both the direct and momentum-dark exciton emissions. In contrast, whereas Fig. 4.3.6**a** clearly resolves the two neutral exciton peaks X_1^0 and X_2^0, the spectrum in Fig. 4.3.6**b** is dominated by several peaks characteristic of WSe_2 ML PL. This dominant ML-like emission indicates imperfect interlayer coupling, likely caused by poor interfacial contact. As a result, the ML PL obscures the spectral region in which X_1^0, X_2^0 and their respective trions are expected tp appear in

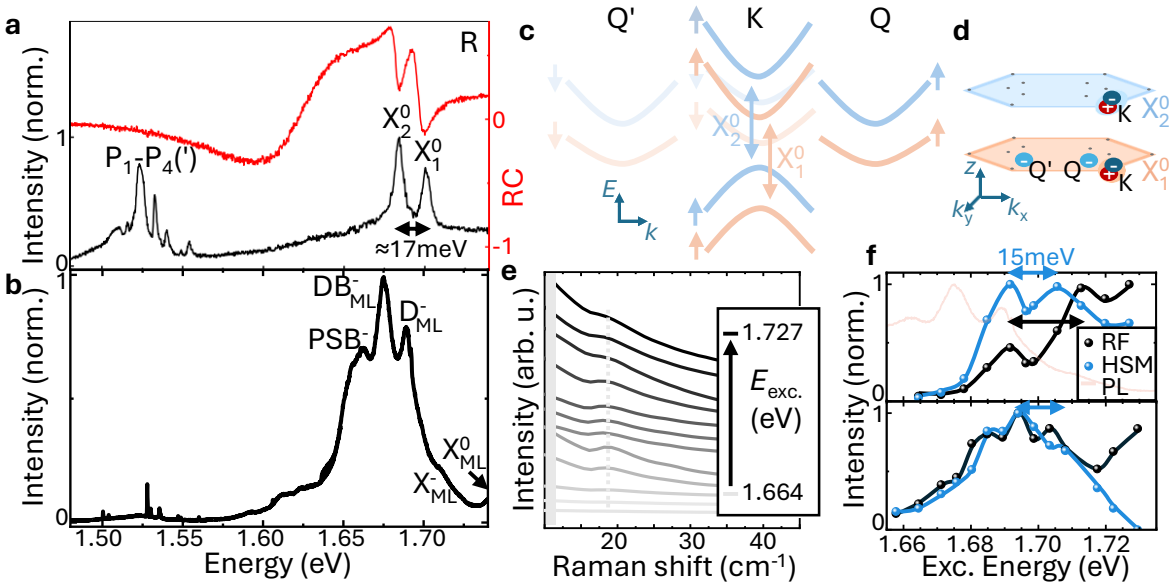

Figure 4.3.6 | Exciton and trion picture of R-type and WSe_2 homo-BLs. **a** Nonresonant PL and RC spectra (adapted from Ref. [200]) and **b** PL spectrum from spot A of sample WBL-R. The phonon sideband PL peaks P_1-P_4 and P'_1–P'_3 of the two momentum-dark excitons and the two bright exciton peaks X_1^0 and X_2^0 are highlighted in **a**. The ML WSe_2 exciton PL peaks X^0_{ML}, X^-_{ML}, D^-_{ML}, DB^-_{ML} and PSB^-_{ML} in **b** arise due to imperfect contact between the layers. **c** Schematic of the dipole-allowed intralayer transitions. Selected valleys in orange and blue represent layer 1 and layer 2, respectively, as the intralayer degeneracy is lifted in the R-type stacking. **d** Illustration of the valley and layer configuration of the bright R-type WSe_2 X^-s consisting of one of the bright excitons X_1^0 or X_2^0 and a localized electron from layer 1, resulting in X_1^- and HX_2^- (cf. Ref. [203]). **e** Waterfall plot of resonant LF Raman spectra measured at various excitation energies E_{exc}. The HSM is indicated by the gray-dotted line. **f** Normalized RF signal and HSM intensity plotted as a function of E_{exc} for spot A (upper panel) and spot B (lower panel) of sample WBL-R. A magnified view of the PL spectrum from **b** is overlaid in orange in the upper panel. Arrows indicate the energy offset between the HSM and RF maxima. Solid lines are guides to the eye.

an R-type WSe_2 homo-BL. The observed PL signatures can be assigned to the neutral exciton (X^0_{ML}), intralayer trion (X^-_{ML}), dark trion (D^-_{ML}), charged biexciton (XB^-_{ML}), and phonon-assisted sidebands (PSB^-_{ML}), as described in Ref. [144] and Section 2.3.2.

LF Raman measurements similar to those performed on the H-type samples are carried out with excitation energies around the intralayer K-valley transitions and are displayed in Fig. 4.3.6**e**. A LF Raman mode emerges at approximately 18.5 cm^{-1} with varying intensity, marked by a gray-dotted line. The energy of this HSM is lower than that observed in H-type samples, indicating a weaker interlayer coupling consistent with observations in reconstructed $MoSe_2$-WSe_2 hetero-BLs [187, 371].

An analysis of the RF signal and HSM intensities as a function of excitation energy is presented for two exemplary sample spots, alongside a close-up of the PL spectrum from Fig. 4.3.6**b**, in the two panels of Fig. 4.3.6**f**. The RF signals from five out of six investigated spots exhibit at least two intensity maxima near ≈ 1.71 eV and ≈ 1.69 eV, with the energy difference varying between 15-25 meV. The relative intensity ratio of these peaks varies significantly across spots, but in four of six cases, the lower-energy peak dominates. The observed RF signal could also be attributed to ML-like intralayer PL contributions, where multiple quasi-particles with similar energies coexist, as identified in the nonresonant PL measurements. Notably, the increase in RF intensity at higher excitation energies is attributed to the ML neutral exciton X^0_{ML}.

The HSM intensities display two distinct maxima, separated by approximately 15 meV. Additionally, an asymmetric low-energy shoulder around 1.685 eV is observed in four of the measured spots, as shown in the lower panel. The HSM resonance near 1.69 eV consistently coincides with the maximum of the RF signal and corresponds to the highest HSM intensity. The energy difference of ≈ 15 meV between the HSM resonance maxima is only slightly smaller than the reported splitting of $\approx$ 16–20 meV between the neutral excitons X^0_1 and X^0_2, suggesting a possible link to trion resonances.

The energy shift of trions compared to the excitons may, hereby, be partially compensated by differences in the dielectric environment, as the investigated sample is hBN-capped, whereas the samples in Ref. [200] are fully hBN-encapsulated. Therefore, only the energy difference, which can be estimated by the trion binding energies, is indicative of the origin of the HSM resonances.

In order to estimate the X^-_1 binding energy, a comparison is made to the hetero-BL case from Ref. [187], where binding energies are calculated as a function of the electron-hole

separation distance at the Q valley. For a charge separation near zero, i.e., an intralayer trion, the binding energy amounts to approximately 26 meV. In contrast, the hybrid trion HX_2^- exhibits a reduced binding energy of a few meV due to the electron being reported as localized in the adjacent layer [203]. Taken together, only a minor energy difference between the trions is expected compared to the neutral-exciton splitting using this microscopic picture. It qualitatively explains the observed reduction in trion energy splitting, which is not seen for all measured spots. Furthermore, the reduction in binding energy illustrates the strong dependence of trion stability on the degree of hybridization.

An assignment of the HSM maxima to the trion resonances X_1^- and HX_2^- by the observed energy difference is, therefore, tentative at best. The low-energy HSM peak at $\approx 1.69\,\mathrm{eV}$—which consistently exhibits the strongest HSM signal—is hereby related to the hybrid trion HX_2^-.

However, if the additionally bound electron of the intralayer trion X_1^- were fully localized within the same layer, no trion-phonon coupling—and thus no HSM—would be expected. The observation of a finite HSM signal therefore suggests partial hybridization of the Q-valley electron. This interpretation is supported by Ref. [220], which predicts hybridization across both layers at the global CB minimum at the Q valley. Moreover, it is possible for the shearing motion to introduce a time-dependent modulation of the electrons' probability density, resulting in a time-dependent deviation from perfect electron localization in a single layer. Gaining supporting experimental evidence for this time-dependent consideration remains elusive, as the HSM's low energy impedes time-resolved experiments with energetically broad laser pulses.

These investigations of the trion-phonon coupling provide experimental evidence for the hybridized nature of the additionally bound electrons at the Q valley, supporting the theoretical predictions presented in Ref. [220].

When extending the excitation energy range shown in the lower panel of Fig. 4.3.6**f**, an additional low-energy maximum appears for both the RF and HSM signals at approximately 1.64 eV. This is highlighted by an arrow in Fig. 4.3.7**a**. The resonance is clearly observed in four of the six measured spots. The RF signal indicates an excitonic resonance, while the HSM maximum reflects quasi-particle–phonon coupling. Hereafter, the origin of this resonance remains speculative.

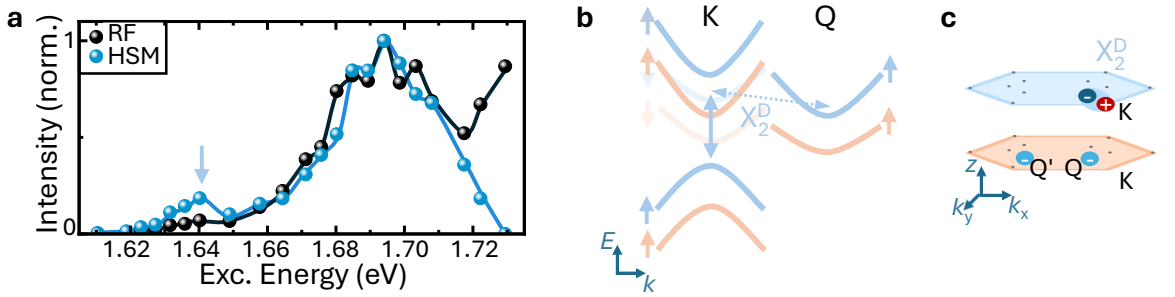

Figure 4.3.7 | a Normalized RF and HSM signal dependent on the excitation energy from the lower panel in Fig. 4.3.6**f** with an expanded x-axis. The emergent resonance is marked by an arrow. **b** Schematic of the phonon-assisted intralayer transition of the momentum-dark exciton X_2^D of the R-type WSe_2 BL. The introduced momentum by the phonon is indicated by the dashed arrow. **c** Schematic of the valley and layer configuration of the momentum-dark WSe_2 exciton in layer 2—X_2^D.

Interlayer excitons in R-type WSe_2 BLs originating from K-K transitions are symmetry-forbidden due to suppressed hole tunneling [200, 225, 389]. In contrast, excitons involving the Q valley—either intralayer or interlayer—are momentum-indirect as their center-of-mass momentum lies outside the light cone. Such excitons can nevertheless acquire weak optical activity through phonon-assisted transitions, as seen in the PL spectra above, where the absorption or emission of a phonon provides the small in-plane momentum required to couple them to light [129, 130, 197, 200, 391]. An exemplary phonon-assisted intralayer X_2^D absorption in the second layer under phonon creation is schematically depicted between the K VB and Q CB in Fig. 4.3.7**b**. The resulting quasi-particle alongside the localized electrons in the lower layer are illustrated in the BZ and layer configuration in Fig. 4.3.7**c**. This mechanism may explain the weak RF resonance and the associated HSM signal, consistent with exciton–phonon coupling due to the electron situated at the Q valley. Their charged counterparts may similarly give rise to trion–phonon coupling, as discussed earlier.

Furthermore, the nominal twist angle of 0.8° in the hBN-capped sample is expected to have a negligible effect due to atomic reconstruction. Nevertheless, as shown in Ref. [385], excitonic transitions in WSe_2 BLs are highly sensitive to the relative twist angle, and a minor contribution from twist-induced optical effects cannot be entirely ruled out.

In the PL and RC measurements shown in Fig. 4.3.6**a** of Ref. [200], as well as in the PL spectra reported in Ref. [385] for R-type WSe_2 homo-BLs, a weak, unidentified PL peak appears alongside an unexplained modulation in the RC signal around $\approx 1.64\,\text{eV}$.

So in total, multiple hints of this resonance have been observed across multiple samples and publications.

Although the exact origin of the low-energy resonance and its coupling remains elusive, monitoring the HSM offers a promising route to gain future insights into novel resonances and their hybridization. Investigating the strength of this low-energy resonance could help clarify its nature. This could be achieved by fabricating dual-gated devices of CVD-grown, high-quality R-type WSe_2 homo-BLs and studying how the HSM evolves under an external electrostatic field. An observable energy shift of the HSM resonance under such conditions would suggest a permanent out-of-plane dipole moment, consistent with the involvement of an interlayer exciton. If the Rayleigh-scattered laser light remains obtrusive to the LF Raman mode, a device with only a back gate would be promising for a doping-dependent study. Alternatively, analysis of the RF g-factor may provide additional insights into the degree of hybridization of the involved quasi-particles, as done in Section 4.3.1. In a twist-dependent study, a possible intralayer origin of this resonance could be investigated.

4.3.4 Probing hybridization of excitonic complexes in reconstructed $MoSe_2$ homobilayers

Extending the same LF Raman investigation to two intrinsically negatively doped H-type $MoSe_2$ homo-BLs demonstrates the HSM as a universal probe in investigating the hybridized character of excitonic resonances. In both samples, distinct X^0 and X^- PL peaks are observed in nonresonant PL measurements, which result in strong RF signals in the resonant LF Raman measurements. Nevertheless, a HSM is unambiguously identified at an energy of $\approx 20\,\mathrm{cm}^{-1}$. The excitation is performed at the low-energy shoulder of the X^- resonance, using an excitation energy of $E_{\mathrm{exc}} \approx 1.61\,\mathrm{eV}$ in order to minimize the RF signal. The background-subtracted HSM is shown normalized in Fig. 4.3.8**a**, where it is compared to the HSM of WSe_2 homo-BLs and the WSe_2 3L, which is investigated in the following section. The HSM energy coincides with the ISM energy of $\approx 20.0\,\mathrm{cm}^{-1}$, as measured in nonresonant Raman experiments at cryogenic temperatures, and is found to follow the polarization direction of the trion. Based on density function theory calculations, the CB minimum—and hence the location of the free electrons—is situated at the Q point [39, 41, 392–394].

This observation of the HSM signal confirms that the Q-valley electrons are hybridized across both layers, consistent with predictions for H-type MoS_2 homo-BLs [248] and analogous to the H-type WSe_2 homo-BL case [203].

In contrast, an R-type $MoSe_2$ sample (not shown) exhibits PL dominated by ML-like emission, similar to R-type WSe_2 homo-BLs. As a result, the RF signal stemming from BL contributions is not identifiable. Similarly, as the LF Raman spectra are dominated by the RF signal, no distinct LF Raman mode is detected.

Having established the applicability of the HSM as a probe of hybridized excitonic complexes in $MoSe_2$ and WSe_2 BLs, this approach is now extended to natural WSe_2 few-layers, where additional interlayer excitonic quasi-particles exist, which may couple to phonons, making them accessible to the same HSM-based investigations.

4.3.5 Probing hybridization of excitonic complexes in natural WSe_2 few-layers

Resonant LF Raman measurements are conducted on natural WSe_2 few-layer stacks, where diverse interlayer coupling mechanisms have been reported. Examples include spin-valley-locked every-other-layer excitons [202], electric-field-driven coupling [141], and other unidentified coupling mechanisms in multilayer TMDCs [108]. For this study, natural WSe_2 tri- (3L), four- (4L), and five-layer (5L) samples are investigated. The number of layers is first determined from unpolarized, nonresonant LF Raman measurements conducted at room temperature by comparing the measured ISM and IBM energies with literature values [159, 395]. Representative spectra of the respective stacks are presented in Fig. 4.3.8**b**, alongside spectra of natural WSe_2 and $MoSe_2$ homo-BLs for comparison. Notably, the IBM is nearly energetically degenerate in energy with the ISM in the 3L stack. The 5L WSe_2 shows an additional ISM (S_2) at lower frequencies, and an additional IBM (B_2) appears at higher energies starting from 4L. The absence of an additional ISM in the trilayer is notable for the following considerations [159].

An excitation energy scan of the LF Raman response across the WSe_2 resonances, as done earlier, is conducted for various layer thicknesses. A low-energy mode is identifiable only in the 3L stacks, which will be examined in detail. The corresponding spectra for the 3L WSe_2 sample are shown in Fig. 4.3.8**c**, where two asymmetric LF Raman modes are discernible at energies $E_1 \approx 15\,\mathrm{cm}^{-1}$ and $E_2 \approx 23.5\,\mathrm{cm}^{-1}$. For the lower-energy mode, an energy shift of about $2\,\mathrm{cm}^{-1}$ is observed for different excitation

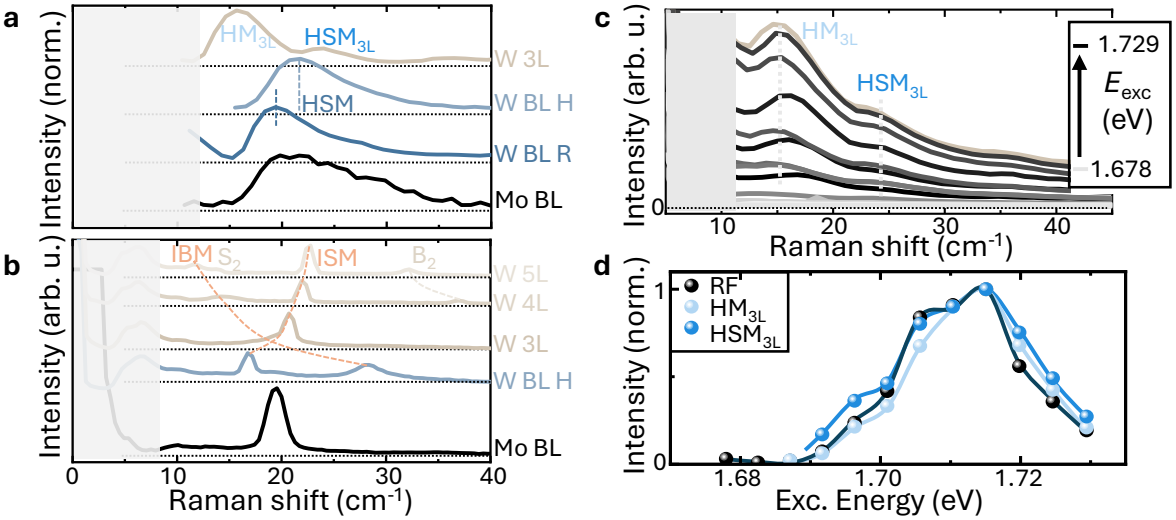

Figure 4.3.8 | a Comparison of the background-subtracted and normalized LF Raman spectra excited at trion resonance: H-type $MoSe_2$ BL spectra, R-type WSe_2 BL spectra from Fig. 4.3.6**e**, H-type WSe_2 BL spectra from Fig. 4.3.5**e**, and 3L spectra from **c**. **b** Upolarized, nonresonant LF Raman spectra measured at room temperature for natural $MoSe_2$ BL and for natural WSe_2 with 2 to 5 layers. The evolution of the ISMs and IBMs is indicated by orange dotted lines. **c** Resonant LF Raman spectra of a WSe_2 3L sample at various excitation energies E_{exc}. Gray dotted lines mark the LF Raman modes. **d** Normalized RF signal, HSM_{3L}- and HM_{3L} intensity as a function of the excitation energy. Curves are guides to the eye.

energies. Since the Raman-mode energies of all previously studied HSMs do not shift under a change in the excitation energy, the mode at $E_2 \approx 23.5\,\mathrm{cm}^{-1}$ is tentatively assigned to the HSM in the 3L, HSM_{3L}. The origin of the lower-energy peak at E_1 remains unclear, as only a single shear mode is expected in 3L stacks [159]. It is therefore labeled as an unidentified hybrid mode, HM_{3L}. The only other known LF Raman mode is the IBM, which is nearly energetically degenerate with the ISM in nonresonant experiments and appears in co-polarized detection geometry. The observed hybrid Raman modes inherit the polarization of the excited quasi-particle and, therefore, appear only in co-polarized detection geometry. As a result, distinguishing between the contributions of the shear and breathing modes based on polarization is not possible and requires supporting theoretical investigations.

The intensities of the RF signal and both hybrid modes are again analyzed as a function of the excitation energy, with the corresponding results shown in Fig. 4.3.8**d**. The hybrid modes intensities are again extracted after background subtraction. Due to the broad and asymmetric lineshape of HM_{3L}, an additional uncertainty is added to the extracted HSM_{3L} intensity, which remains within the displayed dots. Both LF

Raman-mode resonances coincide with the RF signal maximum. The appearance of an asymmetric low-energy shoulder suggests that at least two distinct coupling mechanisms contribute to the HSM intensity—and thus to the trion–phonon coupling—in the 3L system. Notably, the energies of the identified resonances closely match those of the WSe_2 H-type BL, suggesting a shared microscopic origin. The fundamentally different lattice symmetries in both systems appear to play no crucial role.

These experimental findings may serve as a foundation for theoretical investigations aimed at identifying the hybrid quasi-particles involved, and for completing and linking the BL picture to few-layer systems. To develop a comprehensive understanding of excitons and trions in those systems, it is essential to consider the absence of measurable trion–phonon coupling in stacks thicker than three layers, which may, for instance, result from doping confined to the outer layers, thereby resulting in trion hybridization at the few-layer edges.

Chapter 5

Conclusion & Outlook

In this thesis, the phononic, electronic, and excitonic properties, along with their resulting interactions, are explored in TMDC BLs, with a focus on the influence of moiré superlattices and atomic reconstruction. Using high-quality exfoliated and CVD-grown samples integrated into gate-tunable devices, PL, Raman, and absorption-based spectroscopy are combined to probe these effects and their interplay.

First, the moiré-exciton landscape of $MoSe_2$-WS_2 heterostructures is examined. High-quality R-type gated devices are characterized and compared with existing literature during these investigations. The stacking type is hereby unambiguously identified, as the TMDC edges align and the energy difference between the moiré excitons M_2 and M_3 shows excellent agreement with the literature. Homogeneous regions of the samples are located via PL area scans. Furthermore, PL and DR measurements are both used to determine the integer charge-filling factors. For charge fillings greater than two in these measurements, signatures of significant CB hybridization between $MoSe_2$ and WS_2 are identified.

The primary focus of this study lies on phonon-assisted RET processes, revealed through resonant μPL measurements. In doping-dependent excitation energy scans, three distinct resonant down-conversion processes are observed. The corresponding transitions are $M_2 \rightarrow M_1$, $M_2^- \rightarrow M_1^-$, and $M_1 \rightarrow M_1^-$, where the energy resonance between the respective excitonic states is fulfilled by the emission of one or two phonons. These processes can only occur when lateral energy transfer takes place due to the distinct charge and exciton localization within the moiré potential. The last process,

$M_1 \rightarrow M_1^-$, suggests an inter-moiré-cell energy transfer as the excitation in an uncharged cell excludes the emission of a charged quasi-particle. This interpretation is further corroborated in transition intensities analyzed as a function of gate voltage. Here, the transition maxima are observed at the expected charge fillings per moiré cell, which is seen across multiple samples.

In a temperature-dependent study of the $M_1 \rightarrow M_1^-$ process, the maximal energy transfer rate is revealed at 30 K, followed by a decrease at higher temperatures. The initial increase is interpreted as a signature of homogeneous charging behavior across the moiré lattice enabled by thermal activation. In this temperature regime, a contribution of a phonon-assisted FRET can not be excluded. However, the subsequent decline rules out Förster-type dipole–dipole interactions as the driving mechanism. The decrease in this temperature study is consistent with phonon-assisted resonant tunneling, in which increased exciton–phonon scattering reduces the energy-transfer efficiency. A tentative assignment of the observed RET process to this mechanism is, thus, conducted.

A complementary direction for future research could involve a twist-angle–dependent study of these heterostructures. As the moiré lattice constant decreases with increasing twist angle, such a study would provide spatially dependent insight into the RET processes. This could offer further evidence for the proposed mechanism of phonon-assisted resonant tunneling, and an enhancement of the inter-moiré-cell transfer rate may be achieved. Altogether, this may provide the foundation for tunable lateral transport in moiré superlattices.

A deeper understanding of the intrinsic timescales of moiré excitons could be achieved using a pump–probe differential-reflectivity technique, which would directly access exciton transfer and formation times. Moreover, the introduction of charged moiré sites in this system may inspire future theoretical studies aimed at developing a comprehensive understanding of exciton dynamics in moiré lattices with background doping. Furthermore, the transition times could be influenced by emergent local magnetic moments arising in the correlated electron lattice near $\nu = 1$ [59, 300], which might be revealed through circular-polarization-dependent measurements.

In the next part of the thesis, a brief insight into the current ongoing search for the Wigner phonon is given through resonant Raman experiments on the previously investigated R-type $MoSe_2$-WS_2 moiré system. Furthermore, due to the introduced moiré periodicity, a backfolding of the Wigner phonon branches to the Γ point may give rise to optically active moiré-Wigner phonons dependent on the charge filling per moiré cell.

In first experiments, evidence of IMBEs is observed, consistent with earlier experimental work [289]. Additionally, emergent peaks at integer and fractional charge fillings are observed, which are indicative of Wigner-phonon modes. It becomes evident that high-quality samples are crucial for unambiguously identifying the origins of individual modes, as a reduction of the prominent RF signal is required. Future experimental ideas involve the chiral nature of Wigner phonons, which may be observable in future resonance- and helicity-resolved PL/Raman studies.

In twisted $MoSe_2$-WSe_2 heterostructures, the emergence of moiré phonons from both constituent materials due to acoustic phonon branch backfolding to the Γ point is revealed through a LF Raman study. This observation complements earlier insights into moiré phonons in homo-BLs, consisting of $MoSe_2$, MoS_2, or WSe_2 [210, 211, 346]. A significant advantage of these findings is their applicability in a hyperspectral imaging technique. This enables a non-invasive analysis of local relative twist angles and is not deterred by an hBN encapsulation, which enhances the overall sample quality. In general, the ability to detect local twist variations is a necessity in optical experiments and is highly relevant for the interpretation of various studies. A prime example is the broadening of RILS peaks in IMBEs, which is reported in Ref. [289].

In the second part of this thesis, the influence of reconstructed lattices on excitonic and phononic properties is investigated. Resonant LF Raman studies on $MoSe_2$-WSe_2 hetero-BLs reveal an asymmetric LF Raman mode, which is attributed to emergent trion–phonon coupling. This mode appears only under resonant excitation with the intralayer trion states of the two constituent materials. In those, the additionally bound electron is situated at the Q valley and hybridized over both layers, and in turn enables a coupling to the ISM. This interpretation is supported by accompanying theoretical calculations. Further evidence for the hybrid character of the trion is provided by a magneto-PL study. The g_{eff}-factor of $g_{\text{eff}} = -7.7 \pm 2$ is extracted in an R-type hetero-BL, which significantly exceeds the typical intralayer value of approximately -4.

This trion–phonon coupling can be selectively activated or suppressed in electrostatically-doped hetero-BL devices by tuning the system into or out of charge neutrality, which is achieved in three separate devices. One sample exhibits an unexpected trion-phonon coupling in the positive doping regime, requiring further statistics for a final conclusion.

The emergence of a LF Raman mode provides important insights into electron hybridization and their distribution in reciprocal space, specifically whether they are situated at the Q point. The HSM as a probing tool in LF Raman spectroscopy is applied

to both H-type and R-type WSe_2 homo-BLs. In these systems, the bright intralayer excitonic transitions are analyzed, revealing hybridized electrons for both stacking configurations. Notably, this observation of hybridization is a novel insight into the R-type stacking, as the spatial inversion symmetry breaking would result in the localization of carriers within a single layer. Another surprising result in the R-type homo-BL is the identification of a low-energy resonance at approximately 1.64 eV. The detected RF signal is hereby accompanied by the emergence of a HSM. A phonon-assisted second-order absorption in both neutral and negative doping regimes is tentatively discussed as a possible, responsible excitonic resonance. Confirming the origin of this resonance is crucial for a comprehensive picture of the electronic and excitonic landscape in such a fundamental BL system.

Future doping-dependent studies, combined with investigations under externally applied electric and magnetic fields, appear highly promising to understand the origin of this resonance, as the interlayer character and degree of hybridization of the involved quasi-particle can be probed. In this context, sample fabrication using high-quality CVD-grown BLs represents a first step to ensure homogeneous interlayer contact and experimental reproducibility. These experimental efforts will hopefully stimulate complementary theoretical work aimed at unraveling the microscopic picture behind the observed experimental signatures.

In related studies on H-type $MoSe_2$ BLs, similar trion-phonon coupling is observed, strongly suggesting that electrons are hybridized at the Q valley across both layers, as seen in WSe_2 BLs. This finding aligns with theoretical predictions made for MoS_2 BLs in Ref. [248] and further confirms the LF HSM signal to serve as a universal probe in investigating the hybridized character of excitonic resonances.

Finally, the resonant LF Raman measurements are expanded to natural WSe_2 few-layer systems. Notably, the HSM is identified only in 3L samples. Furthermore, an additional, unidentified second LF Raman peak is observed. As the two modes require trion-phonon coupling, they clearly indicate the hybridized character of electrons at the Q valley. One possible explanation for the second LF mode is that it arises from coupling between the trion and the IBM. This remains speculative, as polarization-resolved measurements cannot distinguish between these contributions.

Taken together, these results provide key insights into how the TMDC BL lattice shapes the excitonic and phononic landscapes and defines their interplay. Central outcomes include the identification of phonon-assisted resonant tunneling, which governs exciton

dynamics in moiré superlattices, and the discovery of a universal trion–phonon coupling that serves as a probe of the degree of excitonic hybridization in various 2D vdW homo-BLs and heterostructures.

An essential step towards uncovering novel physical phenomena lies in the fabrication of high-quality samples via CVD growth. With the current structures, time-resolved pump-probe spectroscopy and twist-angle–dependent studies promise further insights into the fundamental physical properties and mechanisms in vdW BL systems.

These new insights, gained in straightforward systems within a single thesis, highlight the potential for future innovations when the scientific community pulls together towards a common goal.

Bibliography

[1] A. Tonk and S. Goyal. *A Literature Review on Leakage and Power Reduction Techniques in CMOS VLSI Design*. International Journal on Recent and Innovation Trends in Computing and Communication **3**, 554–558 (2015).

[2] P. Verma, A. K. Sharma, V. S. Pandey, A. Noor, and A. Tanwar. *Estimation of leakage power and delay in CMOS circuits using parametric variation*. Perspectives in Science **8**, 760–763 (2016).

[3] B. King. *Power Tips: in the Quest for No Standby Power, Where Do We Declare Victory?* (2023).

[4] R. Italia. *An Analysis of Miniaturization in Consumer Electronics: A Technological Overview*. International Journal on Science and Technology (IJSAT) IJSAT24041258 **15** (2024).

[5] V. Gallego and D. R. Insua. *Current Advances in Neural Networks*. Annual Review of Statistics and Its Application **9**, 197–222 (2022).

[6] F. Shao and Z. Shen. *How can artificial neural networks approximate the brain?* Frontiers in Psychology **13** (2023).

[7] I. D. Mienye, T. G. Swart, and G. Obaido. *Recurrent Neural Networks: A Comprehensive Review of Architectures, Variants, and Applications*. Information **15**, 517 (2024).

[8] P. M. Kogge. *Function-based computing and parallelism: A review*. Parallel Computing **2**, 243–253 (1985).

[9] D. Efnusheva, A. Cholakoska, and A. Tentov. *A Survey of Different Approaches for Overcoming the Processor - Memory Bottleneck*. International Journal of Computer Science and Information Technology **9**, 151–163 (2017).

[10] D. Fakhry, M. Abdelsalam, M. W. El-Kharashi, and M. Safar. *A review on computational storage devices and near memory computing for high performance applications*. Memories - Materials, Devices, Circuits and Systems **4**, 100051 (2023).

[11] A. Acín, I. Bloch, H. Buhrman, T. Calarco, C. Eichler, J. Eisert, D. Esteve, N. Gisin, S. J. Glaser, F. Jelezko, S. Kuhr, M. Lewenstein, M. F. Riedel, P. O. Schmidt, R. Thew, A. Wallraff, I. Walmsley, and F. K. Wilhelm. *The quantum technologies roadmap: a European community view.* New Journal of Physics **20**, 080201 (2018).

[12] N. S, H. Singh, and A. U. N. *An extensive review on quantum computers.* Advances in Engineering Software **174**, 103337 (2022).

[13] E. Chae, J. Choi, and J. Kim. *An elementary review on basic principles and developments of qubits for quantum computing.* Nano Convergence **11**, 11 (2024).

[14] J. W. Lim. *Polymer Materials for Optoelectronics and Energy Applications.* Materials **17**, 3698 (2024).

[15] H. Zhang, J. Li, C. Yang, and X. Guo. *Single-Molecule Functional Chips: Unveiling the Full Potential of Molecular Electronics and Optoelectronics.* Accounts of Materials Research **5**, 971–986 (2024).

[16] G. A. Nowsherwan, Q. Ali, U. F. Ali, M. Ahmad, M. Khan, and S. S. Hussain. *Advances in Organic Materials for Next-Generation Optoelectronics: Potential and Challenges.* Organics **5**, 520–560 (2024).

[17] M. M. Sabzehmeidani, S. Gafari, S. jamali, and M. Kazemzad. *Concepts, fabrication and applications of MOF thin films in optoelectronics: A review.* Applied Materials Today **38**, 102153 (2024).

[18] S. T. Ha, Q. Li, J. K. W. Yang, H. V. Demir, M. L. Brongersma, and A. I. Kuznetsov. *Optoelectronic metadevices.* Science **386** (2024).

[19] I. Shahbaz, M. Tahir, L. Li, and Y. Song. *Advancements in 2D transition metal dichalcogenides (TMDs) inks for printed optoelectronics: A comprehensive review.* Materials Today **77**, 142–184 (2024).

[20] W. Ahmad, A. Abbas, U. Younis, J. Zhang, S. H. Aleithan, and Z. Wang. *Advancements in Optoelectronics: Harnessing the Potential of 2D Violet Phosphorus.* Advanced Functional Materials **34** (2024).

[21] P.-F. Gan, Q.-F. Yang, R.-Q. Sun, C.-C. Pan, S.-Y. Yu, and Z.-B. Tan. *Single-molecule optoelectronic devices: exciton effect and spectroscopy characterization.* Rare Metals (2025).

[22] S. Bhatti, R. Sbiaa, A. Hirohata, H. Ohno, S. Fukami, and S. Piramanayagam. *Spintronics based random access memory: a review.* Materials Today **20**, 530–548 (2017).

[23] V. D. Nguyen, S. Rao, K. Wostyn, and S. Couet. *Recent progress in spin-orbit torque magnetic random-access memory.* npj Spintronics **2**, 48 (2024).

[24] K. Cai, T. Jin, and W. S. Lew. *Spin-based magnetic random-access memory for high-performance computing.* National Science Review **11** (2024).

[25] K. S. Novoselov, A. K. Geim, S. V. Morozov, D. Jiang, Y. Zhang, S. V. Dubonos, I. V. Grigorieva, and A. A. Firsov. *Electric Field Effect in Atomically Thin Carbon Films.* Science **306**, 666–669 (2004).

[26] A. Geim and K. Novoselov. *Nobel Prize in Physics 2010 'for groundbreaking experiments regarding the two-dimensional material graphene'*. Tech. rep. 2010.

[27] O. Klein. *Die Reflexion von Elektronen an einem Potentialsprung nach der relativistischen Dynamik von Dirac*. Zeitschrift für Physik **53**, 157–165 (1929).

[28] W. Zhu, V. Perebeinos, M. Freitag, and P. Avouris. *Carrier scattering, mobilities, and electrostatic potential in monolayer, bilayer, and trilayer graphene*. Physical Review B **80**, 235402 (2009).

[29] A. H. C. Neto, F. Guinea, N. M. Peres, K. S. Novoselov, and A. K. Geim. *The electronic properties of graphene*. Reviews of Modern Physics **81**, 109–162 (2009).

[30] S. D. Sarma, S. Adam, E. H. Hwang, and E. Rossi. *Electronic transport in two-dimensional graphene*. Reviews of Modern Physics **83**, 407–470 (2011).

[31] M. I. Katsnelson, K. S. Novoselov, and A. K. Geim. *Chiral tunnelling and the Klein paradox in graphene*. Nature Physics **2**, 620–625 (2006).

[32] A. F. Young and P. Kim. *Quantum interference and Klein tunnelling in graphene heterojunctions*. Nature Physics **5**, 222–226 (2009).

[33] V. P. Gusynin and S. G. Sharapov. *Unconventional integer quantum hall effect in graphene*. Physical Review Letters **95** (2005).

[34] Y. Zhang, Y.-W. Tan, H. L. Stormer, and P. Kim. *Experimental observation of the quantum Hall effect and Berry's phase in graphene*. Nature **438**, 201–204 (2005).

[35] K. S. Novoselov, A. K. Geim, S. V. Morozov, D. Jiang, M. I. Katsnelson, I. V. Grigorieva, S. V. Dubonos, and A. A. Firsov. *Two-dimensional gas of massless Dirac fermions in graphene*. Nature **438**, 197–200 (2005).

[36] A. K. Geim and K. S. Novoselov. *The rise of graphene*. Nature Materials **6**, 183–191 (2007).

[37] X. Du, I. Skachko, A. Barker, and E. Y. Andrei. *Approaching ballistic transport in suspended graphene*. Nature Nanotechnology **3**, 491–495 (2008).

[38] K. I. Bolotin, K. J. Sikes, Z. Jiang, M. Klima, G. Fudenberg, J. Hone, P. Kim, and H. L. Stormer. *Ultrahigh electron mobility in suspended graphene*. Solid State Communications **146**, 351–355 (2008).

[39] A. Splendiani, L. Sun, Y. Zhang, T. Li, J. Kim, C. Y. Chim, G. Galli, and F. Wang. *Emerging photoluminescence in monolayer MoS_2*. Nano Letters **10**, 1271–1275 (2010).

[40] K. F. Mak, C. Lee, J. Hone, J. Shan, and T. F. Heinz. *Atomically Thin MoS_2: A New Direct-Gap Semiconductor*. Physical Review Letters **105**, 136805 (2010).

[41] T. Cheiwchanchamnangij and W. R. L. Lambrecht. *Quasiparticle band structure calculation of monolayer, bilayer, and bulk MoS_2*. Physical Review B **85**, 205302 (2012).

[42] A. Ramasubramaniam. *Large excitonic effects in monolayers of molybdenum and tungsten dichalcogenides*. Physical Review B **86**, 115409 (2012).

[43] D. Y. Qiu, F. H. D. Jornada, and S. G. Louie. *Optical spectrum of MoS_2: Many-body effects and diversity of exciton states*. Physical Review Letters **111**, 216805 (2013).

[44] A. Chernikov, T. C. Berkelbach, H. M. Hill, A. Rigosi, Y. Li, B. Aslan, D. R. Reichman, M. S. Hybertsen, and T. F. Heinz. *Exciton Binding Energy and Nonhydrogenic Rydberg Series in Monolayer WS_2*. Physical Review Letters **113**, 076802 (2014).

[45] K. He, N. Kumar, L. Zhao, Z. Wang, K. F. Mak, H. Zhao, and J. Shan. *Tightly bound excitons in monolayer WSe_2*. Physical Review Letters **113**, 026803 (2014).

[46] H. Zeng, J. Dai, W. Yao, D. Xiao, and X. Cui. *Valley polarization in MoS_2 monolayers by optical pumping*. Nature Nanotechnology **7**, 490–493 (2012).

[47] K. F. Mak, K. He, J. Shan, and T. F. Heinz. *Control of valley polarization in monolayer MoS_2 by optical helicity*. Nature Nanotechnology **7**, 494–498 (2012).

[48] T. Cao, G. Wang, W. Han, H. Ye, C. Zhu, J. Shi, Q. Niu, P. Tan, E. Wang, B. Liu, and J. Feng. *Valley-selective circular dichroism of monolayer molybdenum disulphide*. Nature Communications **3**, 887 (2012).

[49] H. Fang, C. Battaglia, C. Carraro, S. Nemsak, B. Ozdol, J. S. Kang, H. A. Bechtel, S. B. Desai, F. Kronast, A. A. Unal, G. Conti, C. Conlon, G. K. Palsson, M. C. Martin, A. M. Minor, C. S. Fadley, E. Yablonovitch, R. Maboudian, and A. Javey. *Strong interlayer coupling in van der Waals heterostructures built from single-layer chalcogenides*. Proceedings of the National Academy of Sciences **111**, 6198–6202 (2014).

[50] P. Rivera, J. R. Schaibley, A. M. Jones, J. S. Ross, S. Wu, G. Aivazian, P. Klement, K. Seyler, G. Clark, N. J. Ghimire, J. Yan, D. G. Mandrus, W. Yao, and X. Xu. *Observation of long-lived interlayer excitons in monolayer $MoSe_2$–WSe_2 heterostructures*. Nature Communications **6**, 6242 (2015).

[51] P. Nagler, M. V. Ballottin, A. A. Mitioglu, F. Mooshammer, N. Paradiso, C. Strunk, R. Huber, A. Chernikov, P. C. M. Christianen, C. Schüller, and T. Korn. *Giant magnetic splitting inducing near-unity valley polarization in van der Waals heterostructures*. Nature Communications **8**, 1551 (2017).

[52] B. Miller, A. Steinhoff, B. Pano, J. Klein, F. Jahnke, A. Holleitner, and U. Wurstbauer. *Long-Lived Direct and Indirect Interlayer Excitons in van der Waals Heterostructures*. Nano Letters **17**, 5229–5237 (2017).

[53] C. Jin, E. C. Regan, A. Yan, M. I. B. Utama, D. Wang, S. Zhao, Y. Qin, S. Yang, Z. Zheng, S. Shi, K. Watanabe, T. Taniguchi, S. Tongay, A. Zettl, and F. Wang. *Observation of moiré excitons in WSe_2/WS_2 heterostructure superlattices*. Nature **567**, 76–80 (2019).

[54] H. Yu, G.-B. Liu, J. Tang, X. Xu, and W. Yao. *Moiré excitons: From programmable quantum emitter arrays to spin-orbit–coupled artificial lattices*. Science Advances **3**, e1701696 (2017).

[55] L. Yuan, B. Zheng, J. Kunstmann, T. Brumme, A. B. Kuc, C. Ma, S. Deng, D. Blach, A. Pan, and L. Huang. *Twist-angle-dependent interlayer exciton diffusion in WS_2–WSe_2 heterobilayers*. Nature Materials **19**, 617–623 (2020).

[56] L. Zhang, Z. Zhang, F. Wu, D. Wang, R. Gogna, S. Hou, K. Watanabe, T. Taniguchi, K. Kulkarni, T. Kuo, S. R. Forrest, and H. Deng. *Twist-angle dependence of moiré excitons in $WS_2/MoSe_2$ heterobilayers*. Nature Communications **11**, 5888 (2020).

[57] X. Wang, J. Zhu, K. L. Seyler, P. Rivera, H. Zheng, Y. Wang, M. He, T. Taniguchi, K. Watanabe, J. Yan, D. G. Mandrus, D. R. Gamelin, W. Yao, and X. Xu. *Moiré trions in $MoSe_2/WSe_2$ heterobilayers*. Nature Nanotechnology **16**, 1208–1213 (2021).

[58] Y. G. Gobato, C. S. de Brito, A. Chaves, M. A. Prosnikov, T. Woźniak, S. Guo, I. D. Barcelos, M. V. Milošević, F. Withers, and P. C. M. Christianen. *Distinctive g-Factor of Moiré-Confined Excitons in van der Waals Heterostructures*. Nano Letters **22**, 8641–8646 (2022).

[59] L. Ciorciaro, T. Smoleński, I. Morera, N. Kiper, S. Hiestand, M. Kroner, Y. Zhang, K. Watanabe, T. Taniguchi, E. Demler, and A. İmamoğlu. *Kinetic magnetism in triangular moiré materials*. Nature **623**, 509–513 (2023).

[60] B. Polovnikov, J. Scherzer, S. Misra, X. Huang, C. Mohl, Z. Li, J. Göser, J. Förste, I. Bilgin, K. Watanabe, T. Taniguchi, A. Högele, and A. S. Baimuratov. *Field-Induced Hybridization of Moiré Excitons in $MoSe_2/WS_2$ Heterobilayers*. Physical Review Letters **132**, 076902 (2024).

[61] B. Polovnikov, J. Scherzer, S. Misra, H. Schlömer, J. Trapp, X. Huang, C. Mohl, Z. Li, J. Göser, J. Förste, I. Bilgin, K. Watanabe, T. Taniguchi, A. Bohrdt, F. Grusdt, A. S. Baimuratov, and A. Högele. *Implementation of the bilayer Hubbard model in a moiré heterostructure*. arXiv:2404.05494v1 (2024).

[62] B. Padhi, C. Setty, and P. W. Phillips. *Doped Twisted Bilayer Graphene near Magic Angles: Proximity to Wigner Crystallization, Not Mott Insulation*. Nano Letters **18**, 6175–6180 (2018).

[63] Y.-C. Tsui, M. He, Y. Hu, E. Lake, T. Wang, K. Watanabe, T. Taniguchi, M. P. Zaletel, and A. Yazdani. *Direct observation of a magnetic-field-induced Wigner crystal*. Nature **628**, 287–292 (2024).

[64] D. Erkensten, S. Brem, R. Perea-Causin, and E. Malic. *Stability of Wigner crystals and Mott insulators in twisted moiré structures*. Physical Review B **110**, 155132 (2024).

[65] Y. Hu, Y. C. Tsui, M. He, U. Kamber, T. Wang, A. S. Mohammadi, K. Watanabe, T. Taniguchi, Z. Papić, M. P. Zaletel, and A. Yazdani. *High-resolution tunnelling spectroscopy of fractional quantum Hall states*. Nature Physics **21**, 716–723 (2025).

[66] L. Wang, E.-M. Shih, A. Ghiotto, L. Xian, D. A. Rhodes, C. Tan, M. Claassen, D. M. Kennes, Y. Bai, B. Kim, K. Watanabe, T. Taniguchi, X. Zhu, J. Hone, A. Rubio, A. N. Pasupathy, and C. R. Dean. *Correlated electronic phases in twisted bilayer transition metal dichalcogenides*. Nature Materials **19**, 861–866 (2020).

[67] Y. Xu, S. Liu, D. A. Rhodes, K. Watanabe, T. Taniguchi, J. Hone, V. Elser, K. F. Mak, and J. Shan. *Correlated insulating states at fractional fillings of moiré superlattices*. Nature **587**, 214–218 (2020).

[68] B. Padhi, R. Chitra, and P. W. Phillips. *Generalized Wigner crystallization in moiré materials*. Physical Review B **103**, 125146 (2021).

[69] H. Li, S. Li, E. C. Regan, D. Wang, W. Zhao, S. Kahn, K. Yumigeta, M. Blei, T. Taniguchi, K. Watanabe, S. Tongay, A. Zettl, M. F. Crommie, and F. Wang. *Imaging two-dimensional generalized Wigner crystals*. Nature **597**, 650–654 (2021).

[70] Y. Zhou, J. Sung, E. Brutschea, I. Esterlis, Y. Wang, G. Scuri, R. J. Gelly, H. Heo, T. Taniguchi, K. Watanabe, G. Zaránd, M. D. Lukin, P. Kim, E. Demler, and H. Park. *Bilayer Wigner crystals in a transition metal dichalcogenide heterostructure*. Nature **595**, 48–52 (2021).

[71] Y. Shimazaki, C. Kuhlenkamp, I. Schwartz, T. Smoleński, K. Watanabe, T. Taniguchi, M. Kroner, R. Schmidt, M. Knap, and A. Imamoğlu. *Optical Signatures of Periodic Charge Distribution in a Mott-like Correlated Insulator State*. Physical Review X **11**, 021027 (2021).

[72] Y. Tang, J. Gu, S. Liu, K. Watanabe, T. Taniguchi, J. C. Hone, K. F. Mak, and J. Shan. *Dielectric catastrophe at the Wigner-Mott transition in a moiré superlattice*. Nature Communications **13**, 4271 (2022).

[73] H. Park, J. Cai, E. Anderson, Y. Zhang, J. Zhu, X. Liu, C. Wang, W. Holtzmann, C. Hu, Z. Liu, T. Taniguchi, K. Watanabe, J. H. Chu, T. Cao, L. Fu, W. Yao, C. Z. Chang, D. Cobden, D. Xiao, and X. Xu. *Observation of fractionally quantized anomalous Hall effect*. Nature **622**, 74–79 (2023).

[74] J. Cai, E. Anderson, C. Wang, X. Zhang, X. Liu, W. Holtzmann, Y. Zhang, F. Fan, T. Taniguchi, K. Watanabe, Y. Ran, T. Cao, L. Fu, D. Xiao, W. Yao, and X. Xu. *Signatures of fractional quantum anomalous Hall states in twisted $MoTe_2$*. Nature **622**, 63–68 (2023).

[75] Y. Zeng, Z. Xia, K. Kang, J. Zhu, P. Knüppel, C. Vaswani, K. Watanabe, T. Taniguchi, K. F. Mak, and J. Shan. *Thermodynamic evidence of fractional Chern insulator in moiré $MoTe_2$*. Nature **622**, 69–73 (2023).

[76] F. Xu, Z. Sun, T. Jia, C. Liu, C. Xu, C. Li, Y. Gu, K. Watanabe, T. Taniguchi, B. Tong, J. Jia, Z. Shi, S. Jiang, Y. Zhang, X. Liu, and T. Li. *Observation of Integer and Fractional Quantum Anomalous Hall Effects in Twisted Bilayer $MoTe_2$*. Physical Review X **13**, 031037 (2023).

[77] E. Anderson, F.-R. Fan, J. Cai, W. Holtzmann, T. Taniguchi, K. Watanabe, D. Xiao, W. Yao, and X. Xu. *Programming correlated magnetic states with gate-controlled moiré geometry*. Science **381**, 325–330 (2023).

[78] R. Bistritzer and A. H. MacDonald. *Moiré bands in twisted double-layer graphene*. Proceedings of the National Academy of Sciences **108**, 12233–12237 (2011).

[79] Y. Cao, V. Fatemi, S. Fang, K. Watanabe, T. Taniguchi, E. Kaxiras, and P. Jarillo-Herrero. *Unconventional superconductivity in magic-angle graphene superlattices*. Nature **556**, 43–50 (2018).

[80] Y. Cao, V. Fatemi, A. Demir, S. Fang, S. L. Tomarken, J. Y. Luo, J. D. Sanchez-Yamagishi, K. Watanabe, T. Taniguchi, E. Kaxiras, R. C. Ashoori, and P. Jarillo-Herrero. *Correlated insulator behaviour at half-filling in magic-angle graphene superlattices*. Nature **556**, 80–84 (2018).

[81] X. Lu, P. Stepanov, W. Yang, M. Xie, M. A. Aamir, I. Das, C. Urgell, K. Watanabe, T. Taniguchi, G. Zhang, A. Bachtold, A. H. Macdonald, and D. K. Efetov. *Superconductors, orbital magnets and correlated states in magic-angle bilayer graphene*. Nature **574**, 653 (2019).

[82] W. B. Shockley, J. Bardeen, and W. H. Brattain. *Nobel Prize in Physics 1956 'for their researches on semiconductors and their discovery of the transistor effect'*.

[83] W. F. Brinkman, D. E. Haggan, and W. W. Troutman. *A History of the Invention of the Transistor and Where It Will Lead Us*. IEEE Journal of Solid-State Circuits **32** (1997).

[84] R. F. Frindt and A. D. Yoffe. *Physical Properties of Layer Structures: Optical Properties and Photoconductivity of Thin Crystals of Molybdenum Disulphide*. Proceedings of the Royal Society of London **273**, 1352 (1963).

[85] J. A. Wilson and A. D. Yoffe. *The transition metal dichalcogenides discussion and interpretation of the observed optical, electrical and structural properties*. Advances in Physics **18**, 193–335 (1969).

[86] R. A. Bromley, R. B. Murray, and A. D. Yoffe. *The band structures of some transition metal dichalcogenides. III. Group VIA: trigonal prism materials*. Journal of Physics C: Solid State Physics **5**, 759–778 (1972).

[87] R. G. Dickinson and L. Pauling. *The Crystal Structure of Molybdenite*. Journal of the American Chemical Society **45**, 1466–1471 (1923).

[88] K. S. Novoselov, D. Jiang, F. Schedin, T. J. Booth, V. V. Khotkevich, S. V. Morozov, and A. K. Geim. *Two-dimensional atomic crystals*. PNAS **102**, 10451–10453 (2005).

[89] L. F. Mattheiss. *Band Structures of Transition-Metal-Dichalcogenide Layer Compounds*. Physical Review B **8**, 3719–3740 (1973).

[90] R. Coehoorn, C. Haas, J. Dijkstra, C. J. F. Flipse, R. A. D. Groot, and A. Wold. *Electronic structure of $MoSe_2$, MoS_2, and WSe_2. I. Band-structure calculations and photoelectron spectroscopy*. Physical Review B **35**, 12 (1987).

[91] D. Voß, P. Krüger, A. Mazur, and J. Pollmann. *Atomic and electronic structure of WSe_2 from ab initio theory: Bulk crystal and thin film systems*. Physical Review B **60**, 14311–14317 (1999).

[92] S. Lebègue and O. Eriksson. *Electronic structure of two-dimensional crystals from ab initio theory*. Physical Review B **79**, 115409 (2009).

[93] A. Kuc, N. Zibouche, and T. Heine. *Influence of quantum confinement on the electronic structure of the transition metal sulfide TS_2*. Physical Review B **83**, 245213 (2011).

[94] E. S. Kadantsev and P. Hawrylak. *Electronic structure of a single MoS_2 monolayer*. Solid State Communications **152**, 909–913 (2012).

[95] Z. Y. Zhu, Y. C. Cheng, and U. Schwingenschlögl. *Giant spin-orbit-induced spin splitting in two-dimensional transition-metal dichalcogenide semiconductors*. Physical Review B **84**, 153402 (2011).

[96] D. Xiao, G.-B. Liu, W. Feng, X. Xu, and W. Yao. *Coupled Spin and Valley Physics in Monolayers of MoS_2 and Other Group-VI Dichalcogenides*. Physical Review Letters **108**, 196802 (2012).

[97] K. Kośmider, J. W. González, and J. Fernández-Rossier. *Large spin splitting in the conduction band of transition metal dichalcogenide monolayers*. Physical Review B **88**, 245436 (2013).

[98] A. Kormányos, V. Zólyomi, N. D. Drummond, and G. Burkard. *Spin-Orbit Coupling, Quantum Dots, and Qubits in Monolayer Transition Metal Dichalcogenides*. Physical Review X **4**, 011034 (2014).

[99] A. Kormányos, G. Burkard, M. Gmitra, J. Fabian, V. Zólyomi, N. D. Drummond, and V. Fal'ko. *Corrigendum: k.p theory for two-dimensional transition metal dichalcogenide semiconductors*. 2D Materials **2**, 049501 (2015).

[100] Y. Zhang, T.-R. Chang, B. Zhou, Y.-T. Cui, H. Yan, Z. Liu, F. Schmitt, J. Lee, R. Moore, Y. Chen, H. Lin, H.-T. Jeng, S.-K. Mo, Z. Hussain, A. Bansil, and Z.-X. Shen. *Direct observation of the transition from indirect to direct bandgap in atomically thin epitaxial $MoSe_2$*. Nature Nanotechnology **9**, 111–115 (2014).

[101] W. Yao, D. Xiao, and Q. Niu. *Valley-dependent optoelectronics from inversion symmetry breaking*. Physical Review B **77**, 235406 (2008).

[102] A. M. Jones, H. Yu, N. J. Ghimire, S. Wu, G. Aivazian, J. S. Ross, B. Zhao, J. Yan, D. G. Mandrus, D. Xiao, W. Yao, and X. Xu. *Optical generation of excitonic valley coherence in monolayer WSe_2*. Nature Nanotechnology **8**, 634–638 (2013).

[103] A. Molina-Sánchez, D. Sangalli, K. Hummer, A. Marini, and L. Wirtz. *Effect of spin-orbit interaction on the optical spectra of single-layer, double-layer, and bulk MoS_2*. Physical Review B **88**, 045412 (2013).

[104] Z. Gong, G. B. Liu, H. Yu, D. Xiao, X. Cui, X. Xu, and W. Yao. *Magnetoelectric effects and valley-controlled spin quantum gates in transition metal dichalcogenide bilayers*. Nature Communications **4** (2013).

[105] A. M. Jones, H. Yu, J. S. Ross, P. Klement, N. J. Ghimire, J. Yan, D. G. Mandrus, W. Yao, and X. Xu. *Spin–layer locking effects in optical orientation of exciton spin in bilayer WSe_2*. Nature Physics **10**, 130–134 (2014).

[106] C. Jiang, F. Liu, J. Cuadra, Z. Huang, K. Li, A. Rasmita, A. Srivastava, Z. Liu, and W.-B. Gao. *Zeeman splitting via spin-valley-layer coupling in bilayer $MoTe_2$*. Nature Communications **8**, 802 (2017).

[107] A. Arora, M. Koperski, A. Slobodeniuk, K. Nogajewski, R. Schmidt, R. Schneider, M. R. Molas, S. M. de Vasconcellos, R. Bratschitsch, and M. Potemski. *Zeeman spectroscopy of excitons and hybridization of electronic states in few-layer WSe_2, $MoSe_2$ and $MoTe_2$*. 2D Materials **6**, 015010 (2018).

[108] S. Raiber, P. E. F. Junior, D. Falter, S. Feldl, P. Marzena, K. Watanabe, T. Taniguchi, J. Fabian, and C. Schüller. *Ultrafast pseudospin quantum beats in multilayer WSe_2 and $MoSe_2$*. Nature Communications **13** (2022).

[109] G.-B. Liu, W.-Y. Shan, Y. Yao, W. Yao, and D. Xiao. *Three-band tight-binding model for monolayers of group-VIB transition metal dichalcogenides*. Physical Review B **88**, 085433 (2013).

[110] M. M. Glazov, T. Amand, X. Marie, D. Lagarde, L. Bouet, and B. Urbaszek. *Exciton fine structure and spin decoherence in monolayers of transition metal dichalcogenides*. Physical Review B **89**, 201302 (2014).

[111] G. Wang, A. Chernikov, M. M. Glazov, T. F. Heinz, X. Marie, T. Amand, and B. Urbaszek. *Colloquium: Excitons in atomically thin transition metal dichalcogenides*. Reviews of Modern Physics **90**, 021001 (2018).

[112] J. Frenkel. *On the Transformation of light into Heat in Solids. I*. Physical Review **37**, 17–44 (1931).

[113] G. Plechinger, P. Nagler, A. Arora, A. G. D. Águila, M. V. Ballottin, T. Frank, P. Steinleitner, M. Gmitra, J. Fabian, P. C. Christianen, R. Bratschitsch, C. Schüller, and T. Korn. *Excitonic Valley Effects in Monolayer WS_2 under High Magnetic Fields*. Nano Letters **16**, 7899–7904 (2016).

[114] A. V. Stier, K. M. McCreary, B. T. Jonker, J. Kono, and S. A. Crooker. *Exciton diamagnetic shifts and valley Zeeman effects in monolayer WS_2 and MoS_2 to 65 Tesla*. Nature Communications **7**, 10643 (2016).

[115] G. H. Wannier. *The Structure of Electronic Excitation Levels in Insulating Crystals*. Physical Review **52**, 191–197 (1937).

[116] H. Kalt and C. F. Klingshirn. *Semiconductor Optics 1*. Springer International Publishing, 2019.

[117] R. Gross and A. Marx. *Festkörperphysik*. OLDENBOURG WISSENSCHAFTSVERLAG, 2014.

[118] G. Wang, M. M. Glazov, C. Robert, T. Amand, X. Marie, and B. Urbaszek. *Double Resonant Raman Scattering and Valley Coherence Generation in Monolayer WSe_2*. Physical Review Letters **115**, 117401 (2015).

[119] A. Raja, L. Waldecker, J. Zipfel, Y. Cho, S. Brem, J. D. Ziegler, M. Kulig, T. Taniguchi, K. Watanabe, E. Malic, T. F. Heinz, T. C. Berkelbach, and A. Chernikov. *Dielectric disorder in two-dimensional materials*. Nature Nanotechnology **14**, 832–837 (2019).

[120] F. Cadiz, E. Courtade, C. Robert, G. Wang, Y. Shen, H. Cai, T. Taniguchi, K. Watanabe, H. Carrere, D. Lagarde, M. Manca, T. Amand, P. Renucci, S. Tongay, X. Marie, and B. Urbaszek. *Excitonic linewidth approaching the homogeneous limit in MoS_2-based van der Waals heterostructures*. Physical Review X **7**, 021026 (2017).

[121] C. Jin, J. Kim, J. Suh, Z. Shi, B. Chen, X. Fan, M. Kam, K. Watanabe, T. Taniguchi, S. Tongay, A. Zettl, J. Wu, and F. Wang. *Interlayer electron-phonon coupling in WSe_2/hBN heterostructures*. Nature Physics **13**, 127–131 (2017).

[122] Z. Wang, L. Zhao, K. F. Mak, and J. Shan. *Probing the Spin-Polarized Electronic Band Structure in Monolayer Transition Metal Dichalcogenides by Optical Spectroscopy*. Nano Letters **17**, 740–746 (2017).

[123] Z. Li, T. Wang, Z. Lu, C. Jin, Y. Chen, Y. Meng, Z. Lian, T. Taniguchi, K. Watanabe, S. Zhang, D. Smirnov, and S. F. Shi. *Revealing the biexciton and trion-exciton complexes in BN encapsulated WSe_2*. Nature Communications **9**, 3719 (2018).

[124] J. Holler, L. Bauriedl, T. Korn, A. Seitz, F. Özyigit, M. Eichinger, C. Schüller, K. Watanabe, T. Taniguchi, C. Strunk, and N. Paradiso. *Air tightness of hBN encapsulation and its impact on Raman spectroscopy of van der Waals materials*. 2D Materials **7**, 015012 (2020).

[125] X.-X. Zhang, T. Cao, Z. Lu, Y.-C. Lin, F. Zhang, Y. Wang, Z. Li, J. C. Hone, J. A. Robinson, D. Smirnov, S. G. Louie, and T. F. Heinz. *Magnetic brightening and control of dark excitons in monolayer WSe_2*. Nature Nanotechnology **12**, 883–888 (2017).

[126] Y. Zhou, G. Scuri, D. S. Wild, A. A. High, A. Dibos, L. A. Jauregui, C. Shu, K. D. Greve, K. Pistunova, A. Y. Joe, T. Taniguchi, K. Watanabe, P. Kim, M. D. Lukin, and H. Park. *Probing dark excitons in atomically thin semiconductors via near-field coupling to surface plasmon polaritons*. Nature Nanotechnology **12**, 856–860 (2017).

[127] Z. Li, T. Wang, Z. Lu, M. Khatoniar, Z. Lian, Y. Meng, M. Blei, T. Taniguchi, K. Watanabe, S. A. McGill, S. Tongay, V. M. Menon, D. Smirnov, and S. F. Shi. *Direct Observation of Gate-Tunable Dark Trions in Monolayer WSe_2*. Nano Letters **19**, 6886–6893 (2019).

[128] Z. Li, T. Wang, C. Jin, Z. Lu, Z. Lian, Y. Meng, M. Blei, S. Gao, T. Taniguchi, K. Watanabe, T. Ren, S. Tongay, L. Yang, D. Smirnov, T. Cao, and S.-F. Shi. *Emerging photoluminescence from the dark-exciton phonon replica in monolayer WSe_2*. Nature Communications **10**, 2469 (2019).

[129] S. Brem, A. Ekman, D. Christiansen, F. Katsch, M. Selig, C. Robert, X. Marie, B. Urbaszek, A. Knorr, and E. Malic. *Phonon-Assisted Photoluminescence from Indirect Excitons in Monolayers of Transition-Metal Dichalcogenides*. Nano Letters **20**, 2849–2856 (2020).

[130] V. Funk, K. Wagner, E. Wietek, J. D. Ziegler, J. Förste, J. Lindlau, M. Förg, K. Watanabe, T. Taniguchi, A. Chernikov, and A. Högele. *Spectral asymmetry of phonon sideband luminescence in monolayer and bilayer WSe_2*. Physical Review Research **3**, L052019 (2021).

[131] J. S. Ross, S. Wu, H. Yu, N. J. Ghimire, A. M. Jones, G. Aivazian, J. Yan, D. G. Mandrus, D. Xiao, W. Yao, and X. Xu. *Electrical control of neutral and charged excitons in a monolayer semiconductor*. Nature Communications **4**, 1474 (2013).

[132] T. C. Berkelbach, M. S. Hybertsen, and D. R. Reichman. *Theory of neutral and charged excitons in monolayer transition metal dichalcogenides*. Physical Review B **88**, 045318 (2013).

[133] E. Liu, J. van Baren, Z. Lu, T. Taniguchi, K. Watanabe, D. Smirnov, Y. C. Chang, and C. H. Lui. *Exciton-polaron Rydberg states in monolayer $MoSe_2$ and WSe_2*. Nature Communications **12**, 6131 (2021).

[134] M. Sidler, P. Back, O. Cotlet, A. Srivastava, T. Fink, M. Kroner, E. Demler, and A. Imamoglu. *Fermi polaron-polaritons in charge-tunable atomically thin semiconductors*. Nature Physics **13**, 255–261 (2017).

[135] D. K. Efimkin and A. H. MacDonald. *Many-body theory of trion absorption features in two-dimensional semiconductors*. Physical Review B **95**, 035417 (2017).

[136] G. D. Mahan. *Many-Particle Physics*. 3rd ed. Vol. 1. Springer New York, NY, 2000.

[137] P. Massignan, M. Zaccanti, and G. M. Bruun. *Polarons, dressed molecules and itinerant ferromagnetism in ultracold Fermi gases*. Reports on Progress in Physics **77**, 034401 (2014).

[138] K. Wagner, E. Wietek, J. D. Ziegler, M. A. Semina, T. Taniguchi, K. Watanabe, J. Zipfel, M. M. Glazov, and A. Chernikov. *Autoionization and Dressing of Excited Excitons by Free Carriers in Monolayer WSe_2*. Physical Review Letters **125**, 267401 (2020).

[139] T. Goldstein, Y.-C. Wu, S.-Y. Chen, T. Taniguchi, K. Watanabe, K. Varga, and J. Yan. *Ground and excited state exciton polarons in monolayer $MoSe_2$*. J. Chem. Phys. **153**, 071101 (2020).

[140] J. Jasiński, J. Hagel, S. Brem, E. Wietek, T. Taniguchi, K. Watanabe, A. Chernikov, N. Bruyant, M. Dyksik, A. Surrente, M. Baranowski, D. K. Maude, E. Malic, and P. Płochocka. *Quadrupolar Excitons in $MoSe_2$ Bilayers*. Nature Communications **16**, 1382 (2024).

[141] S. Feng, A. J. Campbell, M. Brotons-Gisbert, D. Andres-Penares, H. Baek, T. Taniguchi, K. Watanabe, B. Urbaszek, I. C. Gerber, and B. D. Gerardot. *Highly tunable ground and excited state excitonic dipoles in multilayer 2H-$MoSe_2$*. Nature Communications **15**, 4377 (2024).

[142] S. Feng, A. J. Campbell, B. M. Francis, H. Baek, T. Taniguchi, K. Watanabe, I. C. Gerber, B. D. Gerardot, and M. Brotons-Gisbert. *Quadrupolar and Dipolar Excitons in Bilayer 2H-$MoSe_2$*. arXiv:2503.19883v1 (2025).

[143] P. Back, S. Zeytinoglu, A. Ijaz, M. Kroner, and A. Imamoğlu. *Realization of an Electrically Tunable Narrow-Bandwidth Atomically Thin Mirror Using Monolayer $MoSe_2$*. Physical Review Letters **120**, 037401 (2018).

[144] M. Yang, L. Ren, C. Robert, D. V. Tuan, L. Lombez, B. Urbaszek, X. Marie, and H. Dery. *Relaxation and darkening of excitonic complexes in electrostatically doped monolayer WSe_2: Roles of exciton-electron and trion-electron interactions*. Physical Review B **105**, 085302 (2022).

[145] J. Zipfel, K. Wagner, J. D. Ziegler, T. Taniguchi, K. Watanabe, M. A. Semina, and A. Chernikov. *Light–matter coupling and non-equilibrium dynamics of exchange-split trions in monolayer WS_2*. The Journal of Chemical Physics **153** (2020).

[146] C. V. Raman. *A change of wave-length in light scattering*. Natrue **121**, 619 (1928).

[147] C. V. Raman and K. Krishnan. *The negative absorption of radiation*. Nature **122**, 12–13 (1928).

[148] C. V. Raman and K. S. Krishnan. *A new type of secondary radiation*. Nature **121**, 501–502 (1928).

[149] C. V. Raman. *Part II.—The Raman effect. Investigation of molecular structure by light scattering*. Transactions of the Faraday Society **25**, 781–792 (1929).

[150] R. Loudon. *The Raman effect in crystals*. Advances in Physics **13**, 423–482 (1964).

[151] C. Schüller. *Inelastic Light Scattering of Semiconductor Nanostructures*. 1st ed. Vol. 219. Springer Berlin Heidelberg, 2006.

[152] R. Saito, Y. Tatsumi, S. Huang, X. Ling, and M. S. Dresselhaus. *Raman spectroscopy of transition metal dichalcogenides*. Journal of Physics: Condensed Matter **28**, 353002 (2016).

[153] X. Zhang, X.-F. Qiao, W. Shi, J.-B. Wu, D.-S. Jiang, and P.-H. Tan. *Phonon and Raman scattering of two-dimensional transition metal dichalcogenides from monolayer, multilayer to bulk material*. Chemical Society Reviews **44**, 2757–2785 (2015).

[154] C. Lee, H. Yan, L. E. Brus, T. F. Heinz, J. Hone, and S. Ryu. *Anomalous Lattice Vibrations of Single- and Few-Layer MoS_2*. ACS Nano **4**, 2695–2700 (2010).

[155] H. Zeng, B. Zhu, K. Liu, J. Fan, X. Cui, and Q. M. Zhang. *Low-frequency Raman modes and electronic excitations in atomically thin MoS_2 films*. Physical Review B **86**, 241301 (2012).

[156] H. Li, G. Lu, Y. Wang, Z. Yin, C. Cong, Q. He, L. Wang, F. Ding, T. Yu, and H. Zhang. *Mechanical exfoliation and characterization of single- and few-layer nanosheets of WSe_2, TaS_2, and $TaSe_2$*. small **9**, 1974–1981 (2013).

[157] H. Zeng, G. B. Liu, J. Dai, Y. Yan, B. Zhu, R. He, L. Xie, S. Xu, X. Chen, W. Yao, and X. Cui. *Optical signature of symmetry variations and spin-valley coupling in atomically thin tungsten dichalcogenides*. Scientific Reports **3**, 1608 (2013).

[158] H. Sahin, S. Tongay, S. Horzum, W. Fan, J. Zhou, J. Li, J. Wu, and F. M. Peeters. *Anomalous Raman spectra and thickness-dependent electronic properties of WSe_2*. Physical Review B **87**, 165409 (2013).

[159] W. Zhao, R. M. Ribeiro, M. Toh, A. Carvalho, C. Kloc, A. H. C. Neto, and G. Eda. *Origin of indirect optical transitions in few-layer MoS_2, WS_2, and WSe_2*. Nano Letters **13**, 5627–5634 (2013).

[160] X. Luo, Y. Zhao, J. Zhang, M. Toh, C. Kloc, Q. Xiong, and S. Y. Quek. *Effects of lower symmetry and dimensionality on Raman spectra in two-dimensional WSe_2*. Physical Review B - Condensed Matter and Materials Physics **88**, 495313 (2013).

[161] H. Terrones, E. D. Corro, S. Feng, J. M. Poumirol, D. Rhodes, D. Smirnov, N. R. Pradhan, Z. Lin, M. A. Nguyen, A. L. Elías, T. E. Mallouk, L. Balicas, M. A. Pimenta, and M. Terrones. *New First Order Raman-active Modes in Few Layered Transition Metal Dichalcogenides*. Scientific Reports **4**, 4215 (2014).

[162] A. Molina-Sánchez, K. Hummer, and L. Wirtz. *Vibrational and optical properties of MoS_2: From monolayer to bulk*. Surface Science Reports **70**, 554–586 (2015).

[163] B. R. Carvalho and M. A. Pimenta. *Resonance Raman spectroscopy in semiconducting transition-metal dichalcogenides: basic properties and perspectives*. 2D Materials **7**, 042001 (2020).

[164] M. W. Iqbal, K. Shahzad, R. Akbar, and G. Hussain. *A review on Raman finger prints of doping and strain effect in TMDCs*. Microelectronic Engineering **219**, 111152 (2020).

[165] L. M. Malard, L. Lafeta, R. S. Cunha, R. Nadas, A. Gadelha, L. G. Cançado, and A. Jorio. *Studying 2D materials with advanced Raman spectroscopy: CARS, SRS and TERS*. Physical Chemistry Chemical Physics **23**, 23428–23444 (2021).

[166] P. T. Landsberg. *Recombination in Semiconductors*. Cambridge University Press, 1992.

[167] K. Kaasbjerg, K. S. Thygesen, and K. W. Jacobsen. *Phonon-limited mobility in n-type single-layer MoS_2 from first principles*. Physical Review B **85**, 115317 (2012).

[168] Z. Jin, X. Li, J. T. Mullen, and K. W. Kim. *Intrinsic transport properties of electrons and holes in monolayer transition-metal dichalcogenides*. Physical Review B **90**, 045422 (2014).

[169] W. A. Harrison. *Scattering of Electrons by Lattice Vibrations in Nonpolar Crystals*. Physical Review **104**, 1281–1290 (1956).

[170] T. Sohier, M. Calandra, and F. Mauri. *Two-dimensional Fröhlich interaction in transition-metal dichalcogenide monolayers: Theoretical modeling and first-principles calculations*. Physical Review B **94**, 085415 (2016).

[171] B. Miller, J. Lindlau, M. Bommert, A. Neumann, H. Yamaguchi, A. Holleitner, A. Högele, and U. Wurstbauer. *Tuning the Fröhlich exciton-phonon scattering in monolayer MoS_2*. Nature Communications **10**, 807 (2019).

[172] D. Braun, W. Rühle, C. Trallero-Giner, and J. Collet. *Spectroscopic determination of the optical deformation-potential constant in semiconductors*. Physical Review Letters **67**, 2335–2338 (1991).

[173] S. J. Xu, W. Liu, and M. F. Li. *Direct determination of free exciton binding energy from phonon-assisted luminescence spectra in GaN epilayers*. Applied Physics Letters **81**, 2959–2961 (2002).

[174] R. Riera, R. Rosas, J. L. Marín, J. M. Bergues, and G. Campoy. *Multiphonon resonant Raman scattering in the semimagnetic semiconductor CdMnTe: Fröhlich and deformation potential exciton-phonon interaction*. J. Phys.: Condens. Matter **15**, 3225–3248 (2003).

[175] V. V. Ursaki, I. M. Tiginyanu, V. V. Zalamai, V. M. Masalov, E. N. Samarov, G. A. Emelchenko, and F. Briones. *Photoluminescence and resonant Raman scattering from ZnO-opal structures*. Journal of Applied Physics **96**, 1001–1006 (2004).

[176] B.-L. Gao, Y. Xiong, and S.-J. Xiong. *Collective mode and peak splitting in phonon sidebands from interaction of degenerate exciton states with longitudinal optical phonons*. Physical Review B **74**, 235102 (2006).

[177] S. Sohal, Y. Alivov, Z. Fan, and M. Holtz. *Role of phonons in the optical properties of magnetron sputtered ZnO studied by resonance Raman and photoluminescence*. Journal of Applied Physics **108** (2010).

[178] A. Chernikov, V. Bornwasser, M. Koch, S. Chatterjee, C. N. Böttge, T. Feldtmann, M. Kira, S. W. Koch, T. Wassner, S. Lautenschläger, B. K. Meyer, and M. Eickhoff. *Phonon-assisted luminescence of polar semiconductors: Fröhlich coupling versus deformation-potential scattering*. Physical Review B **85**, 035201 (2012).

[179] T. Wang, Z. Li, Z. Lu, Y. Li, S. Miao, Z. Lian, Y. Meng, M. Blei, T. Taniguchi, K. Watanabe, S. Tongay, W. Yao, D. Smirnov, C. Zhang, and S. F. Shi. *Observation of Quantized Exciton Energies in Monolayer WSe_2 under a Strong Magnetic Field*. Physical Review X **10**, 021024 (2020).

[180] D. Chen, Z. Lian, X. Huang, Y. Su, M. Rashetnia, L. Ma, L. Yan, M. Blei, L. Xiang, T. Taniguchi, K. Watanabe, S. Tongay, D. Smirnov, Z. Wang, C. Zhang, Y.-T. Cui, and S.-F. Shi. *Excitonic insulator in a heterojunction moiré superlattice*. Nature Physics **18**, 1171–1176 (2022).

[181] A. Chernikov, A. M. van der Zande, H. M. Hill, A. F. Rigosi, A. Velauthapillai, J. Hone, and T. F. Heinz. *Electrical Tuning of Exciton Binding Energies in Monolayer WS_2*. Physical Review Letters **115**, 126802 (2015).

[182] A. Steinhoff, M. Florian, M. Rösner, G. Schönhoff, T. O. Wehling, and F. Jahnke. *Exciton fission in monolayer transition metal dichalcogenide semiconductors*. Nature Communications **8**, 1166 (2017).

[183] K. Xiao, T. Yan, Q. Liu, S. Yang, C. Kan, R. Duan, Z. Liu, and X. Cui. *Many-Body Effect on Optical Properties of Monolayer Molybdenum Diselenide*. The Journal of Physical Chemistry Letters **12**, 2555–2561 (2021).

[184] F. Katsch and A. Knorr. *Excitonic theory of doping-dependent optical response in atomically thin semiconductors*. Physical Review B **105**, 045301 (2022).

[185] T. C. Carvalho, F. D. Araujo, C. C. D. Santos, L. M. Alencar, J. Ribeiro-Soares, D. J. Late, A. O. Lobo, A. G. S. Filho, R. S. Alencar, and B. C. Viana. *Temperature-dependent phonon dynamics of supported and suspended monolayer tungsten diselenide*. AIP Advances **9**, 085316 (2019).

[186] E. Easy, Y. Gao, Y. Wang, D. Yan, S. M. Goushehgir, E.-H. Yang, B. Xu, and X. Zhang. *Experimental and Computational Investigation of Layer-Dependent Thermal Conductivities and Interfacial Thermal Conductance of One-to Three-Layer WSe_2*. ACS Applied Materials and Interfaces **13**, 13063–13071 (2021).

[187] S. Meier, Y. Zhumagulov, M. Dietl, P. Parzefall, M. Kempf, J. Holler, P. Nagler, P. E. F. Junior, J. Fabian, T. Korn, and C. Schüller. *Emergent trion-phonon coupling in atomically reconstructed $MoSe_2$-WSe_2 heterobilayers*. Physical Review Research **5**, L032036 (2023).

[188] H. Li, J. Wu, X. Huang, G. Lu, J. Yang, X. Lu, Q. Xiong, and H. Zhang. *Rapid and reliable thickness identification of two-dimensional nanosheets using optical microscopy*. ACS Nano **7**, 10344–10353 (2013).

[189] Y. Anzai, M. Yamamoto, S. Genchi, K. Watanabe, T. Taniguchi, S. Ichikawa, Y. Fujiwara, and H. Tanaka. *Broad range thickness identification of hexagonal boron nitride by colors*. Applied Physics Express **12**, 055007 (2019).

[190] A. Castellanos-Gomez, M. Buscema, R. Molenaar, V. Singh, L. Janssen, H. S. J. van der Zant, and G. A. Steele. *Deterministic transfer of two-dimensional materials by all-dry viscoelastic stamping*. 2D Materials **1**, 011002 (2014).

[191] Y. Guo, C. Liu, Q. Yin, C. Wei, S. Lin, T. B. Hoffman, Y. Zhao, J. H. Edgar, Q. Chen, S. P. Lau, J. Dai, H. Yao, H.-S. P. Wong, and Y. Chai. *Distinctive in-Plane Cleavage Behaviors of Two-Dimensional Layered Materials*. ACS Nano **10**, 8980–8988 (2016).

[192] K. Kim, M. Yankowitz, B. Fallahazad, S. Kang, H. C. Movva, S. Huang, S. Larentis, C. M. Corbet, T. Taniguchi, K. Watanabe, S. K. Banerjee, B. J. Leroy, and E. Tutuc. *Van der Waals Heterostructures with High Accuracy Rotational Alignment*. Nano Letters **16**, 1989–1995 (2016).

[193] K. Pürckhauer, D. Kirpal, A. J. Weymouth, and F. J. Giessibl. *Analysis of Airborne Contamination on Transition Metal Dichalcogenides with Atomic Force Microscopy Revealing That Sulfur Is the Preferred Chalcogen Atom for Devices Made in Ambient Conditions*. ACS Applied Nano Materials **2**, 2593–2598 (2019).

[194] F. Pizzocchero, L. Gammelgaard, B. S. Jessen, J. M. Caridad, L. Wang, J. Hone, P. Bøggild, and T. J. Booth. *The hot pick-up technique for batch assembly of van der Waals heterostructures*. Nature Communications **7**, 11894 (2016).

[195] D. G. Purdie, N. M. Pugno, T. Taniguchi, K. Watanabe, A. C. Ferrari, and A. Lombardo. *Cleaning interfaces in layered materials heterostructures*. Nature Communications **9**, 5387 (2018).

[196] X. Xu, W. Yao, D. Xiao, and T. F. Heinz. *Spin and pseudospins in layered transition metal dichalcogenides*. Nature Physics **10**, 343–350 (2014).

[197] T. Deilmann and K. S. Thygesen. *Finite-momentum exciton landscape in mono- and bilayer transition metal dichalcogenides*. 2D Materials **6** (2019).

[198] N. Leisgang, S. Shree, I. Paradisanos, L. Sponfeldner, C. Robert, D. Lagarde, A. Balocchi, K. Watanabe, T. Taniguchi, X. Marie, R. J. Warburton, I. C. Gerber, and B. Urbaszek. *Giant Stark splitting of an exciton in bilayer MoS_2*. Nature Nanotechnology **15**, 901–907 (2020).

[199] L. Sponfeldner, N. Leisgang, S. Shree, I. Paradisanos, K. Watanabe, T. Taniguchi, C. Robert, D. Lagarde, A. Balocchi, X. Marie, I. C. Gerber, B. Urbaszek, and R. J. Warburton. *Capacitively and Inductively Coupled Excitons in Bilayer MoS_2*. Physical Review Letters **129** (2022).

[200] Z. Li, J. Förste, K. Watanabe, T. Taniguchi, B. Urbaszek, A. S. Baimuratov, I. C. Gerber, A. Högele, and I. Bilgin. *Stacking-dependent exciton multiplicity in WSe_2 bilayers*. Physical Review B **106**, 045411 (2022).

[201] D. Erkensten, S. Brem, R. Perea-Causín, J. Hagel, F. Tagarelli, E. Lopriore, A. Kis, and E. Malic. *Electrically tunable dipolar interactions between layer-hybridized excitons*. Nanoscale **15**, 11064–11071 (2023).

[202] Y. Zhang, C. Xiao, D. Ovchinnikov, J. Zhu, X. Wang, T. Taniguchi, K. Watanabe, J. Yan, W. Yao, and X. Xu. *Every-other-layer dipolar excitons in a spin-valley locked superlattice*. Nature Nanotechnology **18**, 501–506 (2023).

[203] R. Perea-Causin, S. Brem, F. Buchner, Y. Lu, K. Watanabe, T. Taniguchi, J. M. Lupton, K. Q. Lin, and E. Malic. *Electrically tunable layer-hybridized trions in doped WSe_2 bilayers*. Nature Communications **15**, 6713 (2024).

[204] C. H. Lui, Z. Ye, C. Ji, K.-C. Chiu, C.-T. Chou, T. I. Andersen, C. Means-Shively, H. Anderson, J.-M. Wu, T. Kidd, Y.-H. Lee, and R. He. *Observation of interlayer phonon modes in van der Waals heterostructures*. Physical Review B **91**, 165403 (2015).

[205] X. Zhang, W. P. Han, J. B. Wu, S. Milana, Y. Lu, Q. Q. Li, A. C. Ferrari, and P. H. Tan. *Raman spectroscopy of shear and layer breathing modes in multilayer MoS_2*. Physical Review B **87**, 115413 (2013).

[206] L. Liang, J. Zhang, B. G. Sumpter, Q.-H. Tan, P.-H. Tan, and V. Meunier. *Low-Frequency Shear and Layer-Breathing Modes in Raman Scattering of Two-Dimensional Materials*. ACS Nano **11**, 11777–11802 (2017).

[207] A. A. Puretzky, L. Liang, X. Li, K. Xiao, K. Wang, M. Mahjouri-Samani, L. Basile, J. C. Idrobo, B. G. Sumpter, V. Meunier, and D. B. Geohegan. *Low-Frequency Raman Fingerprints of Two-Dimensional Metal Dichalcogenide Layer Stacking Configurations*. ACS Nano **9**, 6333–6342 (2015).

[208] A. A. Puretzky, L. Liang, X. Li, K. Xiao, B. G. Sumpter, V. Meunier, and D. B. Geohegan. *Twisted $MoSe_2$ Bilayers with Variable Local Stacking and Interlayer Coupling Revealed by Low-Frequency Raman Spectroscopy.* ACS Nano **10**, 2736–2744 (2016).

[209] S. Huang, L. Liang, X. Ling, A. A. Puretzky, D. B. Geohegan, B. G. Sumpter, J. Kong, V. Meunier, and M. S. Dresselhaus. *Low-Frequency Interlayer Raman Modes to Probe Interface of Twisted Bilayer MoS_2.* Nano Letters **16**, 1435–1444 (2016).

[210] M. L. Lin, Q. H. Tan, J. B. Wu, X. S. Chen, J. H. Wang, Y. H. Pan, X. Zhang, X. Cong, J. Zhang, W. Ji, P. A. Hu, K. H. Liu, and P. H. Tan. *Moiré phonons in twisted bilayer MoS_2.* ACS Nano **12**, 8770–8780 (2018).

[211] K. Q. Lin, J. Holler, J. M. Bauer, P. Parzefall, M. Scheuck, B. Peng, T. Korn, S. Bange, J. M. Lupton, and C. Schüller. *Large-Scale Mapping of Moiré Superlattices by Hyperspectral Raman Imaging.* Advanced Materials **33**, 2008333 (2021).

[212] M. Boora, Y. C. Lin, C. Chen, N. Trainor, J. A. Robinson, J. M. Redwing, and J. Y. Suh. *Low-Frequency Raman Study of Large-Area Twisted Bilayers of WS_2 Stacked by an Etchant-Free Transfer Method.* ACS Applied Materials and Interfaces **16**, 2902–2911 (2024).

[213] G. Plechinger, S. Heydrich, J. Eroms, D. Weiss, C. Schüller, and T. Korn. *Raman spectroscopy of the interlayer shear mode in few-layer MoS_2 flakes.* Applied Physics Letters **101** (2012).

[214] L. Li and M. Wu. *Binary Compound Bilayer and Multilayer with Vertical Polarizations: Two-Dimensional Ferroelectrics, Multiferroics, and Nanogenerators.* ACS Nano **11**, 6382–6388 (2017).

[215] D. Yang, J. Liang, J. Wu, Y. Xiao, J. I. Dadap, K. Watanabe, T. Taniguchi, and Z. Ye. *Non-volatile electrical polarization switching via domain wall release in 3R-MoS_2 bilayer.* Nature Communications **15** (2024).

[216] Y. Hassan, B. Singh, M. Joe, B. M. Son, T. D. Ngo, Y. Jang, S. Sett, A. Singha, R. Biswas, M. Bhakar, K. Watanabe, T. Taniguchi, V. Raghunathan, G. Sheet, Z. Lee, W. J. Yoo, P. K. Srivastava, and C. Lee. *Twist-Controlled Ferroelectricity and Emergent Multiferroicity in WSe_2 Bilayers.* Advanced Materials (2024).

[217] T. Ouyang, S. Cha, Y. Sun, T. Taniguchi, K. Watanabe, N. M. Gabor, and C. H. Lui. *Electrically Switching Ferroelectric Order in 3R-MoS_2 Layers.* Nano Lett **25**, 1459–1465 (2025).

[218] Z. Fei, W. Zhao, T. A. Palomaki, B. Sun, M. K. Miller, Z. Zhao, J. Yan, X. Xu, and D. H. Cobden. *Ferroelectric switching of a two-dimensional metal.* Nature **560**, 336–339 (2018).

[219] J. Sung, Y. Zhou, G. Scuri, V. Zólyomi, T. I. Andersen, H. Yoo, D. S. Wild, A. Y. Joe, R. J. Gelly, H. Heo, S. J. Magorrian, D. Bérubé, A. M. Valdivia, T. Taniguchi, K. Watanabe, M. D. Lukin, P. Kim, V. I. Fal'ko, and H. Park. *Broken mirror symmetry in excitonic response of reconstructed domains in twisted $MoSe_2/MoSe_2$ bilayers*. Nature Nanotechnology **15**, 750–754 (2020).

[220] T. I. Andersen, G. Scuri, A. Sushko, K. D. Greve, J. Sung, Y. Zhou, D. S. Wild, R. J. Gelly, H. Heo, D. Bérubé, A. Y. Joe, L. A. Jauregui, K. Watanabe, T. Taniguchi, P. Kim, H. Park, and M. D. Lukin. *Excitons in a reconstructed moiré potential in twisted WSe_2/WSe_2 homobilayers*. Nature Materials **20**, 480–487 (2021).

[221] J. Wang, H. Liu, X. Hu, Y. Liu, and D. Liu. *Imaging of Defect-Accelerated Energy Transfer in $MoS_2/hBN/WS_2$Heterostructures*. ACS Applied Materials and Interfaces **14**, 8521–8526 (2022).

[222] J. Liang, D. Yang, J. Wu, J. I. Dadap, K. Watanabe, T. Taniguchi, and Z. Ye. *Optically Probing the Asymmetric Interlayer Coupling in Rhombohedral-Stacked MoS_2 Bilayer*. Physical Review X **12** (2022).

[223] A. Weston, E. G. Castanon, V. Enaldiev, F. Ferreira, S. Bhattacharjee, S. Xu, H. Corte-León, Z. Wu, N. Clark, A. Summerfield, T. Hashimoto, Y. Gao, W. Wang, M. Hamer, H. Read, L. Fumagalli, A. V. Kretinin, S. J. Haigh, O. Kazakova, A. K. Geim, V. I. Fal'ko, and R. Gorbachev. *Interfacial ferroelectricity in marginally twisted 2D semiconductors*. Nature Nanotechnology **17**, 390–395 (2022).

[224] P. Meng, Y. Wu, R. Bian, E. Pan, B. Dong, X. Zhao, J. Chen, L. Wu, Y. Sun, Q. Fu, Q. Liu, D. Shi, Q. Zhang, Y. W. Zhang, Z. Liu, and F. Liu. *Sliding induced multiple polarization states in two-dimensional ferroelectrics*. Nature Communications **13** (2022).

[225] S. Zhang, Y. Liu, Z. Sun, X. Chen, B. Li, S. L. Moore, S. Liu, Z. Wang, S. E. Rossi, R. Jing, J. Fonseca, B. Yang, Y. Shao, C. Y. Huang, T. Handa, L. Xiong, M. Fu, T. C. Pan, D. Halbertal, X. Xu, W. Zheng, P. J. Schuck, A. N. Pasupathy, C. R. Dean, X. Zhu, D. H. Cobden, X. Xu, M. Liu, M. M. Fogler, J. C. Hone, and D. N. Basov. *Visualizing moiré ferroelectricity via plasmons and nano-photocurrent in graphene/twisted-WSe_2 structures*. Nature Communications **14** (2023).

[226] A. K. Geim and I. V. Grigorieva. *Van der Waals heterostructures*. Nature **499**, 419–425 (2013).

[227] T. Roy, M. Tosun, X. Cao, H. Fang, D. H. Lien, P. Zhao, Y. Z. Chen, Y. L. Chueh, J. Guo, and A. Javey. *Dual-gated MoS_2/WSe_2 van der Waals tunnel diodes and transistors*. ACS Nano **9**, 2071–2079 (2015).

[228] A. Nourbakhsh, A. Zubair, M. S. Dresselhaus, and T. Palacios. *Transport properties of a MoS_2/WSe_2 heterojunction transistor and its potential for application*. Nano Letters **16**, 1359–1366 (2016).

[229] C. Li, X. Yan, X. Song, W. Bao, S. Ding, D. W. Zhang, and P. Zhou. *WSe_2/MoS_2 and $MoTe_2/SnSe_2$ van der Waals heterostructure transistors with different band alignment*. Nanotechnology **28** (2017).

[230] K. Nakamura, N. Nagamura, K. Ueno, T. Taniguchi, K. Watanabe, and K. Nagashio. *All 2D Heterostructure Tunnel Field-Effect Transistors: Impact of Band Alignment and Heterointerface Quality*. ACS Applied Materials and Interfaces **12**, 51598–51606 (2020).

[231] Z. Cheng, R. Cao, K. Wei, Y. Yao, X. Liu, J. Kang, J. Dong, Z. Shi, H. Zhang, and X. Zhang. *2D Materials Enabled Next-Generation Integrated Optoelectronics: from Fabrication to Applications*. Advanced Science **8** (2021).

[232] M. Zhao, Y. Hao, C. Zhang, R. Zhai, B. Liu, W. Liu, C. Wang, S. H. M. Jafri, A. Razaq, R. Papadakis, J. Liu, X. Ye, X. Zheng, and H. Li. *Advances in Two-Dimensional Materials for Optoelectronics Applications*. Crystals **12**, 1087 (2022).

[233] Z. U. D. Babar, A. Raza, A. Cassinese, and V. Iannotti. *Two Dimensional Heterostructures for Optoelectronics: Current Status and Future Perspective*. Molecules **28**, 2275 (2023).

[234] K. H. Jin, W. Jiang, G. Sethi, and F. Liu. *Topological quantum devices: a review*. Nanoscale **15**, 12787–12817 (2023).

[235] S. Pandey, R. Kiran, R. Trivedi, Y. Raviprakash, S. D. Kamath, and V. Mishra. *Insights on bio-medical, quantum, and optoelectronic applications of 2D transition metal dichalcogenides–a review*. Optical and Quantum Electronics **56** (2024).

[236] K. S. Novoselov, A. Mishchenko, A. Carvalho, and A. H. C. Neto. *2D materials and van der Waals heterostructures*. Science **353**, 6298 (2016).

[237] Y. Jiang, S. Chen, W. Zheng, B. Zheng, and A. Pan. *Interlayer exciton formation, relaxation, and transport in TMD van der Waals heterostructures*. Light: Science & Applications **10**, 72 (2021).

[238] R. Ribeiro-Palau, C. Zhang, K. Watanabe, T. Taniguchi, J. Hone, and C. R. Dean. *Twistable electronics with dynamically rotatable heterostructures*. Science **361**, 690–693 (2018).

[239] M. Brotons-Gisbert, B. D. Gerardot, A. W. Holleitner, and U. Wurstbauer. *Interlayer and Moiré excitons in atomically thin double layers: From individual quantum emitters to degenerate ensembles*. MRS Bulletin **49**, 914–931 (2024).

[240] N. P. Wilson, W. Yao, J. Shan, and X. Xu. *Excitons and emergent quantum phenomena in stacked 2D semiconductors*. Nature **599**, 383–392 (2021).

[241] K. F. Mak and J. Shan. *Semiconductor moiré materials*. Nature Nanotechnology **17**, 686–695 (2022).

[242] A. Tartakovskii. *Excitons in 2D heterostructures*. Nature Reviews Physics **2**, 8–9 (2019).

[243] P. Rivera, H. Yu, K. L. Seyler, N. P. Wilson, W. Yao, and X. Xu. *Interlayer valley excitons in heterobilayers of transition metal dichalcogenides*. Nature Nanotechnology **13**, 1004–1015 (2018).

[244] K. Tran, J. Choi, and A. Singh. *Moiré and beyond in transition metal dichalcogenide twisted bilayers*. 2D Materials **8**, 022002 (2021).

[245] K.-Q. Lin. *A roadmap for interlayer excitons*. Light: Science & Applications **10**, 99 (2021).

[246] R. L. Anderson. *Germanium-Gallium Arsenide Heterojunctions [Letter to the Editor]*. IBM Journal of Research and Development **4**, 283–287 (1960).

[247] K. Xu, Y. Xu, H. Zhang, B. Peng, H. Shao, G. Ni, J. Li, M. Yao, H. Lu, H. Zhu, and C. M. Soukoulis. *The role of Anderson's rule in determining electronic, optical and transport properties of transition metal dichalcogenide heterostructures*. Physical Chemistry Chemical Physics **20**, 30351–30364 (2018).

[248] J. F. Silveira, R. Besse, A. C. Dias, N. A. Caturello, and J. L. D. Silva. *Tailoring Excitonic and Optoelectronic Properties of Transition Metal Dichalcogenide Bilayers*. Journal of Physical Chemistry C **126**, 9173–9184 (2022).

[249] J. Kistner-Morris, A. Shi, E. Liu, T. Arp, F. Farahmand, T. Taniguchi, K. Watanabe, V. Aji, C. H. Lui, and N. Gabor. *Electric-field tunable Type-I to Type-II band alignment transition in $MoSe_2/WS_2$ heterobilayers*. Nature Communications **15**, 4075 (2024).

[250] M. Li, M. Z. Bellus, J. Dai, L. Ma, X. Li, H. Zhao, and X. C. Zeng. *A type-I van der Waals heterobilayer of WSe_2 /$MoTe_2$*. Nanotechnology **29**, 335203 (2018).

[251] K. Kośmider and J. Fernández-Rossier. *Electronic properties of the MoS_2-WS_2 heterojunction*. Physical Review B **87**, 075451 (2013).

[252] J. Kang, S. Tongay, J. Zhou, J. Li, and J. Wu. *Band offsets and heterostructures of two-dimensional semiconductors*. Applied Physics Letters **102**, 012111 (2013).

[253] H. Terrones, F. López-Urías, and M. Terrones. *Novel hetero-layered materials with tunable direct band gaps by sandwiching different metal disulfides and diselenides*. Scientific Reports **3**, 1549 (2013).

[254] H. Terrones and M. Terrones. *Bilayers of transition metal dichalcogenides: Different stackings and heterostructures*. Journal of Materials Research **29**, 373–382 (2014).

[255] V. O. Özçelik, J. G. Azadani, C. Yang, S. J. Koester, and T. Low. *Band alignment of two-dimensional semiconductors for designing heterostructures with momentum space matching*. Physical Review B **94**, 035125 (2016).

[256] O. Karni, E. Barré, S. C. Lau, R. Gillen, E. Y. Ma, B. Kim, K. Watanabe, T. Taniguchi, J. Maultzsch, K. Barmak, R. H. Page, and T. F. Heinz. *Infrared Interlayer Exciton Emission in MoS_2/WSe_2 Heterostructures*. Physical Review Letters **123**, 247402 (2019).

[257] Y. Liu, A. Elbanna, W. Gao, J. Pan, Z. Shen, and J. Teng. *Interlayer Excitons in Transition Metal Dichalcogenide Semiconductors for 2D Optoelectronics*. Advanced Materials **34** (2022).

[258] J. Shim, S. Oh, D.-H. Kang, S.-H. Jo, M. H. Ali, W.-Y. Choi, K. Heo, J. Jeon, S. Lee, M. Kim, Y. J. Song, and J.-H. Park. *Phosphorene/rhenium disulfide heterojunction-based negative differential resistance device for multi-valued logic*. Nature Communications **7**, 13413 (2016).

[259] R. Yan, S. Fathipour, Y. Han, B. Song, S. Xiao, M. Li, N. Ma, V. Protasenko, D. A. Muller, D. Jena, and H. G. Xing. *Esaki Diodes in van der Waals Heterojunctions with Broken-Gap Energy Band Alignment*. Nano Letters **15**, 5791–5798 (2015).

[260] A. Beer, K. Zollner, C. S. de Brito, P. E. F. Junior, P. Parzefall, T. S. Ghiasi, J. Ingla-Aynés, S. Mañas-Valero, C. Boix-Constant, K. Watanabe, T. Taniguchi, J. Fabian, H. S. J. van der Zant, Y. G. Gobato, and C. Schüller. *Proximity-Induced Exchange Interaction and Prolonged Valley Lifetime in $MoSe_2$/CrSBr Van-Der-Waals Heterostructure with Orthogonal Spin Textures*. ACS Nano **18**, 31044–31054 (2024).

[261] K. Q. Lin, P. E. F. Junior, R. Hübner, J. D. Ziegler, J. M. Bauer, F. Buchner, M. Florian, F. Hofmann, K. Watanabe, T. Taniguchi, J. Fabian, A. Steinhoff, A. Chernikov, S. Bange, and J. M. Lupton. *Ultraviolet interlayer excitons in bilayer WSe_2*. Nature Nanotechnology **19**, 196–201 (2024).

[262] H. C. Kamban and T. G. Pedersen. *Interlayer excitons in van der Waals heterostructures: Binding energy, Stark shift, and field-induced dissociation*. Scientific Reports **10**, 5537 (2020).

[263] P. K. Nayak, Y. Horbatenko, S. Ahn, G. Kim, J. U. Lee, K. Y. Ma, A. R. Jang, H. Lim, D. Kim, S. Ryu, H. Cheong, N. Park, and H. S. Shin. *Probing Evolution of Twist-Angle-Dependent Interlayer Excitons in $MoSe_2/WSe_2$ van der Waals Heterostructures*. ACS Nano **11**, 4041–4050 (2017).

[264] X. Hong, J. Kim, S.-F. Shi, Y. Zhang, C. Jin, Y. Sun, S. Tongay, J. Wu, Y. Zhang, and F. Wang. *Ultrafast charge transfer in atomically thin MoS_2/WS_2 heterostructures*. Nature Nanotechnology **9**, 682–686 (2014).

[265] P. Merkl, F. Mooshammer, P. Steinleitner, A. Girnghuber, K.-Q. Lin, P. Nagler, J. Holler, C. Schüller, J. M. Lupton, T. Korn, S. Ovesen, S. Brem, E. Malic, and R. Huber. *Ultrafast transition between exciton phases in van der Waals heterostructures*. Nature Materials **18**, 691–696 (2019).

[266] S. Ovesen, S. Brem, C. Linderälv, M. Kuisma, T. Korn, P. Erhart, M. Selig, and E. Malic. *Interlayer exciton dynamics in van der Waals heterostructures*. Communications Physics **2**, 23 (2019).

[267] D. Schmitt, J. P. Bange, W. Bennecke, A. A. AlMutairi, G. Meneghini, K. Watanabe, T. Taniguchi, D. Steil, D. R. Luke, R. T. Weitz, S. Steil, G. S. Jansen, S. Brem, E. Malic, S. Hofmann, M. Reutzel, and S. Mathias. *Formation of moiré interlayer excitons in space and time*. Nature **608**, 499–503 (2022).

[268] N. R. Wilson, P. V. Nguyen, K. Seyler, P. Rivera, A. J. Marsden, Z. P. L. Laker, G. C. Constantinescu, V. Kandyba, A. Barinov, N. D. M. Hine, X. Xu, and D. H. Cobden. *Determination of band offsets, hybridization, and exciton binding in 2D semiconductor heterostructures*. Science Advances **3**, 31601832 (2017).

[269] R. Gillen and J. Maultzsch. *Interlayer excitons in $MoSe_2/WSe_2$ heterostructures from first principles*. Physical Review B **97**, 165306 (2018).

[270] E. Wietek, M. Florian, J. Göser, T. Taniguchi, K. Watanabe, A. Högele, M. M. Glazov, A. Steinhoff, and A. Chernikov. *Nonlinear and Negative Effective Diffusivity of Interlayer Excitons in Moiré-Free Heterobilayers*. Physical Review Letters **132**, 016202 (2024).

[271] K. L. Seyler, P. Rivera, H. Yu, N. P. Wilson, E. L. Ray, D. G. Mandrus, J. Yan, W. Yao, and X. Xu. *Signatures of moiré-trapped valley excitons in $MoSe_2/WSe_2$ heterobilayers*. Nature **567**, 66–70 (2019).

[272] T. Woźniak, P. E. F. Junior, G. Seifert, A. Chaves, and J. Kunstmann. *Exciton g factors of van der Waals heterostructures from first-principles calculations*. Physical Review B **101**, 235408 (2020).

[273] E. Liu, E. Barré, J. van Baren, M. Wilson, T. Taniguchi, K. Watanabe, Y.-T. Cui, N. M. Gabor, T. F. Heinz, Y.-C. Chang, and C. H. Lui. *Signatures of moiré trions in $WSe_2/MoSe_2$ heterobilayers*. Nature **594**, 46–50 (2021).

[274] J. Holler, M. Selig, M. Kempf, J. Zipfel, P. Nagler, M. Katzer, F. Katsch, M. V. Ballottin, A. A. Mitioglu, A. Chernikov, P. C. M. Christianen, C. Schüller, A. Knorr, and T. Korn. *Interlayer exciton valley polarization dynamics in large magnetic fields*. Physical Review B **105**, 085303 (2022).

[275] S. Zhao, Z. Li, X. Huang, A. Rupp, J. Göser, I. A. Vovk, S. Y. Kruchinin, K. Watanabe, T. Taniguchi, I. Bilgin, A. S. Baimuratov, and A. Högele. *Excitons in mesoscopically reconstructed moiré heterostructures*. Nature Nanotechnology **18**, 572–579 (2023).

[276] J. Holler, M. Selig, D. S. Smirnov, M. Kempf, J. Zipfel, P. Nagler, M. Katzer, F. Katsch, M. V. Ballottin, A. A. Mitioglu, A. Chernikov, P. C. M. Christianen, C. Schüller, A. Knorr, and T. Korn. *Magneto-Spectroscopy of Interlayer Excitons in Transition-Metal Dichalcogenide Heterostructures*. physica status solidi (b) **262**, 2400079 (2025).

[277] P. E. F. Junior and J. Fabian. *Signatures of Electric Field and Layer Separation Effects on the Spin-Valley Physics of $MoSe_2/WSe_2$ Heterobilayers: From Energy Bands to Dipolar Excitons*. Nanomaterials **13**, 01187 (2023).

[278] F. Volmer, M. Ersfeld, P. E. F. Junior, L. Waldecker, B. Parashar, L. Rathmann, S. Dubey, I. Cojocariu, V. Feyer, K. Watanabe, T. Taniguchi, C. M. Schneider, L. Plucinski, C. Stampfer, J. Fabian, and B. Beschoten. *Twist angle dependent interlayer transfer of valley polarization from excitons to free charge carriers in $WSe_2/MoSe_2$ heterobilayers*. npj 2D Materials and Applications **7**, 58 (2023).

[279] M. Brotons-Gisbert, H. Baek, A. Campbell, K. Watanabe, T. Taniguchi, and B. D. Gerardot. *Moiré-Trapped Interlayer Trions in a Charge-Tunable $WSe_2/MoSe_2$ Heterobilayer*. Physical Review X **11**, 031033 (2021).

[280] H. Yu, G.-B. Liu, and W. Yao. *Brightened spin-triplet interlayer excitons and optical selection rules in van der Waals heterobilayers*. 2D Materials **5**, 035021 (2018).

[281] L. Zhang, R. Gogna, G. W. Burg, J. Horng, E. Paik, Y.-H. Chou, K. Kim, E. Tutuc, and H. Deng. *Highly valley-polarized singlet and triplet interlayer excitons in van der Waals heterostructure*. Physical Review B **100**, 041402 (2019).

[282] T. Wang, S. Miao, Z. Li, Y. Meng, Z. Lu, Z. Lian, M. Blei, T. Taniguchi, K. Watanabe, S. Tongay, D. Smirnov, and S.-F. Shi. *Giant Valley-Zeeman Splitting from Spin-Singlet and Spin-Triplet Interlayer Excitons in WSe_2 /$MoSe_2$ Heterostructure*. Nano Letters **20**, 694–700 (2020).

[283] A. Y. Joe, L. A. Jauregui, K. Pistunova, A. M. M. Valdivia, Z. Lu, D. S. Wild, G. Scuri, K. D. Greve, R. J. Gelly, Y. Zhou, J. Sung, A. Sushko, T. Taniguchi, K. Watanabe, D. Smirnov, M. D. Lukin, H. Park, and P. Kim. *Electrically controlled emission from singlet and triplet exciton species in atomically thin light-emitting diodes*. Physical Review B **103**, L161411 (2021).

[284] J. G. Roch, D. Miserev, G. Froehlicher, N. Leisgang, L. Sponfeldner, K. Watanabe, T. Taniguchi, J. Klinovaja, D. Loss, and R. J. Warburton. *First-Order Magnetic Phase Transition of Mobile Electrons in Monolayer MoS_2*. Physical Review Letters **124** (2020).

[285] D. V. Tuan, B. Scharf, Z. Wang, J. Shan, K. F. Mak, I. Žutić, and H. Dery. *Probing many-body interactions in monolayer transition-metal dichalcogenides*. Physical Review B **99**, 085301 (2019).

[286] K. Tran, G. Moody, F. Wu, X. Lu, J. Choi, K. Kim, A. Rai, D. A. Sanchez, J. Quan, A. Singh, J. Embley, A. Zepeda, M. Campbell, T. Autry, T. Taniguchi, K. Watanabe, N. Lu, S. K. Banerjee, K. L. Silverman, S. Kim, E. Tutuc, L. Yang, A. H. MacDonald, and X. Li. *Evidence for moiré excitons in van der Waals heterostructures*. Nature **567**, 71–75 (2019).

[287] B. Polovnikov, J. Scherzer, S. Misra, X. Huang, C. Mohl, Z. Li, J. Göser, J. Förste, I. Bilgin, K. Watanabe, T. Taniguchi, A. S. Baimuratov, and A. Högele. *Coulomb-correlated states of moiré excitons and charges in a semiconductor moiré lattice*. arXiv:2208.04056 (2022).

[288] D. Halbertal, N. R. Finney, S. S. Sunku, A. Kerelsky, C. Rubio-Verdú, S. Shabani, L. Xian, S. Carr, S. Chen, C. Zhang, L. Wang, D. Gonzalez-Acevedo, A. S. McLeod, D. Rhodes, K. Watanabe, T. Taniguchi, E. Kaxiras, C. R. Dean, J. C. Hone, A. N. Pasupathy, D. M. Kennes, A. Rubio, and D. N. Basov. *Moiré metrology of energy landscapes in van der Waals heterostructures*. Nature Communications **12**, 242 (2021).

[289] N. Saigal, L. Klebl, H. Lambers, S. Bahmanyar, V. Antić, D. M. Kennes, T. O. Wehling, and U. Wurstbauer. *Collective Charge Excitations between Moiré Minibands in Twisted WSe_2 Bilayers Probed with Resonant Inelastic Light Scattering.* Physical Review Letters **133**, 046902 (2024).

[290] C. Zhang, C.-P. Chuu, X. Ren, M.-Y. Li, L.-J. Li, C. Jin, M.-Y. Chou, and C.-K. Shih. *Interlayer couplings, Moiré patterns, and 2D electronic superlattices in MoS_2/WSe_2 hetero-bilayers.* Science Advances **3** (2017).

[291] H. Park, J. Zhu, X. Wang, Y. Wang, W. Holtzmann, T. Taniguchi, K. Watanabe, J. Yan, L. Fu, T. Cao, D. Xiao, D. R. Gamelin, H. Yu, W. Yao, and X. Xu. *Dipole ladders with large Hubbard interaction in a moiré exciton lattice.* Nature Physics **19**, 1286–1292 (2023).

[292] Q. Tan, A. Rasmita, Z. Zhang, X. Dai, R. He, X. Cai, K. Watanabe, T. Taniguchi, H. Cai, and W.-b. Gao. *Enhanced coherence from correlated states in WSe_2/MoS_2 moiré heterobilayer.* Nature Communications **16**, 4518 (2025).

[293] Z. Lian, Y. Meng, L. Ma, I. Maity, L. Yan, Q. Wu, X. Huang, D. Chen, X. Chen, X. Chen, M. Blei, T. Taniguchi, K. Watanabe, S. Tongay, J. Lischner, Y. T. Cui, and S. F. Shi. *Valley-polarized excitonic Mott insulator in WS_2/WSe_2 moiré superlattice.* Nature Physics **20**, 34–39 (2024).

[294] E. C. Regan, D. Wang, C. Jin, M. I. B. Utama, B. Gao, X. Wei, S. Zhao, W. Zhao, Z. Zhang, K. Yumigeta, M. Blei, J. D. Carlström, K. Watanabe, T. Taniguchi, S. Tongay, M. Crommie, A. Zettl, and F. Wang. *Mott and generalized Wigner crystal states in WSe_2/WS_2 moiré superlattices.* Nature **579**, 359–363 (2020).

[295] H. Li, S. Li, M. H. Naik, J. Xie, X. Li, J. Wang, E. Regan, D. Wang, W. Zhao, S. Zhao, S. Kahn, K. Yumigeta, M. Blei, T. Taniguchi, K. Watanabe, S. Tongay, A. Zettl, S. G. Louie, F. Wang, and M. F. Crommie. *Imaging moiré flat bands in three-dimensional reconstructed WSe_2/WS_2 superlattices.* Nature Materials **20**, 945–950 (2021).

[296] T. Li, J. Zhu, Y. Tang, K. Watanabe, T. Taniguchi, V. Elser, J. Shan, and K. F. Mak. *Charge-order-enhanced capacitance in semiconductor moiré superlattices.* Nature Nanotechnology **16**, 1068–1072 (2021).

[297] X. Huang, T. Wang, S. Miao, C. Wang, Z. Li, Z. Lian, T. Taniguchi, K. Watanabe, S. Okamoto, D. Xiao, S. F. Shi, and Y. T. Cui. *Correlated insulating states at fractional fillings of the WS_2/WSe_2 moiré lattice.* Nature Physics **17**, 715–719 (2021).

[298] M. H. Naik, E. C. Regan, Z. Zhang, Y. H. Chan, Z. Li, D. Wang, Y. Yoon, C. S. Ong, W. Zhao, S. Zhao, M. I. B. Utama, B. Gao, X. Wei, M. Sayyad, K. Yumigeta, K. Watanabe, T. Taniguchi, S. Tongay, F. H. da Jornada, F. Wang, and S. G. Louie. *Intralayer charge-transfer moiré excitons in van der Waals superlattices.* Nature **609**, 52–57 (2022).

[299] T. Smoleński, P. E. Dolgirev, C. Kuhlenkamp, A. Popert, Y. Shimazaki, P. Back, X. Lu, M. Kroner, K. Watanabe, T. Taniguchi, I. Esterlis, E. Demler, and A. Imamoğlu. *Signatures of Wigner crystal of electrons in a monolayer semiconductor*. Nature **595**, 53–57 (2021).

[300] Y. Zhang, N. F. Q. Yuan, and L. Fu. *Moiré quantum chemistry: Charge transfer in transition metal dichalcogenide superlattices*. Physical Review B **102**, 201115 (2020).

[301] Z. Shan, W. Su, K. Watanabe, T. Taniguchi, S. Zhu, Y. Xu, and Y. Tang. *Gate-tunable chiral spin mode in WSe_2/WS_2 moiré superlattices*. arXiv:2509.16511 (2025).

[302] A. Laturia, M. L. V. de Put, and W. G. Vandenberghe. *Dielectric properties of hexagonal boron nitride and transition metal dichalcogenides: from monolayer to bulk*. npj 2D Materials and Applications **2**, 6 (2018).

[303] E. M. Alexeev, D. A. Ruiz-Tijerina, M. Danovich, M. J. Hamer, D. J. Terry, P. K. Nayak, S. Ahn, S. Pak, J. Lee, J. I. Sohn, M. R. Molas, M. Koperski, K. Watanabe, T. Taniguchi, K. S. Novoselov, R. V. Gorbachev, H. S. Shin, V. I. Fal'ko, and A. I. Tartakovskii. *Resonantly hybridized excitons in moiré superlattices in van der Waals heterostructures*. Nature **567**, 81–86 (2019).

[304] F. Wu, T. Lovorn, E. Tutuc, and A. H. MacDonald. *Hubbard Model Physics in Transition Metal Dichalcogenide Moiré Bands*. Physical Review Letters **121**, 026402 (2018).

[305] J. Scherzer, L. Lackner, B. Han, B. Polovnikov, L. Husel, J. Göser, Z. Li, J.-C. Drawer, M. Esmann, C. Bennenhei, F. Eilenberger, K. Watanabe, T. Taniguchi, A. S. Baimuratov, C. Schneider, and A. Högele. *Correlated magnetism of moiré exciton-polaritons on a triangular electron-spin lattice*. arXiv:2405.12698v1 (2024).

[306] A. Pinczuk, L. Brillson, E. Burstein, and E. Anastassakis. *Resonant Light Scattering by Single-Particle Electronic Excitations in n-GaAs*. Physical Review Letters **27**, 317–320 (1971).

[307] G. Abstreiter and K. Ploog. *Inelastic Light Scattering from a Quasi-Two-Dimensional Electron System in GaAs/AlGaAs Heterojunctions*. Physical Review Letters **42**, 1308–1311 (1979).

[308] G. Abstreiter, T. Egeler, S. Beeck, A. Seilmeier, H. J. Hobner, G. Weimann, and W. Schlapp. *Electronic Excitations in Narrow GaAs/AlGaAs Quantum Well Structures*. Surface Science **196**, 613–618 (1988).

[309] S. D. Sarma and D.-W. Wang. *Resonant Raman Scattering by Elementary Electronic Excitations in Semiconductor Structures*. Physical Review Letters **83**, 816–819 (1999).

[310] M. Kang, A. Pinczuk, B. S. Dennis, M. A. Eriksson, L. N. Pfeiffer, and K. W. West. *Inelastic Light Scattering by Gap Excitations of Fractional Quantum Hall States at* $1/3 \leq \nu \leq 2/3$. Physical Review Letters **84**, 546–549 (2000).

[311] S. Meier, P. E. F. Junior, F. Haas, E.-S. Heller, F. Dirnberger, V. Zeller, T. Korn, J. Fabian, D. Bougeard, and C. Schüller. *Intersubband excitations in ultrathin core-shell nanowires in the one-dimensional quantum limit probed by resonant inelastic light scattering*. Physical Review B **104**, 235307 (2021).

[312] Y. Tang, J. Gu, S. Liu, K. Watanabe, T. Taniguchi, J. Hone, K. F. Mak, and J. Shan. *Tuning layer-hybridized moiré excitons by the quantum-confined Stark effect*. Nature Nanotechnology **16**, 52–57 (2021).

[313] B. Polovnikov, J. Scherzer, S. Misra, X. Huang, C. Mohl, Z. Li, J. Göser, J. Förste, I. Bilgin, K. Watanabe, T. Taniguchi, A. Högele, and A. S. Baimuratov. *Supplemental Material: Field-Induced Hybridization of Moiré Excitons in $MoSe_2/WS_2$ Heterobilayers*. Physical Review Letters **132**, 076902 (2024).

[314] H. Haug and S. W. Koch. *Semiconductor laser theory with many-body effects*. Physical Review A **39**, 1887–1898 (1989).

[315] P. Parzefall, N. Paulik, C. S. de Brito, J. Göser, J. Trapp, K. Watanabe, T. Taniguchi, D. Erkensten, G. Meneghini, Y. G. Gobato, E. Malic, A. Högele, and C. Schüller. *Programmable phonon-assisted resonant energy transfer between moiré cells in charge-tunable $MoSe_2$-WS_2 heterobilayers*. npj 2D Materials and Applications **9**, 84 (2025).

[316] N. Paulik. *Investigating moiré phenomena in $MoSe_2$-WS_2 van der Waals heterostructures*. Universität Regensburg, Master's thesis (2025).

[317] A. M. Shentsev and M. M. Glazov. *Electromagnetic field assisted exciton diffusion in moiré superlattices*. Physical Review B **111**, 045301 (2025).

[318] Y. Tang, L. Li, T. Li, Y. Xu, S. Liu, K. Barmak, K. Watanabe, T. Taniguchi, A. H. MacDonald, J. Shan, and K. F. Mak. *Simulation of Hubbard model physics in WSe_2/WS_2 moiré superlattices*. Nature **579**, 353–358 (2020).

[319] P. Parzefall, N. Paulik, C. S. de Brito, J. Göser, J. Trapp, K. Watanabe, T. Taniguchi, D. Erkensten, G. Meneghini, Y. G. Gobato, E. Malic, A. Högele, and C. Schüller. *Supplementary Information: Programmable phonon-assisted resonant energy transfer between moiré cells in charge-tunable $MoSe_2$-WS_2 heterobilayers*. npj 2D Materials and Applications **9**, 84 (2025).

[320] A. Berkdemir, H. R. Gutiérrez, A. R. Botello-Méndez, N. Perea-López, A. L. Elías, C.-I. Chia, B. Wang, V. H. Crespi, F. López-Urías, J.-C. Charlier, H. Terrones, and M. Terrones. *Identification of individual and few layers of WS_2 using Raman Spectroscopy*. Scientific Reports **3**, 1755 (2013).

[321] D. Nam, J.-U. Lee, and H. Cheong. *Excitation energy dependent Raman spectrum of $MoSe_2$*. Scientific Reports **5**, 17113 (2015).

[322] S. Rahman, X. Sun, Y. Zhu, and Y. Lu. *Extraordinary Phonon Displacement and Giant Resonance Raman Enhancement in WSe_2/WS_2 Moiré Heterostructures*. ACS Nano **16**, 21505–21517 (2022).

[323] A. M. Jones, H. Yu, J. R. Schaibley, J. Yan, D. G. Mandrus, T. Taniguchi, K. Watanabe, H. Dery, W. Yao, and X. Xu. *Excitonic luminescence upconversion in a two-dimensional semiconductor*. Nature Physics **12**, 323–327 (2016).

[324] K. Hao, L. Xu, P. Nagler, A. Singh, K. Tran, C. K. Dass, C. Schu, T. Korn, X. Li, and G. Moody. *Coherent and Incoherent Coupling Dynamics between Neutral and Charged Excitons in Monolayer MoS_2*. Nano Letters **16**, 5109–5113 (2016).

[325] M. Manca, M. M. Glazov, C. Robert, F. Cadiz, T. Taniguchi, K. Watanabe, E. Courtade, T. Amand, P. Renucci, X. Marie, G. Wang, and B. Urbaszek. *Enabling valley selective exciton scattering in monolayer WSe_2 through upconversion*. Nature Communications **8**, 14927 (2017).

[326] B. Han, C. Robert, E. Courtade, M. Manca, S. Shree, T. Amand, P. Renucci, T. Taniguchi, K. Watanabe, X. Marie, L. E. Golub, M. M. Glazov, and B. Urbaszek. *Exciton States in Monolayer $MoSe_2$ and $MoTe_2$ Probed by Upconversion Spectroscopy*. Physical Review X **8**, 031073 (2018).

[327] J. Jadczak, L. Bryja, J. Kutrowska-Girzycka, P. Kapuściński, M. Bieniek, Y.-S. Huang, and P. Hawrylak. *Room temperature multi-phonon upconversion photoluminescence in monolayer semiconductor WS_2*. Nature Communications **10**, 107 (2019).

[328] Y. Dai, P. Qi, G. Tao, G. Yao, B. Shi, Z. Liu, Z. Liu, X. He, P. Peng, Z. Dang, L. Zheng, T. Zhang, Y. Gong, Y. Guan, K. Liu, and Z. Fang. *Phonon-assisted upconversion in twisted two-dimensional semiconductors*. Light: Science & Applications **12**, 6 (2023).

[329] S. Ayari, S. Jaziri, R. Ferreira, and G. Bastard. *Phonon-assisted exciton/trion conversion efficiency in transition metal dichalcogenides*. Physical Review B **102**, 125410 (2020).

[330] C. Robert, D. Lagarde, F. Cadiz, G. Wang, B. Lassagne, T. Amand, A. Balocchi, P. Renucci, S. Tongay, B. Urbaszek, and X. Marie. *Exciton radiative lifetime in transition metal dichalcogenide monolayers*. Physical Review B **93**, 205423 (2016).

[331] D. L. Dexter. *A theory of sensitized luminescence in solids*. The Journal of Chemical Physics **21**, 836–850 (1953).

[332] M. Stavola, D. L. Dexter, and R. S. Knox. *Electron-hole pair excitation in semiconductors via energy transfer from an external sensitizer*. Physical Review B **31**, 2277–2289 (1985).

[333] G. Froehlicher, E. Lorchat, and S. Berciaud. *Charge Versus Energy Transfer in Atomically Thin Graphene-Transition Metal Dichalcogenide van der Waals Heterostructures*. Physical Review X **8**, 011007 (2018).

[334] T. Förster. *Energiewanderung und Fluoreszenz*. Naturwissenschaften **33**, 166–175 (1946).

[335] T. Förster. *Zwischenmolekulare Energiewanderung und Fluoreszenz*. Annalen der Physik **437**, 55–75 (1948).

[336] J. R. Lakowicz. "Energy Transfer." *Principles of Fluorescence Spectroscopy Third Edition*. Springer US, 2006, pp. 443–475.

[337] Z. Hu, P. L. Hernández-Martínez, X. Liu, M.-R. Amara, W. Zhao, K. Watanabe, T. Taniguchi, H. V. Demir, and Q. Xiong. *Trion-Mediated Förster Resonance Energy Transfer and Optical Gating Effect in WS_2 /hBN/$MoSe_2$ Heterojunction.* ACS Nano **14**, 13470–13477 (2020).

[338] C. Manolatou, H. Wang, W. Chan, S. Tiwari, and F. Rana. *Radiative and non-radiative exciton energy transfer in monolayers of two-dimensional group-VI transition metal dichalcogenides.* Physical Review B **93**, 155422 (2016).

[339] M. Selig, E. Malic, K. J. Ahn, N. Koch, and A. Knorr. *Theory of optically induced Förster coupling in van der Waals coupled heterostructures.* Physical Review B **99**, 035420 (2019).

[340] D. Kozawa, A. Carvalho, I. Verzhbitskiy, F. Giustiniano, Y. Miyauchi, S. Mouri, A. H. C. Neto, K. Matsuda, and G. Eda. *Evidence for Fast Interlayer Energy Transfer in $MoSe_2/WS_2$ Heterostructures.* Nano Letters **16**, 4087–4093 (2016).

[341] X. Liu, Z. Hao, E. Khalaf, J. Y. Lee, Y. Ronen, H. Yoo, D. H. Najafabadi, K. Watanabe, T. Taniguchi, A. Vishwanath, and P. Kim. *Tunable spin-polarized correlated states in twisted double bilayer graphene.* Nature **583**, 221–225 (2020).

[342] Q. Zhang, E. Linardy, X. Wang, and G. Eda. *Excitonic Energy Transfer in Heterostructures of Quasi-2D Perovskite and Monolayer WS_2.* ACS Nano **14**, 11482–11489 (2020).

[343] C. Lei, Y. Ma, X. Xu, T. Zhang, B. Huang, and Y. Dai. *Broken-Gap Type-III Band Alignment in WTe_2/HfS_2 van der Waals Heterostructure.* The Journal of Physical Chemistry C **123**, 23089–23095 (2019).

[344] A. Karmakar, T. Kazimierczuk, I. Antoniazzi, M. Raczyński, S. Park, H. Jang, T. Taniguchi, K. Watanabe, A. Babiński, A. Al-Mahboob, and M. R. Molas. *Excitation-Dependent High-Lying Excitonic Exchange via Interlayer Energy Transfer from Lower-to-Higher Bandgap 2D Material.* Nano Letters **23**, 5617–5624 (2023).

[345] J. J. P. Thompson, M. Gerhard, G. Witte, and E. Malic. *Optical signatures of Förster-induced energy transfer in organic/TMD heterostructures.* npj 2D Materials and Applications **7**, 69 (2023).

[346] P. Parzefall, J. Holler, M. Scheuck, A. Beer, K.-Q. Lin, B. Peng, B. Monserrat, P. Nagler, M. Kempf, T. Korn, and C. Schüller. *Moiré phonons in twisted $MoSe_2$ –WSe_2 heterobilayers and their correlation with interlayer excitons.* 2D Materials **8**, 035030 (2021).

[347] L. Wu, Y. Chen, H. Zhou, and H. Zhu. *Ultrafast energy transfer of both bright and dark excitons in 2D van der Waals heterostructures beyond dipolar coupling.* ACS Nano **13**, 2341–2348 (2019).

[348] G. C. He, L. N. Shi, Y. L. Hua, and X. L. Zhu. *The phonon scattering mechanism and its effect on the temperature dependent thermal and thermoelectric properties of a silver nanowire.* Physical Chemistry Chemical Physics **24**, 3059–3065 (2022).

[349] G. Meneghini, S. Brem, and E. Malic. *Excitonic Thermalization Bottleneck in Twisted TMD Heterostructures*. Nano Letters **24**, 4505–4511 (2024).

[350] W. Knorr, S. Brem, G. Meneghini, and E. Malic. *Polaron-induced changes in moiré exciton propagation in twisted van der Waals heterostructures*. Nanoscale **16**, 8996–9003 (2024).

[351] E. Wigner. *On the Interaction of Electrons in Metals*. Physical Review **46**, 1002–1011 (1934).

[352] E. Wigner. *Effects of the electron interaction on the energy levels of electrons in metals*. Transactions of the Faraday Society **34**, 678 (1938).

[353] C. C. Grimes and G. Adams. *Evidence for a Liquid-to-Crystal Phase Transition in a Classical, Two-Dimensional Sheet of Electrons*. Physical Review Letters **42**, 795–798 (1979).

[354] R. S. Crandall. *Collective Modes of a Two-Dimensional Wigner Crystal*. Physical Review A **8**, 2136–2142 (1973).

[355] L. Bonsall and A. A. Maradudin. *Some static and dynamical properties of a two-dimensional Wigner crystal*. Physical Review B **15**, 1959–1973 (1977).

[356] H. Yu and J. Zhou. *Phonons of electronic crystals in two-dimensional semiconductor moiré patterns*. Natural Sciences **3** (2023).

[357] D. Yang, L. Li, N. Zhang, and H. Yu. *Chiral phonons of honeycomb-type bilayer Wigner crystals*. Chinese Physics B **34**, 017301 (2024).

[358] D. Erkensten and E. Malic. *Private Communication* (2025).

[359] H. Zhu, J. Yi, M.-Y. Li, J. Xiao, L. Zhang, C.-W. Yang, R. A. Kaindl, L.-J. Li, Y. Wang, and X. Zhang. *Observation of chiral phonons*. Science **359**, 579–582 (2018).

[360] E. Liu, J. van Baren, T. Taniguchi, K. Watanabe, Y.-C. Chang, and C. H. Lui. *Valley-selective chiral phonon replicas of dark excitons and trions in monolayer WSe_2*. Physical Review Research **1**, 032007 (2019).

[361] M. He, P. Rivera, D. V. Tuan, N. P. Wilson, M. Yang, T. Taniguchi, K. Watanabe, J. Yan, D. G. Mandrus, H. Yu, H. Dery, W. Yao, and X. Xu. *Valley phonons and exciton complexes in a monolayer semiconductor*. Nature Communications **11**, 618 (2020).

[362] A. Delhomme, D. Vaclavkova, A. Slobodeniuk, M. Orlita, M. Potemski, D. M. Basko, K. Watanabe, T. Taniguchi, D. Mauro, C. Barreteau, E. Giannini, A. F. Morpurgo, N. Ubrig, and C. Faugeras. *Flipping exciton angular momentum with chiral phonons in $MoSe_2/WSe_2$ heterobilayers*. 2D Materials **7**, 041002 (2020).

[363] M. Lamparski, B. V. Troeye, and V. Meunier. *Soliton signature in the phonon spectrum of twisted bilayer graphene*. 2D Materials **7**, 025050 (2020).

[364] J. Quan, L. Linhart, M. L. Lin, D. Lee, J. Zhu, C. Y. Wang, W. T. Hsu, J. Choi, J. Embley, C. Young, T. Taniguchi, K. Watanabe, C. K. Shih, K. Lai, A. H. MacDonald, P. H. Tan, F. Libisch, and X. Li. *Phonon renormalization in reconstructed MoS_2 moiré superlattices*. Nature Materials **20**, 1100–1105 (2021).

[365] P. Parzefall. *Optical characterization of $MoSe_2$-WSe_2 heterobilayer lattices*. Universität Regensburg, Master's thesis (2021).

[366] S. Carr, D. Massatt, S. B. Torrisi, P. Cazeaux, M. Luskin, and E. Kaxiras. *Relaxation and domain formation in incommensurate two-dimensional heterostructures*. Physical Review B **98**, 224102 (2018).

[367] H. Yoo, R. Engelke, S. Carr, S. Fang, K. Zhang, P. Cazeaux, S. H. Sung, R. Hovden, A. W. Tsen, T. Taniguchi, K. Watanabe, G. C. Yi, M. Kim, M. Luskin, E. B. Tadmor, E. Kaxiras, and P. Kim. *Atomic and electronic reconstruction at the van der Waals interface in twisted bilayer graphene*. Nature Materials **18**, 448–453 (2019).

[368] M. R. Rosenberger, H. J. Chuang, M. Phillips, V. P. Oleshko, K. M. McCreary, S. V. Sivaram, C. S. Hellberg, and B. T. Jonker. *Twist Angle-Dependent Atomic Reconstruction and Moiré Patterns in Transition Metal Dichalcogenide Heterostructures*. ACS Nano **14**, 4550–4558 (2020).

[369] A. Weston, Y. Zou, V. Enaldiev, A. Summerfield, N. Clark, V. Zólyomi, A. Graham, C. Yelgel, S. Magorrian, M. Zhou, J. Zultak, D. Hopkinson, A. Barinov, T. H. Bointon, A. Kretinin, N. R. Wilson, P. H. Beton, V. I. Fal'ko, S. J. Haigh, and R. Gorbachev. *Atomic reconstruction in twisted bilayers of transition metal dichalcogenides*. Nature Nanotechnology **15**, 592–597 (2020).

[370] I. Maity, P. K. Maiti, H. R. Krishnamurthy, and M. Jain. *Reconstruction of moiré lattices in twisted transition metal dichalcogenide bilayers*. Physical Review B **103**, L121102 (2021).

[371] J. Holler, S. Meier, M. Kempf, P. Nagler, K. Watanabe, T. Taniguchi, T. Korn, and C. Schüller. *Low-frequency Raman scattering in WSe_2-$MoSe_2$ heterobilayers: Evidence for atomic reconstruction*. Applied Physics Letters **117** (2020).

[372] K. Uchida, S. Furuya, J.-I. Iwata, and A. Oshiyama. *Atomic corrugation and electron localization due to Moiré patterns in twisted bilayer graphenes*. Physical Review B **90**, 155451 (2014).

[373] X. Zhang, Q.-H. Tan, J.-B. Wu, W. Shi, and P.-H. Tan. *Review on the Raman spectroscopy of different types of layered materials*. Nanoscale **8**, 6435–6450 (2016).

[374] Y. Pan and D. R. T. Zahn. *Raman Fingerprint of Interlayer Coupling in 2D TMDCs*. Nanomaterials **12**, 3949 (2022).

[375] Y. Pan, S. Li, M. Rahaman, I. Milekhin, and D. R. T. Zahn. *Signature of lattice dynamics in twisted 2D homo/hetero-bilayers*. 2D Materials **9**, 045018 (2022).

[376] Y. Zhao, X. Luo, H. Li, J. Zhang, P. T. Araujo, C. K. Gan, J. Wu, H. Zhang, S. Y. Quek, M. S. Dresselhaus, and Q. Xiong. *Interlayer Breathing and Shear Modes in Few-Trilayer MoS_2 and WSe_2*. Nano Letters **13**, 1007–1015 (2013).

[377] W. Zhao, Z. Ghorannevis, K. K. Amara, J. R. Pang, M. Toh, X. Zhang, C. Kloc, P. H. Tan, and G. Eda. *Lattice dynamics in mono- and few-layer sheets of WS_2 and WSe_2*. Nanoscale **5**, 9677–9683 (2013).

[378] S. Meier, M. Dietl, P. Parzefall, M. Kempf, J. Holler, P. Nagler, C. Schüller, Y. Zhumagulov, P. E. F. Junior, J. Fabian, and T. Korn. *Supplemental Material: Emergent trion-phonon coupling in atomically-reconstructed MoSe 2-WSe 2 heterobilayers*. Physical Review Research **5**, L032036 (2023).

[379] J. Zipfel, K. Wagner, M. A. Semina, J. D. Ziegler, T. Taniguchi, K. Watanabe, M. M. Glazov, and A. Chernikov. *Electron recoil effect in electrically tunable $MoSe_2$ monolayers*. Physical Review B **105**, 075311 (2022).

[380] T. Deilmann, P. Krüger, and M. Rohlfing. *Ab Initio Studies of Exciton g Factors: Monolayer Transition Metal Dichalcogenides in Magnetic Fields*. Physical Review Letters **124**, 226402 (2020).

[381] J. Förste, N. V. Tepliakov, S. Y. Kruchinin, J. Lindlau, V. Funk, M. Förg, K. Watanabe, T. Taniguchi, A. S. Baimuratov, and A. Högele. *Exciton g-factors in monolayer and bilayer WSe_2 from experiment and theory*. Nature Communications **11**, 4539 (2020).

[382] F. Xuan and S. Y. Quek. *Valley Zeeman effect and Landau levels in two-dimensional transition metal dichalcogenides*. Physical Review Research **2**, 033256 (2020).

[383] S. Meier. *Resonant Raman spectroscopy of low-dimensional semiconductor structurestures*. Universität Regensburg, PhD thesis (2022).

[384] J. Lichtenberger. *Spannungsabhängige Untersuchung der Hybridschermode an $MoSe_2$-WSe_2 Heterostrukturen mittels optischer Spektroskopie*. Universität Regensburg, Master's thesis (2024).

[385] G. Scuri, T. I. Andersen, Y. Zhou, D. S. Wild, J. Sung, R. J. Gelly, D. Bérubé, H. Heo, L. Shao, A. Y. Joe, A. M. M. Valdivia, T. Taniguchi, K. Watanabe, M. Lončar, P. Kim, M. D. Lukin, and H. Park. *Electrically Tunable Valley Dynamics in Twisted WSe_2/WSe_2 Bilayers*. Physical Review Letters **124**, 217403 (2020).

[386] R. Perea-Causin, S. Brem, F. Buchner, Y. Lu, K. Watanabe, T. Taniguchi, J. M. Lupton, K.-Q. Lin, and E. Malic. *SI: Electrically tunable layer-hybridized trions in doped WSe_2 bilayers*. Nature Communications **15**, 6713 (2024).

[387] Y. Wang, Z. Wang, W. Yao, G. B. Liu, and H. Yu. *Interlayer coupling in commensurate and incommensurate bilayer structures of transition-metal dichalcogenides*. Physical Review B **95** (2017).

[388] X. Zhang, W. Y. Shan, and D. Xiao. *Optical Selection Rule of Excitons in Gapped Chiral Fermion Systems*. Physical Review Letters **120** (2018).

[389] I. Paradisanos, S. Shree, A. George, N. Leisgang, C. Robert, K. Watanabe, T. Taniguchi, R. J. Warburton, A. Turchanin, X. Marie, I. C. Gerber, and B. Urbaszek. *Controlling interlayer excitons in MoS_2 layers grown by chemical vapor deposition*. Nature Communications **11** (2020).

[390] K. Ko, A. Yuk, R. Engelke, S. Carr, J. Kim, D. Park, H. Heo, H. M. Kim, S. G. Kim, H. Kim, T. Taniguchi, K. Watanabe, H. Park, E. Kaxiras, S. M. Yang, P. Kim, and H. Yoo. *Operando electron microscopy investigation of polar domain dynamics in twisted van der Waals homobilayers*. Nature Materials **22**, 992–998 (2023).

[391] F. Paleari, H. P. C. Miranda, A. Molina-Sánchez, and L. Wirtz. *Exciton-Phonon Coupling in the Ultraviolet Absorption and Emission Spectra of Bulk Hexagonal Boron Nitride*. Physical Review Letters **122**, 187401 (2019).

[392] T. Jiang, H. Liu, D. Huang, S. Zhang, Y. Li, X. Gong, Y. R. Shen, W. T. Liu, and S. Wu. *Valley and band structure engineering of folded MoS_2 bilayers*. Nature Nanotechnology **9**, 825–829 (2014).

[393] P. Hein, A. Stange, K. Hanff, L. X. Yang, G. Rohde, K. Rossnagel, and M. Bauer. *Momentum-resolved hot electron dynamics at the 2H-MoS_2 surface*. Physical Review B **94**, 205406 (2016).

[394] R. Wallauer, J. Reimann, N. Armbrust, J. Güdde, and U. Höfer. *Intervalley scattering in MoS_2 imaged by two-photon photoemission with a high-harmonic probe*. Applied Physics Letters **109** (2016).

[395] S.-Y. Chen, C. Zheng, M. S. Fuhrer, and J. Yan. *Helicity-Resolved Raman Scattering of MoS_2, $MoSe_2$, WS_2, and WSe_2 Atomic Layers*. Nano Letters **15**, 2526–2532 (2015).

List of publications

1. **P. Parzefall**, J. Holler, M. Scheuck, A. Beer, KQ. Lin, B. Peng, B. Monserrat, P. Nagler, M. Kempf, T. Korn, and C. Schüller. *Moiré phonons in twisted $MoSe_2$-WSe_2 heterobilayers and their correlation with interlayer excitons.* 2D Materials **8**, 035030 (2021)

2. KQ. Lin, J. Holler, J. Bauer, **P. Parzefall**, M. Scheuck, B. Peng, T. Korn, S. Bange, J. Lupton, and C. Schüller. *Large-Scale Mapping of Moiré Superlattices by Hyperspectral Raman Imaging.* Advanced Materials **33**, 2008333 (2021)

3. S. Meier, Y. Zhumagulov, M. Dietl, **P. Parzefall**, M. Kempf, J. Holler, P. Nagler, P. E. Faria Junior, J. Fabian, T. Korn, and C. Schüller. *Emergent trion-phonon coupling in atomically reconstructed $MoSe_2$-WSe_2 heterobilayers.* Physical Review Research **5**, L032036 (2023)

4. A. Beer, K. Zollner, C. Serati de Brito, P. E. Faria Junior, **P. Parzefall**, T. S. Ghiasi, J. Ingla-Aynés, S. Manãs-Valero, C. Boix-Constant, K. Watanabe, T. Taniguchi, J. Fabian, H. S. J. van der Zant, Y. Galvão Gobato, and C. Schüller. *Proximity-Induced Exchange Interaction and Prolonged Valley Lifetime in $MoSe_2$-/CrSBr Van-Der-Waals Heterostructure with Orthogonal Spin Textures.* ACS Nano **18**, 31044-31054 (2024)

5. **P. Parzefall**, N. Paulik, C. Serati de Brito, J. Göser, J. Trapp, K. Watanabe, T. Taniguchi, D. Erkensten, G. Meneghini, Y. Galvão Gobato, E. Malic, A. Högele, and C. Schüller. *Programmable phonon-assisted resonant energy transfer between moiré cells in charge-tunable $MoSe_2$-WS_2 heterobilayers.* npj 2D materials and applications **9**, 84 (2025)

Danksagung

Nun komme ich zu dem für mich wichtigsten Teil meiner Arbeit, da ich nun allen danken darf, die mich begleitet und ein erfolgreiches Gelingen meiner Arbeit erst ermöglicht haben.

An erster Stelle danke ich Christian für deine wunderbare Betreuung meiner Arbeit. Danke, dass du den Grundstein gelegt hast, mir alle Möglichkeiten gegeben hast, sei es nicht nur durch deine wissenschaftlichen Ideen, sondern auch durch das Ausleben meiner eigenen, sowie durch Konferenz- und Auslandsbesuche, bei denen ich die wissenschaftliche Gemeinschaft und die damit verbundene wissenschaftliche Arbeit in all ihren Facetten kennenlernen durfte. Durch die enge Zusammenarbeit durfte ich lernen, wie man aus einer unübersichtlichen Datenmenge systematisch und erfolgreich Schlüsse zieht, die am Ende in eine erfolgreiche Veröffentlichung münden.

Des Weiteren danke ich PD Dr. Jonathan Eroms für die Übernahme des Zweitgutachtens meiner Dissertation und Prof. Dr. Bali und Prof. Dr. Bougeard für das Eintreten als Prüfer bei meiner Verteidigung.

Danke an die ganze Arbeitsgruppe, dass wir uns nicht nur wissenschaftlich immer unterstützten, sondern durch eure offene Art ein Umfeld erschaffen habt, in dem man immer gerne zur Arbeit geht, auch wenn die Zeiten im Labor frustrierend sind. Danke, Johannes, dass du mich eingelernt hast und für Fragen immer offen warst. Danke, Sebastian, für die Übergabe deiner Expertise im Raman-Labor. Danke, Andi, Anna, Michi, Verena, Simon, Johannes, Caique, Marco und Marten, dass ich euch nicht nur meine Kollegen, sondern auch Freunde nennen darf. Danke an alle meine Bacheloranden Matthias, Susanne und Annika und an meine Masteranden Fabian Dallinger, Nici und Jakob für eure Unterstützung im Labor und bei unserer Arbeit.

Danke an Eva Weiss, Doris Meier und Elke Haushalter, dass ihr immer eine offene Tür und eure Hilfe für administrative Aufgaben anbietet. Danke an Christof für deine Unterstützung im Labor und deine hilfsbereite Art. Bei all meinen Ideen und Vorschlägen fühlte ich mich immer sehr geschätzt und unterstützt.

Danke auch besonders an all diejenigen, die meine Arbeit anderweitig unterstützten, sei es durch eine wissenschaftliche Kollaboration, durch das Anhören meiner Probevorträge über die Jahre, durch Feedback zu meiner Arbeit oder einfach dadurch, dass ihr für neuen Schwung im Gespräch bei einer Tasse Kaffee oder Tee sorgtet.

Danke an große Teile der Fakultät, durch eure offene Art wird es einem ermöglicht, nicht nur mit Ideen, sondern auch mit Fragen und Problemen anzukommen und im offenen Austausch gemeinsam zu grübeln. Danke, Prof. Dr. Bougeard, Slava, Paulo, Kai-Qiang, Imke und Sebastians (Bange und Krug).

Danke an all diejenigen, die mich durch Material oder fertige Proben unterstützten. Danke, Johannes, Philipp Nagler, Marten, Fabi, Niclas, Jakob, Nici, Lucia, Philip, Anna, Nadine, Jonas (Bauer und Göser) und Julian Trapp.

Vielen Dank, Mama und Papa, dass ihr mich bei meinen Träumen, Wünschen und einfach in allen Lebenslagen stets unterstützt. Danke für das Ermöglichen einer solchen Ausbildung. Danke an meine beiden Lieblingschwestern Anna und Teresa. Danke, Lu, du gibst mir Kraft, Erfüllung und grenzenlosen Optimismus.